AN ABSTRACT OF THE DISSERTATION OF

Daniel McCulley for the degree of Doctor of Philosophy in Physics presented on March 12, 2020

Title: Measuring the Electric Field Dependence of Photocurrent Quantum Yield in Suspended Carbon Nanotube pn Junctions

Abstract approved: _____

Ethan D. Minot

In nanoscale materials, the Coulombic interaction between electrons are stronger than in bulk materials. These stronger interactions, caused by confinement and reduced dielectric screening, have interesting consequences for light-matter interactions. In carbon nanotubes (CNTs), strong interactions can enhance the impact ionization process, and thus assist photocurrent generation in CNTs. Conversely, the strength of the attraction between photo-excited electrons and holes can hinder photocurrent generation by binding electrons and holes to each other. An understanding of both impact ionization and electron-hole binding is needed to determine which will dominate the system and under what circumstances. The central question of this research is whether high efficiency photocurrent can be generated in a material that has strong Coulombic interactions between charge carriers. In this thesis I explore the possibility of using electric fields to ionize excitons and thereby access a regime where highly efficient photocurrent generation can be achieved.

I begin by introducing simple theoretical models that explain the general features of CNT optical properties. Increasing the complexity of the models reveals finer details of the system and allows us to estimate the effect of electric field on the exciton energy state and ionization rate.

To maximize Coulmbic interactions between charge carriers, I made fully suspended CNTs by growing the nanotubes over a trench using a fast-heat chemical vapor deposition process. Split-gate electrodes at the bottom of the trench are used create a pn junction in the nanotube by applying opposite voltages to each gate, populating each half of the nanotube opposite-sign charge. The devices form near ideal diodes, and the samples are remarkably clean. The same design of CNT devices that I used are also used by our collaborators at University of Utah to study strongly interacting transport phenomena at low temperature.

A number of computational models were used to quantify the CNT device parameters. Working with Dr. Andrea Bertoni, we created and experimentally verified an electrostatics model that calculates the electric field in the CNT pn junction and determines the intrinsic region length. Experimental verification of the simulations was achieved using scanning photocurrent microscopy. Simulations of the optical interference patterns near the nanotube were performed using finite-difference-time-domain software to determine the number of photons absorbed by the CNT. Dr. Vasili Perebeinos computed the effect of electric field on the excited states in carbon nanotubes by solving the Bethe-Salpeter equation for a CNT exciton in a static electric field.

Photocurrent spectra were measured around the S_{22} resonance on eight different CNTs over a range of electric fields up to $\sim 10\ \mathrm{V}/\mu\mathrm{m}$. The spectra are processed to extract the photocurrent quantum yield (PCQY) from the photocurrent peak. The PCQY increases with field in all cases, and increases by a factor of 35 to a value of 1.85 electrons per photon in the largest diameter CNT (with D = 2.8 nm). The same procedure was performed for the S_{33} resonance which shows a weaker field dependence, but larger PCQY ~ 0.3 at low field.

The results show that the photocurrent quantum yield can exceed 100% at the S_{22} exciton resonance sufficiently large axial electric field and CNT diameter. This suggests that impact ionization can coexist with efficient exciton dissociation when the electric field is ~10 V/μm and the CNT diameter is ~ 2.8 nm. We observed a different PCQY field dependence for S_{33} excitons. A large fraction of S_{33} excitons autoionize at low fields, resulting in a high PQCY at low field. We observe a gradual increase in PCQY with respect to field. The gradual increase is attributed

to reduced recombination of the free carriers by sweeping them out of the device more quickly. To interpret our data we compared our experimental results with theoretical calculations of the decay products of S_{22} and S_{33} excitons. This research serves as a framework that can be extended to other systems with strong interactions, and motivates future work tuning the carrier interaction strength to achieve high-efficiency photocurrent generation.

Measuring the Electric Field Dependence of Photocurrent Quantum Yield in Suspended Carbon Nanotube pn Junctions

by
Daniel McCulley

A DISSERTATION

submitted to

Oregon State University

in partial fulfillment of
the requirements for the
degree of

Doctor of Philosophy

Presented March 12, 2020
Commencement June 2020

Doctor of Philosophy dissertation of Daniel McCulley presented on March 12, 2020

APPROVED:

Major Professor, representing Physics

Head of the Department of Physics

Dean of the Graduate School

I understand that my dissertation will become part of the permanent collection of Oregon State University libraries. My signature below authorizes release of my dissertation to any reader upon request.

Daniel McCulley, Author

ACKNOWLEDGEMENTS

The past six years were tumultuous and productive. I needed support both professionally and personally to grow as an expert in my field and as a person. Fortunately, the great people around me rose to the occasion.

I'd like to express my gratitude to my advisor Ethan Minot for all of the ways you found to help me. You were consistently creative and constructive in your guidance. You're a truly talented advisor, and a gift to our community.

The people I worked with in the Minot lab made the days more productive and much more enjoyable. Lee and Morgan, just about everything I know about the lab came from you. I look up to both of you. Mitch, we learned a lot from each other. You're good at many things I'm not, you're a great friend, and thank you for all the work you did that went into this thesis. Carly, you had the closest desk to mine, and that was just a cross you had to bear. I appreciate our friendship born from an unlikely shared interest in crosswords and mma fighting. Dublin, there's only room in that lab for one meme lord, good luck.

Mom, you supported me while I found my way in the world and encouraged me in every way you could. Dad, thanks for the support throughout all these years in school. Si, you praised me for hard work, and without knowing you I wouldn't have thought this was possible.

To all of my friends from the physics department, you gave me a community and made me feel I'm not here by mistake. And a final thanks to my sweet cat Obi who wakes me up every morning.

CONTRIBUTION OF AUTHORS

Mitchell Senger wrote data analysis protocols, performed simulations of optical interference, and assisted in data collection. Dr. Andrea Bertoni created a self-consistent electrostatic model to determine the axial electric field in the carbon nanotube. Dr. Vasili Perebeinos assisted in the interpretation of the final results by modeling the effect of electric field on absorption and the decay products of the excitons.

TABLE OF CONTENTS

Page

1 Introduction 1
1.1 The role of interactions in carbon nanotube transport phenomena 2
1.2 The role of interactions in opto-electronics 3
1.3 Impact ionization and multiple exciton generation in carbon nanotubes 5
1.4 Collaborative works not described in this thesis 6
1.4.1 Wigner crystal compressibility 7
1.4.2 Studies of carbon nanotube band gaps 7
1.4.3 Early photocurrent quantum yield measurements 7
2 Carbon nanotube optical properties 9
2.1 Harmonic oscillator with a sinusoidal driving force 9
2.2 Thomas-Reich-Kuhn sum rule and comparison to experiment 11
2.3 A semi-classical, two-state system 11
2.4 Fermi's Golden Rule 13
2.5 Effect of confinement on electron energy states 15
2.6 Ionization field of excitons 18
2.7 Excitonic Stark effect 20
3 Device background 22
3.1 Device dimensions 22
3.2 Nanotube growth 23
3.3 Transport Properties 24
3.4 Device Stability 26
3.5 Exceptional properties of the suspended CNTs 27
3.6 Optimizing nanotube growth and shipment 28
4 Computational modeling 29
4.1 Self-consistent field calculations 29
4.1.1 Self-consistent field calculation methods 30
4.1.2 Self-consistent field calculation results and discussion 32
4.1.3 Extracting intrinsic region length from electrostatic modeling 34
4.1.4 Cross-check of calculated charge density 35
4.2 Computational modeling of excited states in carbon nanotubes 37

TABLE OF CONTENTS (CONTINUED)

4.2.1 Shift in exciton absorption peak location with field 37
4.2.2 Calculation of change in carbon nanotube oscillator strength 38
4.2.3 Change in spectral width of exciton peaks 39
4.3 Simulation of optical interference from back reflection 41
5 Field dependence of photocurrent quantum yield 45
5.1 Photocurrent measurement of carbon nanotube photodiodes 45
5.1.1 Scanning Photocurrent Imaging 45
5.1.2 Illuminated diode curve 46
5.1.3 Carbon nanotube photocurrent spectroscopy 48
5.2 Calculation of photocurrent quantum yield 49
5.2.1 Extracting quantum yield from a photocurrent spectrum 49
5.2.2 Determination of photon flux 52
5.2.3 Imaging the intrinsic region length 54
5.2.4 Effect of angle on axial field 58
5.3 Photocurrent spectra in changing axial electric field 59
5.3.1 Peak shifting 60
5.3.2 Peak width 61
5.4 Photocurrent quantum yield as a function of axial electric field 62
5.5 Exciton dissociation pathways and timescales 65
6 Conclusion 69
7 Bibiliography 71
8 Appendix: Extended data for devices A-J 78

LIST OF FIGURES

Figure Page

Figure 1.1 A schematic of a multiple exciton generation process. A high-energy exciton created from light with $\hbar\omega > E$g decays into multiple low-energy excitons. Figure taken from published work.[30] 4

Figure 2.1 Simple two-state system with an electron excited by light with energy $\hbar\omega$L and electric field strength E_0 from state $\psi 1$ with energy E_1 to state $\psi 2$ with energy E_2 12

Figure 2.2 A depiction of a transition between states separated by an energy ΔE in a semiconductor with parabolic valence and conduction bands labeled E_b and E_c respectively. 14

Figure 2.3 The axes of the carbon nanotube. 15

Figure 2.4 A Coulomb potential with a DC electric field with the exciton binding energy indicated. 19

Figure 2.5 The estimated ionization field versus the exciton binding energy from the simple model described by Eq. 2.42 (blue). The ionization field calculated using solutions to the Bethe-Salpeter equation (circles) with a quadtratic fit (orange).[58] 20

Figure 3.1 a) Schematic of split-gate electrode configuration creating a pn junction in a CNT. The blue is SiO_2 and the grey is platinum. b) An SEM image of the suspended CNT device. 22

Figure 3.2 a) Optical microscope image of an electrode surface after CNT growth without much residue. b) Optical microscope image of an electrode surface after growth with residue. The scratches on the contacts were made while probing the chip and are related to the residue. 24

Figure 3.3 a) The variety of FET transport curves (V_{sd} = 25 mV) that can be expected for semiconducting CNTs on a good growth. b) An ideal CNT FET curve with a sharp turn-on and minimal hysteresis. c) Simulated band-bending diagram for $V_g < 0$ (red) and $V_g > 0$ (blue) for a CNT with E_g = 0.53 eV. 25

Figure 3.4 a) The Dark I-V_{sd} curve of a suspended carbon nanotube pn junction with $V_{g2} = -V_{g1}$ = 5 V. b) Simulated band bending diagram for $V_{g1} = -V_{g2}$ = 5 V with E_g = 0.53 eV. 26

Figure 3.5 The change over time of the CNT FET curve while the device is left in vacuum and shifts from p-type toward n-type contact. This data was taken by Lee Aspitarte and his published work discusses it in further detail.[63] 27

Figure 4.1 Cross sectional diagram of the dimensions used in the simulation. The metal electrode thickness is 60 nm. Dotted lines represent the SiO_2 in the device. We assume translation symmetry in the third dimension. 30

LIST OF FIGURES (CONTINUED)

Figure Page

Figure 4.2 The energy bands along the length of the nanotube from SCF calculations. The chemical potential for holes, μ_h, is in equilibrium with the left electrode. The chemical potential for electrons, μ_e, is in equilibrium with the right electrode. We assume the middle of the CNT is insulating. 32

Figure 4.3 a) Schematic of the geometry used in the self-consistent electrostatic-field (SCF) calculations. Electric field lines are sketched in orange. b) Calculated charge density along the length of a CNT with E_g = 0.5 eV. The gate voltages are equal and opposite (V_{g1} = -V_{g2}). All three curves are calculated with V_{sd} = 0. c) Calculated band bending diagram (the edge of the valance and conduction bands) when $V\mathrm{g1} = -V\mathrm{g2}$ = 6 V and E_g = 0.5 eV. d) The axial-component of electric field at the center of the CNT. The grey dashed line shows the result of a zeroth-order calculation (assuming no charge on the CNT). Open circles show the results of the SCF calculations. e) Open circles show the calculated value of the intrinsic region length, L_i. The dashed lines shows values of L_i estimated using Eq. 4.9. 34

Figure 4.4 a) The charge density along the length of the CNT. Linear fits (red) are extrapolated to the x-axis to find the edge of the intrinsic region with V_{g1} = 4 V. The dashed line shows the value is comparable to using a cutoff charge density of $1e$ μm $-$ 1. b) The calculated intrinsic region length using different cutoff charge densities. 35

Figure 4.5 a) The charge density along the length of the nanotube as a function of gate voltage with Vsd = 0 V. b) The maximum charge density in p doped portion of the nanotube extracted from the SCF simulations shown in a). 36

Figure 4.6 a) The calculated absorption spectrum of a (20,16) CNT for difference values of electric field strength. b) The calculated average Stark shift of the S_{22} resonance for eight CNTs with different chiralities that are relevant to experiments discussed in chapter 5. 38

Figure 4.7 a) The calculated S22 absorption for a (20,16) CNT. b) The change in oscillator strength with field found by integrating the peaks in a). 39

Figure 4.8 Calculated changes in the FWHM of the S_{22} absorption peak as a function of field for eight different CNT chiralities. The changes are relative to FWHM values of 13 – 22 meV. The chiralities shown here are relevant to the experiments discussed in the next section. 40

Figure 4.9 a) The calculated S11 absorption peak for CNT D and CNT E, the smallest and largest diameter CNTs in the study. The changing color indicated the field increasing from F = 0 V/μm (violet) to F = 15 V/μm (yellow). b) The change in FWHM for the S11 peaks shown in a). 40

Figure 4.10 a) Cross sectional diagram of a CNT grown flat across the surface of the electrodes. b) Cross sectional diagram of a CNT that has adhered to the side of the electrode before crossing the trench. 42

LIST OF FIGURES (CONTINUED)

Figure Page

Figure 4.11 a) The FDTD simulation window with a focused Gaussian beam profile incident on the electrode geometry. b) The optical interference strength, β, at a wavelength of 1630 nm. c) Interference strength vs. photon energy measured at the center of the CNT, 616 nm above the top surface of the split gate electrodes. The range of S22 peak energies for the eight CNTs discussed in the main text is indicated. d) The interference strength vs. photon energy at different heights above the top surface of the split gate electrodes. e) The change in interference strength (defocused beam, height 616 nm) when the separation distance between the split-gates is reduced from 500 nm to 350 nm. f) Cross-sectional diagram of the electrode layout showing the separation between the gates. 43

Figure 4.12 a) The change in optical power enhancement as different elements of the similuation are included. b) Illustration of a plane wave incident on a perfect conductor (corresponds to black curve) c) Illustration of a plane wave incident on a layer of platinum (corresponds to purple curve). d) Illustration of a plane wave incident on a layer SiO_2 on top of platinum (corresponds to blue curve). e) Illustration of a plane wave incident on layers of SiO_2 and platinum with a gap in middle (corresponds to red curve). 44

Figure 5.1 Scanning photocurrent image of a CNT photodiode. The location of the source-drain electrodes and the axis of the CNT are indicated. 46

Figure 5.2 Experimental measurement of photocurrent for a (20,16) CNT excited at the S_{44} resonance ($\hbar\omega = 1.92$ eV). Photocurrent grows linearly with V_{sd} when for $V_{sd} < 0$. Linear extrapolations of these curves intercept the x-axis at the $V_{sd} = 0.4$ V, corresponding to the expected band gap of this CNT 47

Figure 5.3 a) Illuminated IV curve of a (22,11) CNT excited at the resonance $S_{22} = 0.86$ eV. b) Illuminated IV curve of a (23,12) CNT excited at the resonance $S_{22} = 0.795$ eV. 48

Figure 5.4 Photocurrent spectrum (black) around the S_{22}, S_{33}, S_{44}, S_{55}, and S_{66} exciton resonances. The spectrum was obtained with $V_{sd} = -0.5$ V and optical power ~ 10 μW spread over an area ~100 μm^2. The empirical absorption cross section of a CNT with chiral index (22,14) and diameter = 2.56 nm (blue).[66] 49

Figure 5.5 a) Photocurrent spectrum around the S_{33} exciton resonance of a CNT with chiral index (19,18) and diameter = 2.51 nm for $V_{g1} = -V_{g2} = 4$ V and $V_{sd} = -0.5$ V. b) The laser power at the height of the nanotube. c) The intrinsic region length calculated using the SCF simulations discussed in Section 4.1. d) The photocurrent peak corrected for photon flux and the intrinsic region length. Further analysis details in Appendix A for Device J. 51

LIST OF FIGURES (CONTINUED)

Figure Page

Figure 5.6 a) The typical photocurrent response as a function of laser intensity. The red linear fit has a slope of 0.3 pA cm^2 W^{-1}. b) A scanning photocurrent image sampling the PSF of the laser spot. c) Cross section of the photocurrent image in b) along the dashed red line along with a fit using the sum of three Gaussians (fit parameters in Appendix A: Device A summary) d) Cross section of the photocurrent image in b) along the dashed green line along with a Gaussian fit (fit parameters in Appendix A: Device A summary)..... 53

Figure 5.7 a) Scanning photocurrent image of the Schottky barriers at each contact with V_{sd} =0 and $V_{g1} = V_{g2} = 0$. The axis of the CNT is indicated with a dotted line. b) Scanning photocurrent image of an elongated photocurrent spot when V_{sd} = -3 V and $V_{g1} = -V_{g2} = 6$ V. c) An image of the reflected light from the scanning photocurrent image. The images shows the edges of the electrodes (white) the gate electrodes (grey) and the gap between the gate electrodes (black). d) A cross section of the photocurrent image shown in b) along the CNT axis. The fit from Eq. 5.15 is shown in red for L = 0.9 μm and a = 0.347 μm. 55

Figure 5.8 a) Cross sections of photocurrent images along the CNT axis for various $V_{g1} = -V_{g2}$. V_{sd} = -2 V for all 5 curves. b) Diode characteristics at the highest ratios of V_{sd}/V_{g1} used in (a). There is no reverse-bias break down. c) Cross sections of photocurrent images along the CNT axis at various V_{sd}. $V_{g1} = -V_{g2} = 6$ V for all 6 curves. d) Comparison of the model in Eq. 2 of the main text (red) with experimental measurement of L_i extracted from the cross sections shown in (a) (black). The fitting procedure to find L_i becomes unreliable when $V_{g1} > 6$ V (open circles), because L_i is below the spatial resolution of the microscope. The nanotube chirality is (17,12). 57

Figure 5.9 Scanning photocurrent images showing elongation of the intrinsic region when $|V_{sd}|$ increases or $V_{g1} = -V_{g2}$ decreases. The scale bar is 0.5 μm. Dashed lines indicate the CNT axis. 58

Figure 5.10 Depection of a carbon nanotube grown across two electrodes at an angle θ relative to the electric field, F_0. 58

Figure 5.11 Power normalized photocurrent spectrum around the S_{22}, S_{33}, and S_{44} exciton resonances of a CNT with chiral index (22,14) and diameter = 2.46 nm. The spectrum 59

Figure 5.12 a) S_{22} peak position as a function of axial electric field for eight different CNTs with known chirality. b) The blue curve shows the weighted average of the S_{22} peak shift for the eight CNTs discussed in the main text. The red curve shows the calculated average Stark shift of the S_{22} resonance for the same eight CNTs. The grey boundaries show the spread of peak shifts observed in the experiment. 61

Figure 5.13 a) The FWHM of the S_{22} photocurrent peaks at increasing axial field for the eight different chiralities discussed in the main text. b) The FWHM of the S_{22} photocurrent peak with an applied axial field of 4 V/μm. The dashed line is the relationship in Eq. S9. c) The change in FWHM of the S_{22} photocurrent peaks. d) Calculated changes in the FWHM of the S_{22} absorption peak as a function of field for each chirality of CNT in the study. The color coding in the inset of panel (a) applies to all of the panels..... 62

LIST OF FIGURES (CONTINUED)

Figure Page

Figure 5.14 a) The photocurrent spectrum at increasing gate voltage centered on the S_{33} exciton resonance of a (19,18) CNT with a diameter of 2.51 nm. b) The intrinsic region length at increasing gate voltage. c) The photocurrent spectrum normalized by the photon flux and intrinsic region length. d) The photocurrent quantum yield of the device versus increasing axial field. 63

Figure 5.15. a) The photocurrent quantum yield at the S_{22} exciton resonance for 8 different CNTs as a function of increasing axial electric field. V_{sd} = -0.5 V. Squares indicate insufficient data to determine photon flux. b) The PCQY as a function of field for the same 8 CNTs plotted on a third axis against the S_{22} resonance energy. 64

Figure 5.16 a) Proposed pathways for relaxation of the S_{22} exciton at low field (no field-induced exciton dissociation). Pathways that can lead to photocurrent (PC) are shown in orange. White arrows represent free carriers that are swept out by electric field. b) Computational modeling of a (20, 9) CNT. The model calculates the size distribution of the e-h separation of the decay products of the S_{22} and S_{33} phonon decay mechanism. The x-axis is the inverse size of the e-h separation using a two-particle wavefunction from the Bethe-Salpeter Equation solution. Solid lines represent the probability of generating the decay product with a certain e-h separation, and dashed lines represent the cumulative probability. The leftmost peaks in probability correspond to free carriers (Le-h = 50 nm = one quarter of the length of the simulated supercell). The rightmost peak for S_{22} decay (about 40% of the total decay products) corresponds to fully bound S_{11} and S_{12} excitons (Le-h ≈ 2.5 nm). c) Possible relaxation pathways of the S_{22} exciton at high field, including field-induced dissociation of S_{11}, S_{12}, S_{21} and S_{22} excitons..... 66

Figure 8.1 Device A Summary. a) Raw photocurrent spectrum of a (27,8) carbon nanotube. b) Laser power at the height of nanotube. c) Photocurrent image of the nanotube. The power is $P = 2.02$ μW with $\beta\text{foc} = 1.07$. d) The photocurrent spectrum corrected for photon flux and intrinsic region length. e) The photocurrent quantum yield as a function of the axial field at the center of the CNT. f) Cross sections along the photocurrent spot used to calculate an area A = 6.7 μm2. 79

Figure 8.2 Photocurrent spectrum normalized by the laser power at the height of the nanotube 34 nm below the electrode (black). The product of absorption cross section per carbon atom and the number of atoms per length of a (27,8) CNT (blue). 79

Figure 8.3 Device B Summary. a) The photocurrent spectrum of a (24,14) CNT. b) Laser power at the height of nanotube at 34 nm below the electrode surface. c) Photocurrent image of the nanotube. The power is $P = 8.36$ μW with $\beta\text{foc} = 1.14$. d) The photocurrent spectrum corrected for photon flux and intrinsic region length. e) The photocurrent quantum yield as a function of the axial field at the center of the CNT. f) Cross sections along the photocurrent spot used to calculate an area A =5.4 μm2..... 80

Figure 8.4 Photocurrent spectrum normalized by the laser power at the height of the nanotube 34 nm below the electrode (black). The product of absorption cross section per carbon atom and the number of atoms per length of a (24,14) CNT (blue). 80

LIST OF FIGURES (CONTINUED)

Figure Page

Figure 8.5 Device C Summary. Raw photocurrent spectrum of a (24,17) carbon nanotube. b) Laser power at the height of nanotube at 34 nm below the electrode surface. c) Photocurrent image of the nanotube. The power is $P = 23.1$ μW with $\beta\text{foc} = 1.31$. d) The photocurrent spectrum corrected for photon flux and intrinsic region length. e) The photocurrent quantum yield as a function of the axial field at the center of the CNT. f) Cross sections along the photocurrent spot used to calculate an area A = 9.1 μm2. 81

Figure 8.6 Photocurrent spectrum normalized by the laser power at the height of the nanotube 34 nm below the electrode (black). The product of absorption cross section per carbon atom and the number of atoms per length of a (24,17) CNT (blue). 81

Figure 8.7 Device D Summary. Raw photocurrent spectrum of a (20,9) carbon nanotube. b) Laser power at the height of nanotube at 34 nm below the electrode surface. c) The photocurrent spectrum corrected for photon flux and intrinsic region length. d) The photocurrent quantum yield as a function of the axial field at the center of the CNT. 82

Figure 8.8 Photocurrent spectrum normalized by the laser power at the height of the nanotube 34 nm below the electrode (black). The product of absorption cross section per carbon atom and the number of atoms per length of a (20,9) CNT (blue). 82

Figure 8.9 Device E Summary. Raw photocurrent spectrum of a (30,11) carbon nanotube. b) Laser power at the height of nanotube at 34 nm below the electrode surface. c) Photocurrent image of the nanotube. The power is $P = 1.63$ μW with $\beta\text{foc} = 1.52$. d) The photocurrent spectrum corrected for photon flux and intrinsic region length. e) The photocurrent quantum yield as a function of the axial field at the center of the CNT. f) Cross sections along the photocurrent spot used to calculate an area A = 5.4 μm2. 83

Figure 8.10 Photocurrent spectrum normalized by the laser power at the height of the nanotube at 34 nm below the electrode (black). The product of absorption cross section per carbon atom and the number of atoms per length of a (30,11) CNT (blue). 83

Figure 8.11 S25 Device F Summary. Raw photocurrent spectrum of a (20,10) carbon nanotube. b) Laser power at the height of nanotube at 34 nm below the electrode surface. c) Photocurrent image of the nanotube. The power is $P = 5.6$ μW with $\beta\text{foc} = 0.49$. d) The photocurrent spectrum corrected for photon flux and intrinsic region length. e) The photocurrent quantum yield as a function of the axial field at the center of the CNT. f) Cross sections along the photocurrent spot used to calculate an area A = 5.5 μm2. 84

Figure 8.12 Photocurrent spectrum normalized by the laser power at the height of the nanotube 34 nm below the electrode (black). The product of absorption cross section per carbon atom and the number of atoms per length of a (20,10) CNT (blue). 84

LIST OF FIGURES (CONTINUED)

Figure Page

Figure 8.13 Device G Summary a) Raw photocurrent spectrum of a (22,14) carbon nanotube. b) Laser power at the height of nanotube at 34 nm below the electrode surface. c) The photocurrent spectrum corrected for photon flux and intrinsic region length. d) The photocurrent quantum yield as a function of the axial field at the center of the CNT. 85

Figure 8.14 Photocurrent spectrum normalized by the laser power at the height of the nanotube 34 nm below the electrode (black). The product of absorption cross section per carbon atom and the number of atoms per length of a (22,14) CNT (blue). 85

Figure 8.15 Device H Summary. The photocurrent spectrum of a (20,16) carbon nanotube. b) Laser power at the height of nanotube at 34 nm below the electrode surface. c) Photocurrent image of the nanotube. The power is $P = 44.3$ μW with $\beta\text{foc} = 1.05$. d) The photocurrent spectrum corrected for photon flux and intrinsic region length. e) The photocurrent quantum yield as a function of the axial field at the center of the CNT. f) Cross sections along the photocurrent spot used to calculate an area A = 15.2 μm2. 86

Figure 8.16 Photocurrent spectrum normalized by the laser power at the height of the nanotube 34 nm below the electrode (black). The product of absorption cross section per carbon atom and the number of atoms per length in the nanotube (blue). 86

Figure 8.17 Device J Summary Raw photocurrent spectrum of a (19,18) carbon nanotube. b) Laser power at the height of nanotube at 34 nm below the electrode surface with $\beta\text{foc}\beta\text{def} = 1.62$. c) Photocurrent image of the nanotube. The power is $P = 46.8$ μW with $\beta\text{foc} = 1.41$. d) The photocurrent spectrum corrected for photon flux and intrinsic region length. e) The photocurrent quantum yield as a function of the axial field at the center of the CNT. f) Cross sections along the photocurrent spot were used to calculate an area $A = 4.92$ μm2. 87

Figure 8.18 Photocurrent spectrum normalized by the laser power at the height of the nanotube 34 nm below the electrode (black) and the optical width of a (19,18) nanotube (blue) 87

LIST OF TABLES

Table Page

Table 5.1 The angles of the nanotubes relative to the electrodes for the CNTs used in the study. The angle could not be determined for many CNTs, indicated as NA. 59

Table 8.1 The fitting parameters for scanning photocurrent image cross sections for Device A. The extra lobes in the photocurrent image are fit using three Gaussians. The total area under them is $A\mathrm{foc} = \pi w\mathrm{y}, 0(wx, 0 + ax, 1wx, 1 + ax, -1wx, -1)$. 79

Table 8.2 The fitting parameters for scanning photocurrent image cross sections for Device C. The extra lobes in the photocurrent image can be well fit using three Gaussians. The total area under them is $A\mathrm{foc} = \pi w\mathrm{y}, 0(wx, 0 + ax, 1wx, 1 + ax, -1wx, -1)$. 81

Table 8.3 The fitting parameters for scanning photocurrent image cross sections for Device F. The extra lobes in the photocurrent image can be well fit using three Gaussians. The total area under them is $A\mathrm{foc} = \pi w\mathrm{y}, 0(ax, 0wx, 0 + ax, 1wx, 1 + ax, -1wx, -1)$. 84

1 Introduction

Strongly interacting quantum particles can give rise to novel behavior that are inaccessible to weakly interacting systems. Prominent examples of such novel physics were discovered in the early 1900's, in which superconductivity[1] and superfluidity[2,3] were observed by entering a regime, accessible only at low temperatures, where interactions are strong relative to thermal fluctuations. In these systems, resistance-free flow of quantum particles emerged from the interaction-driven formation of composite bosons. It took more than forty years to formalize a mathematical theory which adequately explained the initial observations of superconductivity, resulting in the well known BCS theory in which the formation of cooper pairs is mediated by an electron-phonon interaction.[4] With the ultimate goal of achieving room temperature superconductivity, much larger interaction strengths are required. While we lack a comprehensive model of high temperature superconductors, one possibility is the formation of a superconducting state from electron-electron interaction physics.[5] The study of superconductors and superfluids remain active fields more than a century after their initial discovery, demonstrating both the possibilities and the challenges that arise from strongly interacting systems.

A more contempory example from the 1980's is the fractional quantum Hall effect where interaction-driven physics emerges as a result of confinement. In low-temperature, 2d-electron systems the Hall resistance was found to take on integer multiples of a discrete value (the quantum of resistance) which corresponds to quantized charge excitations.[6] This integer quantum Hall effect can be explained using a non-interacting model, however, just two years later, in higher quality samples and at lower temperature, a surpising result showed fractional charge excitations (known as the fractional quantum Hall effect).[7] An explanation for the puzzling results was proposed a year later where it was shown that the observations could modeled with an interaction-driven formation of composite bosons.[8] This experiment opened the doors to a multitude of experiments using confinement to induce strong electron-electron interactions.

Nanomaterials play an important role in the field of interaction–driven physics, where structures with nano-scale features inherently confine electrons on the order of nanometers in at least one dimension. Carbon nanotubes (CNTs) are a prime example of a material with extreme

quantum confinement. The width of the structure is approximately 1 nm, but the length can be thousands of nanometers. Interaction effects are prominent even at room temperature because the Coulombic energy scale of the system can be far greater than the thermal energy scale. In addition to confinement, electrons in a fully suspended carbon nanotube experience very little dielectric screening as there is no surrounding bulk material. CNTs host interesting electronic properties and light-matter interactions, and can be challenging to model.

1.1 The role of interactions in carbon nanotube transport phenomena

The energy of electronic states in carbon nanotubes are modulated by the effects of strong Coulomb repulsion. The distance of closest approach of two electrons in a suspended CNT gives a characteristic energy scale of the Coulomb repulsion which is given by

$$E_c = \frac{e^2}{4\pi\epsilon_{\text{eff}} D} \sim 100 \text{ meV} \tag{1.1}$$

for nanotube diameters in the range $D = 1\text{–}3$ nm, and with an effective dielectric constant of $\epsilon_{\text{eff}} = 3\epsilon_0$. The Coulomb energy scale can far exceed room temperature thermal energy scales so the effects of stong interactions can be observed even at room temperature. Electrons in metallic CNTs have been modeled as a Luttinger liquid,[9,10] and experiments find quantative agreement for the power-law scaling of both the conductance with temperature as well as the transconductance with voltage.[11] At low temperature and low carrier density, electrons localize to form a Wigner crystal state due to the dominance of Coulomb repulsion over kinetic energy of the carriers.[12,13] The plasmon frequencies of the π plasmons in single carbon nanotubes are markedly different than in aggregated nanotube samples owing to Coulomb interacitons.[14,15] These examples demonstrate how repulsive Coulomb interactions substantially modify CNT electronic transport.

Attractive Coulomb interactions share a similar energy scale to repulsion, which manifests in both the electronic and opto-electronic properties of CNTs. In electronic experiments, an interaction-driven energy gap is observed in CNTs with a nominally metallic band structure. The nature of the gap is still uncertain. One possibility is the formation of a Mott insulating state, which arises due to repulsive interactions. This state has been given considerable theoretical consideration[9,10,16–19] which is corroborated by experimental work.[20] A recent alternative model proposed that an excitonic insulating state forms.[21] The binding energy of the excitons arises

from attractive interactions. In this model, excitons form in the ground state of the system which leads to insulating behavior. Recent experimental work finds the diameter dependence of the gap agrees more closely with an excitonic insulator model than the Mott insulating state.[22]

1.2 The role of interactions in opto-electronics

In addition to novel electrical phenomena, strong carrier interactions dramatically change a material's opto-electronic properties. In the presence of strong Coulomb attraction, stable excitons can form at room temperature.[23–26] Organic semiconductors are an example of such systems which have achieved substantial commercial success functioning as LED displays. In contrast to a crystal lattice, the systems behave as a collection of molecules, where photoexcited carriers within the molecules experience strong excitonic effects and different relaxation pathways.[27] Similar effects are common in all nanoscale systems, where strong carrier interactions are ubiquitous.

The performance of optoelectronic devices depends critically on the relaxation pathways available to energetic charge carriers. Novel relaxation pathways that emerge in nanomaterials as a result of interaction physics are of particular interest. A sought-after application of such pathways is to circumvent the well known Schockley-Quiesser limit in future generations of solar cells. In a traditional solar cell, a carrier excited from light with $\hbar\omega > E_{\mathrm{g}}$ (where E_{g} is the band gap of the semiconductor) thermalizes down to the band edge and the excess energy ($\hbar\omega - E_{\mathrm{g}}$) is lost to heat. Multiple exciton generation (MEG) is a pathway in which a high-energy exciton decays into multiple low-energy excitons, sometimes referred to as a carrier multiplication pathway. Such a process can harness the energy lost to heat and produce an internal quantum efficiency greater than 100% (Illustrated in Figure 1.1). The efficiency limit of a single junction cell with E_{g} = 1.1 eV is 30% under 1 sun.[28] With idealized multiplication pathways, the ultimate efficiency shifts to 43%.[29] Achieving a substantial increase in efficiency requires a high probability of multiplication.

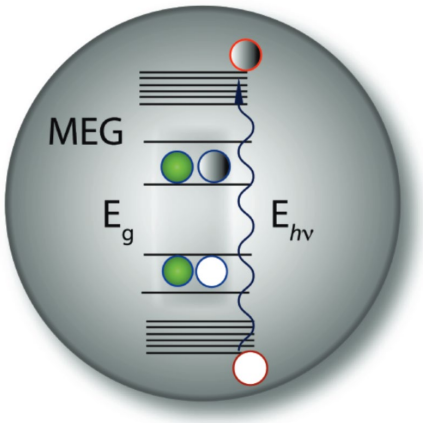

Figure 1.1 A schematic of a multiple exciton generation process. A high-energy exciton created from light with $\hbar\omega > 2E_g$ decays into multiple low-energy excitons. Figure taken from published work.[30]

The probability of MEG occuring in bulk materials is small, but the probability is enhanced in nanomaterials. Measurements of internal quantum efficiency in PbSe and PbS quantum dots (QDs) were found to outperform their bulk analogs.[31] Experimental efforts have focused on engineering MEG pathways in quantum dots to optimize performance for photovoltaic cells.[32–36] Advances in QD device design have led to the experimental realization of internal quantum efficiency greater than 100% when $\hbar\omega \gtrsim 3E_g$..[37–39] A high internal quantum efficiency doesn't necessarily mean a high power conversion efficiency. The excitons must separate and be collected at the contacts before recombination due to competing processes (e.g. Auger recombination).

Multiple exciton generation is a process which improves the efficiency of converting light into electricity by multiplying the number of carriers. Another process that can accomplish this is impact ionization which harnesses the kinetic energy of electrons and holes. In contrast to MEG (where a high energy exciton decays into multiple excitons), impact ionization occurs when a high energy electron in the conduction band excites an electron from the valence band to the conduction band through momentum transfer.

Impact ionization is commonly studied in semiconductor diode avalanche breakdown. Electrons in a region of high electric field accelerate and create additional electron-hole (e-h) pairs via collisions. An avalanche of current begins when each created e-h pair becomes a generator of additional e-h pairs and the diode breaks down. This effect is well characterized in

bulk systems.[40,41] Impact ionization has already been harnessed in existing technology in avalanche photodiodes to create highly sensitive photodetectors.[42,43] In optoelectronics experiments, impact ionization has been seen to boost the internal quantum efficiency of silicon photodiodes when $\hbar\omega > 7E_g$.[44] Impact ionization has been proposed as an alternative explanation of the carrier multiplication seen in QDs.[45] Due to enhanced Coulomb interactions, impact ionization may be accessible with lower electric field in nanomaterials, potentially boosting the quantum efficiency of photodiodes in a different regime of electric field.[44,46,47]

1.3 Impact ionization and multiple exciton generation in carbon nanotubes

Carbon nanotubes offer unique relaxation pathways for energetic charge carriers from other nanomaterials.[48] Like quantum dots they are highly confined systems, but offer the new possibility of long range electrical transport which allows for impact ionization.[49] With the possibility of both MEG and impact ionization, highly efficient photocurrent generation may be possible. Over the last decade, optoelectronic experiments in CNTs have shown that carrier multiplication is possible and that efficient photon to electron conversion can be achieved.

In 2009, Gabor et al. found signatures of multiple electron-hole generation in the photocurrent from CNT photodiodes at temperatures below 60 K.[50] Significantly, the signature of multiple electron-hole generation was apparent at the CNT's second optical resonance ($\hbar\omega \sim 2E_g$). However, the authors did not quantify photocurrent quantum yield (PCQY). PCQY is defined here as the number of electrons extracted as the photocurrent divided by the number of photons absorbed by the intrinsic region of the CNT p-i-n junction.

Later, photoluminescence experiments on CNTs found multiple exciton generation at room temperature when $\hbar\omega \approx 3E_g$.[51] In that work, the optical technique was sensitive to excitons, but not sensitive to photocurrent. Sharp increases in electroluminescence have been observed at bias voltages just below the threshold for avalanche breakdown in recent work.[52] The observation is attributed to impact ionization by excitons, providing evidence that impact ionization processes in CNTs can efficiently convert current into light. Whether the reverse process of converting light efficiently into electricity is possible remains an open question.

Early photocurrent measurements estimated the external quantum efficiency of CNT photodiodes.[53] The first optoelectronic measurement that quantified PCQY in a CNT photodiode found ~ 3%.[54] In that work, the CNT photodiode was excited at the first and second optical

resonances (S_{11} and S_{22} resonance. Aspitarte et al. used a different device geometry, and $\hbar\omega > 4E_g$ to show room-temperature PCQY ~ 30% (S_{44} and S_{55} optical resonances).[56]). Performing photocurrent spectroscopy on the same device geometry, Chang et al. saw photocurrent increase with the field of the CNT pn junction (but did not quantify the field or the PCQY).[55] Using a third device geometry, barrier-free bipolar CNT diodes, Wang et al. estimated room-temperature PCQY as high as ~ 60% at the S_{11} optical resonance.[57] Kumamoto et al. used a combination of photocurrent and photoluminescence from a suspended CNT under high bias (no pn junction) to estimate PCQY ~ 60% at an electric field ~ 15 V/μm (excitation at the S_{22} resonance).[58] The experiments by Wang et al.[57] and Kumamoto et al.[58] suggest large axial electric field is critical to achieving high PCQY in CNT photodiodes. Indeed, theory predicts a significant increase in PCQY when axial field becomes strong enough to enable exciton dissociation and impact ionization.[59,60]

In this thesis I will show that large electric fields can substantially increase exciton dissociation in CNTs. Key components of accomplishing this include quantifying the axial electric field in the CNT, quantifying the PCQY as a function of axial field, and relating the changes in PCQY to changes in exciton dissociation via computational modeling. Chapter 2 provides a basis for understanding the optical properties of CNTs by introducing a series of simple models that capture the fundamental aspects of the physics and lead to tractable calculations. Chapter 3 gives a background on the fully-suspended, dual-gated CNT device used in the experiments. Chapter 4 shows the computational methods for determining the axial field in the nanotube, the response of excitons in a CNT to an external electric field, and effect cavity enhancement in determing the intensity of light on the nanotube. Chapter 5 presents the main experimental techniques, the main results, and the interpretation.

1.4 Collaborative works not described in this thesis

I contributed to a number of projects that are not discussed in detail in this thesis. All of this work is performed on the same fully-suspended, dual-gated CNT device. The projects listed below explore the consequences of repulsive and attractive interaction physics on CNT electronic (§1.4.1 and §1.4.2) and optoelectric (§1.4.3) properties.

1.4.1 Wigner crystal compressibility

This work involved a collaboration with Vikram Deshpande's group at University of Utah. Experiments completed at Utah determined the compressibility of the Wigner crystal by measuring the energy required to add additional electrons to the nanotube. My main contribution was supplying the suspended CNT devices. An additional contribution was identifying nanotube chiralities using photocurrent spectroscopy, although Mitchell Senger performed much of that work. This work was published in Physical Review Letters in 2019.[61]

1.4.2 Studies of carbon nanotube band gaps

I worked on two projects related to the role of Coulomb interactions in carbon nanotube band gaps. The first, led by Lee Aspirarte, employed multiple measurements techniques to quantify the change in the nanotube transport gap in response to a change in dielectric environment. The work started by attempting to coat nanotubes in solid dielectrics to screen strong Coulomb interactions. Titanium dioxide was chosen for its large dielectric constant. The coating of solid dielectric material introduced substantial electrostatic disorder in the CNT.[62] This understanding motivated the use of liquids to change the dielectric environment. Using liquids introduced complications in electronic measurements, but ultimately was a success. In my contribution, I immersed suspended CNTs in various liquids, and measured the transport gap electronically from transport curves. This work was published in Scientific Reports in 2017.[63]

In later work, led my Mitchell Senger, the relationship between the transport gap and the diameter of the nanotube was measured for a number of nominally metallic nanotubes. Initially, it was thought that the interaction-driven gap in nanotubes is a Mott insulating state following from the Luttinger liquid physics mentioned in §1.1. This picture has been called into question with the proposal of an excitonic insulating state[21] which is more closely supported by our data. This work was published in 2018 in Physical Review B.[22]

1.4.3 Early photocurrent quantum yield measurements

Lee Aspitarte led the work performing the first photocurrent quantum yield measurements in our suspended CNT devices.[56] One requirement was a comprehensive understanding of the energy bands along the nanotubes and at the contacts.[64] One of my contributions to these projects was sample preparation which included photoresist removal, ebeam evaporation, nanotube growth via chemical vapor deposition, and wire bonding. I performed characterization of the

electronic transport properties which is described in §3.3. I also contributed to scanning photocurrent imaging (process described in §5.1.1), and photocurrent spectroscopy measurements (process described in §5.1.3). This work was published in Nano Letters in 2016.[56]

2 Carbon nanotube optical properties

This chapter will discuss a series of models of light-matter interactions in CNTs starting with the simplest model of a mass on a spring and then considering increasingly complex models. This model gives an estimate of the integrated absorption cross section. The precise quantum mechanical theory of the optical transitions is complex. Sum rules express the integrated absorption in a simple form, and agrees nicely with the simple classical model. For information about the frequency and polarization dependence of the absorption, I consider a two-state quantum mechanics model which further generalizes to Fermi's Golden rule. I then go on to discuss the role of confinement and extrernal electric field on the energy states of an exciton. The combination of these models provides an approachable theoretical basis for light matter interaction in CNTs in the presence of external electric fields.

2.1 Harmonic oscillator with a sinusoidal driving force

I'll start by considering a fully classical model of a damped harmonic oscillator with a sinusoidal driving force. Further information on this material can be found in Classical Mechanics by John R. Taylor.[65] The goal of this section is to model the electron as a harmonic oscillator and calculate its effective cross-sectional area for absorbing incident light. This simple model captures some of the most essential behavior of system by considering only the most important relevant quantities: electron motion in an electric field, and a mechanism for dissipation. The equation of motion of a damped-driven harmonic oscillator can be written generally as

$$\ddot{x} + \frac{\gamma}{m}\dot{x} + \omega_0^2 x = \frac{F(t)}{m} \tag{2.1}$$

where γ is a damping coefficient, ω_0 is the natural frequency of oscillation, and the driving force can be described by $F(t) = eE_0 \cos \omega t$. The wavelength is much larger than the electron's motion so the spatially dependent kx term is not included.

The first step is to calculate the work done by the drag force over one period, *T*, is described by

$$W = \int_0^T \gamma v \, dx = \int \gamma v^2 dt = \int \gamma \omega^2 A^2 \cos^2(\omega t + \phi) dt = \gamma \omega^2 A^2 \frac{T}{2} \tag{2.2}$$

The rate that energy leaves the system is $P = \frac{\gamma\omega^2 A^2}{2}$. The next step is to find the ratio of the light energy flux to the energy absorbed by the oscillation to find the effective absorption cross section. The energy flux of the light (energy/area/time) is given by

$$S = \frac{E_0^2}{2Z_0} \tag{2.3}$$

where $Z_0 = 377\Omega$ is wave impedance of free space. The absorption cross section is the ratio of the absorbed power to the enrgy flux which is given by

$$\sigma(\omega) = \frac{\gamma\omega_0^2 A^2 Z_0}{E_0^2} \tag{2.4}$$

The next step is to find the integrated absorption cross section over a wide frequency range

$$\int \sigma(\omega)d\omega = \frac{\gamma\omega_0^2 Z_0}{E_0^2}\int A^2 d\omega \tag{2.5}$$

The amplitude of a damped oscillator with a sinusoidal driving force is described by a Lorentzian of the form

$$A^2 = \frac{\left(\frac{eE_0}{m}\right)^2}{(\omega_0^2 - \omega^2) + \frac{\gamma^2\omega^2}{m^2}}. \tag{2.6}$$

The maximum amplitude when on resonance ($\omega = \omega_0$) is

$$A_{\max}^2 = \left(\frac{eE_0}{\gamma\omega_0}\right)^2. \tag{2.7}$$

The FWHM of the resonance is

$$\text{FWHM} = \frac{\gamma}{m}. \tag{2.8}$$

The area under the curve is

$$\int A^2 d\omega = \frac{\pi}{2}\,\text{FWHM} \cdot A_{\max}. \tag{2.9}$$

which gives a final expression for the integrated absorption of

$$\int \sigma(\omega)d\omega = \frac{e^2 Z_0}{m_e} = 1 \times 10^{-5}\ \text{m}^2 \cdot \text{rad} \cdot \text{s}^{-1}. \tag{2.10}$$

In the next section I will compare this number to the measured value as well as discuss the fundamental nature that the integrated absorption cross section has in a system.

2.2 Thomas-Reich-Kuhn sum rule and comparison to experiment

This section connects the ideas from the previous section to the Thomas-Reich-Kuhn (TRK) sum rule. The TRK sum rule is a powerful predictor of absorption properties for a wide variety of materials including nanoscale systems without needing to consider complex energy levels and precise quantum mechanics. In SI units the sum rule is given by

$$\int \sigma(\omega) d\omega = \frac{\pi}{2} Z_0 \sum \frac{e_i^2}{m_i} \tag{2.11}$$

which, for a single electron, exactly matches the solution from the previous section. The TRK sum rule states that the integrated absorption is a constant that depends only on the number of charges in the system and their mass.[66]

To evaluate the sum rule and the simple model in the previous section I'll compare it to a familiar value. The measured absorption cross section of the graphene p_z electron is typically reported as $\sigma = 7 \times 10^{-18}$ $\mathrm{cm^2 atom^{-1}}$. When integrating the absorption cross section per atom over the full range energy states in the graphene p_z orbital (~10 eV), the integrated absorption is

$$\int \sigma(\omega) d\omega = 1.1 \times 10^{-5} \ \ \mathrm{m^2 \cdot rad \cdot s^{-1}} \tag{2.12}$$

which is in excellent agreement with the value of a single electron harmonic oscillator. Furthermore, CNTs have a similar integrated absorption cross section to graphene despite major differences in the absorption spectrum.[67]

In summary, the simple models discussed earlier in this chapter which encorporate only coarse details of the system can acurately describe general properties of the system. Now that we understand the integrated absorption, in the next section I will discuss the finer structure within the CNT absorption spectrum.

2.3 A semi-classical, two-state system

The zeroth order model discussed in §2.1 and §2.2 gave information about the total absorption of CNTs and graphene. In this section I will introduce a basic model that incorporates quantum mechanics. The model can be generalized from a single-particle system to include a one-dimensional density of states and uncover further details of the CNT absorption spectrum. Further information on this can be found in many quantum mechanics textbooks textbooks.[68–71]

In particular, the third volume of *The Feynman Lectures on Physics* has an excellent discussion of two-state systems.

Consider the simple two-state quantum mechanics model shown in Figure 2.1.An electron is initially in a state $|\psi_1\rangle$ with energy E_1 in an electric field, E_0. shown in Figure 2.1. The wave function for the electron can be expressed as

$$\psi(x,t) = c_1\psi_1(x)e^{i\omega_1 t} + c_2\psi_2(x)e^{i\omega_2 t} \tag{2.13}$$

where $c_1(t)$ is the probability amplitude for the electron occupying $|\psi_1\rangle$ and $c_2(t)$ probability amplitude for the electron occupying $|\psi_2\rangle$. Initally the system is in the state $|\psi_1\rangle$ and therefore $c_1(0) = 1$ and $c_2(0) = 0$.

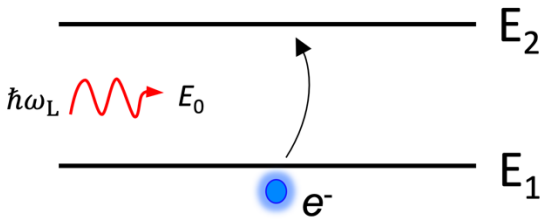

Figure 2.1 Simple two-state system with an electron excited by light with energy $\hbar\omega_L$ and electric field strength E_0 from state ψ_1 with energy E_1 to state ψ_2 with energy E_2.

The Hamiltonian of the system is described by

$$\hat{H} = \frac{p^2}{2m} + V(x) + eE_0 x\cos\omega_L t \tag{14}$$

The wavelength of light is much larger than the atomic scale, and is approximately constant across the atom ($kx \approx 0$).

Treating the field as a first order perturbation where $\hat{H} = H_0 + H'$, only H' has a time dependence. Plugging $\psi(x,t)$ into the Schrodinger equation yields

$$i\hbar\frac{d\psi(x,t)}{dt} = H'\psi(x,t). \tag{2.15}$$

Taking the inner product of $\psi_1(x)$ and $\psi_2(x)$ with the Schrodinger equations gives two differential equations that govern the system

$$i\hbar\frac{dc_1(t)}{dt} = c_2 e^{i\Delta\omega t}\cdot eE_0\cos(\omega_L t)\cdot\langle\psi_1(x)|x\cdot\psi_2(x)\rangle \tag{2.16}$$

$$i\hbar\frac{dc_2(t)}{dt} = c_1 e^{-i\Delta\omega t}\cdot eE_0\cos(\omega_L t)\cdot\langle\psi_2(x)|x\cdot\psi_1(x)\rangle. \quad (2.17)$$

The solution for short timescales ($c_1(t)\approx 1$) and for $\omega_L \approx \Delta\omega$ is given by

$$c_2(t)\approx\left(\frac{eE_0}{2i\hbar}\right)\langle\psi_1(x)|x\cdot\psi_2(x)\rangle e^{-i(\Delta\omega-\omega_L)\frac{t}{2}}\cdot t\cdot\sinh\left(\frac{(\Delta\omega-\omega_L)t}{2}\right). \quad (2.18)$$

Therefore, the probability of being in $|\psi_2\rangle$ is

$$|c_2(t)|^2 = W_{12} = \left(\frac{eE_0}{2i\hbar}\right)^2|\langle\psi_1(x)|x\cdot\psi_2(x)\rangle|^2\cdot t^2\cdot\sinh^2\left(\frac{(\Delta\omega-\omega_L)t}{2}\right). \quad (2.19)$$

For very short timescales this can be further approximated to

$$W_{12}\approx\left(\frac{eE_0}{2i\hbar}\right)^2|\langle\psi_1(x)|x\cdot\psi_2(x)\rangle|^2\cdot t\cdot\delta(\Delta\omega-\omega_L). \quad (2.20)$$

Finally, the transition rate of the electron in response to a perturbation from light with energy $\hbar\omega_L$ is given by

$$\frac{dW_{12}}{dt} = \left(\frac{eE_0}{2\hbar}\right)^2|\langle\psi_1(x)|x\cdot\psi_2(x)\rangle|^2\delta(\Delta\omega-\omega_L). \quad (2.21)$$

The inner product $\langle\psi_1(x)|x\cdot\psi_2(x)\rangle = M_{12}$ are the dipole matrix elements, which are discussed further in the next section. To gain insight into CNT absorption I will treat the dipole matrix element as a constant and generalize this result from a 2-state system to a system with many transitions in the next section.

2.4 Fermi's Golden Rule

The section generalizes the result from the previous section for a transition between two states with energy E_1 and E_2 to a transition from a state with N states with energy difference ΔE. Further reading on the derivation of Fermi's golden rule can be found in textbooks.[70–72] Many prefer an alternative approach that requires less approximations.[73] Figure 2.2 shows the new system which encorporates an energy band that has multiple states at each energy.

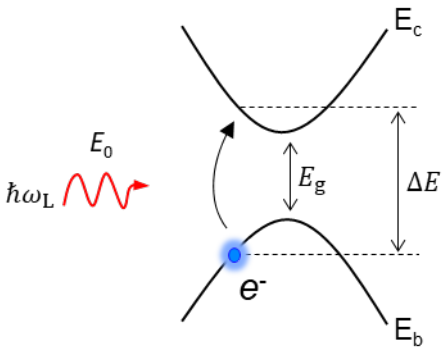

Figure 2.2 A depiction of a transition between states separated by an energy ΔE in a semiconductor with parabolic valence and conduction bands labeled E_b and E_c respectively.

Taking the product of the number of states separated by ΔE with the transition rate and integrating over ΔE will give the total transition probability, W_{if}, between any two initial and final states separated by ΔE. The number of states separated by energy ΔE can be found from the joint density of states, $g_r(\Delta E)$. For a system like a CNT, the one-dimensional joint density states is given by

$$g_r(\Delta E) = \frac{1}{\pi\hbar}\left(\frac{m^*}{2(\Delta E - E_g)}\right)^{\frac{1}{2}} \tag{2.22}$$

where E_g is the band gap and m^* is the effective mass. The total transition rate between all of the initial and final states separated by energy ΔE is given by

$$W_{\text{if}} = \int_{E_g}^{\infty} g_r(\Delta E)\, W_{12}(\Delta E) d\Delta E \propto \int_{E_g}^{\infty} g_r(\Delta E)\, \delta(\Delta E - \hbar\omega) d\Delta E \tag{2.23}$$

which leads to the final expression for the transition rate between states separated by energy ΔE

$$W_{\text{if}} = \frac{2\pi e^2}{\hbar} |\langle i|\boldsymbol{E}\cdot\boldsymbol{x}|f\rangle|^2 g_r(\hbar\omega)\,. \tag{2.24}$$

This is a well known result that predicts the transition probability per unit length of an electron in a one dimensional material. The qualitative features of the transition rate are strikingly different from a 3-D material. Notably, the density of states diverges at $\Delta E = E_g$ which are called Van Hove singularities. These features have been observed in STM measurements, which measure the density of states (not the joint density of states) of the CNT band structure.[74]

This far the dipole matrix elements have been ignored and treated as a constant. They have an important role in the absorption properties of the system. One immediate consequence of the dipole matrix elements is a polarization dependent transition rate. Consider the symmetry of the system shown in Figure 2.3. The matrix elements for light polarized on the *x* and *y* axis are equivalent, but light on the z-axis are not expressed by

$$\langle i|x|f\rangle = \langle i|y|f\rangle \neq \langle i|z|f\rangle. \tag{2.25}$$

In summary, consideration of a two-state system resulted in a tractable mathematical result that ultimately captured the effect of confinement on the electronic states and transition rates in CNTs. In addition, it introduced a polarization dependence to the optical transition rate. Another major effect of confinement is a change in electron-hole interaction strength. In CNTs the interaction strength dominates over thermal energy and excitons play a major role in their optical absorption. In the next section I'll discuss bound states and excitonic effects.

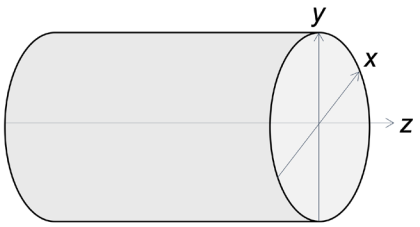

Figure 2.3 The axes of the carbon nanotube.

2.5 Effect of confinement on electron energy states

In the following sections I'll discuss the role of excitons in CNTs and how the light-matter interations are dramatically changed due to the dominant role that excitons play in the system. When the absorption of a photon creates an electron in the conduction band, a Coulomb attraction to the hole left behind creates a bound state. Due to this interaction, the bound state has a higher probability of formation than a free electron. Under the right conditions, the bound state is stable under thermal fluctuations. Confinement plays an important role in determining the energy states of the exciton.

To show the effect that confinement has on the energy states, I'll calculate and compare the energy states in 3D and 2D. This calculation is taken from excercises in *Optical Properties of Solids* by Mark Fox.[72] The variational principle states that the energy state that minimizes the energy will be the closest to the true ground state energy of the system. To be relevant to how the ground-state energies of an exciton is modified, it makes sense to consider a normalized 1s hydrogenic wavefunction of the form

$$(r,\theta,\phi) = \left(\frac{1}{\xi}\right)^{\frac{3}{2}} \exp\left(-\frac{r}{\xi}\right) \tag{2.26}$$

where ξ is the variational parameter. The Hamiltonian is given by

$$H = -\frac{\hbar^2}{2\mu}\nabla^2 - \frac{e^2}{4\pi\epsilon r}. \tag{2.27}$$

where μ is the reduced mass. In 3D, the expectation value of the energy is given by

$$\langle E\rangle = \int_0^{\infty}\int_0^{\pi}\int_0^{2\pi} \psi^* H\psi r^2 \sin\theta \, dr d\theta d\phi \tag{2.28}$$

The calculation is made much easier by the fact that the wavefunction only depends on *r*. And thus, the term $H\psi$ in the integral is given by

$$H\psi = -\frac{\hbar^2}{2\mu r^2}\frac{\partial}{\partial r}\left(r^2\frac{\partial\psi}{\partial r}\right) - \frac{e^2}{4\pi\epsilon r}\psi = \left[\frac{-\hbar^2}{2\mu\xi^2} + \frac{\hbar^2}{\mu\xi r} - \frac{e^2}{4\pi\epsilon r}\right]\frac{1}{\pi\xi^3}\cdot\exp\left(-\frac{r}{\xi}\right) \tag{2.29}$$

Therefore the energy is

$$\langle E\rangle = 4\pi\frac{1}{\pi\xi^3}\left[\frac{-\hbar^2}{2\mu\xi^2}\int_0^{\infty} r^2 e^{-\frac{2r}{\xi}}dr + \left(\frac{\hbar^2}{\mu\xi} - \frac{e^2}{4\pi\epsilon}\right)\int_0^{\infty} r\, e^{-\frac{2r}{\xi}}dr\right] = \frac{\hbar^2}{2\mu\xi^2} - \frac{e^2}{4\pi\epsilon\xi} \tag{2.30}$$

where the first integral is normalized to 1, and the second becomes $\xi^2/4$. Now using the variational principle to minimize the energy with respect to ξ, the minimum is when $\xi_{\min} = 4\pi\epsilon\hbar^2/\mu e^2$ which corresponds to a minimum energy of

$$\langle E\rangle_{\min,3D} = \frac{-\mu e^4}{2(4\pi\epsilon\hbar)^2}. \tag{2.31}$$

that has a radius of

$$r_{\text{ex}} = \frac{4\pi\epsilon\hbar^2}{\mu e^2}. \tag{2.32}$$

The variational method gave exactly the same answer as the well known ground state $E_{x1} = \frac{-\mu}{m_0 \epsilon_r^2} \mathrm{R_H}$ where $\mathrm{R_H}$ is the Rydberg energy with exciton radius is given by $a_\mathrm{B} = \frac{m_e \epsilon_r}{\mu} a_B^H$. This worked well both because we knew correct wavefunction from the start, and it happened to have a tractable mathematical solution.

To show how the energy states change due to confinement, I will do the same procedure in 2D. in this case, the normalized wavefunction is

$$\psi(r,\theta) = \left(\frac{2}{\pi\xi^2}\right)^{\frac{1}{2}} \exp\left(-\frac{r}{\xi}\right). \tag{2.33}$$

I'm using ∇^2 in polar coordinates this time, noting the azimuthal symmetry which makes the $\partial\psi/\,\partial\theta$ terms are zero. The value for $H\psi$ is now

$$H\psi = -\frac{\hbar^2}{2\mu r}\frac{\partial}{\partial r}\left(r\frac{\partial\psi}{\partial r}\right) - \frac{e^2}{4\pi\epsilon r}\psi = \left(\frac{-\hbar^2}{2\mu\xi^2} + \frac{\hbar^2}{2\mu\xi r} - \frac{e^2}{4\pi\epsilon r}\right)\psi \tag{2.34}$$

where the integration will only be over two-dimensions. Calculating the energy yields

$$\langle E\rangle = \frac{-\hbar^2}{2\mu\xi^2}\int_0^\infty\int_0^{2\pi} \psi^*\psi r dr d\theta + \left(\frac{\hbar^2}{2\mu\xi} - \frac{e^2}{4\pi\epsilon}\right)\int_0^\infty\int_0^{2\pi} \psi^*\psi dr d\theta. \tag{2.35}$$

where first integral is normalized to 1 and the second becomes $\frac{2}{\xi}$ which yields the energy

$$\langle E\rangle = \frac{\hbar^2}{2\mu\xi^2} - \frac{e^2}{2\pi\epsilon\xi}. \tag{2.36}$$

Minimizing this with respect to ξ gives $\xi_{\min} = \frac{2\pi\hbar^2\epsilon}{\mu e^2}$ which corresponds to

$$\langle E\rangle_{\min,2\mathrm{D}} = -\frac{\mu e^4}{8(\pi\epsilon\hbar)^2} \tag{2.37}$$

which has a magnitude four times larger than the 3-dimensional case. A CNT is even more confined than an exciton in three-dimensions. It follows that an even larger modulation in the exciton energies is expected. Furthermore, charges in a CNT experience less dielectric screening and the energy scales with ϵ^{-2}. With this calculation in consideration and reduced dielectric screening, excitons should play an important role in CNTs.

Due to the Coulomb attraction, the probability of forming a bound electron-hole pair is higher than a free-particle transition. Exciton absorption peaks are readily observed in CNTs at

room temperature because $E_{\mathrm{ex}} \gg k_{\mathrm{B}}T$. Because of that, exciton features dominate the absorption spectrum of CNTs.[23]

2.6 Ionization field of excitons

The central focus of this thesis is to understand how photocurrent generation efficiency changes in response to external electric field. It is sensible to gain intuition by considering familiar Hydrogenic exciton system. In an exciton, the field the electron feels from the hole is approximately E_{ex}/er therefore the ionization field is given by

$$F_{\mathrm{i}} \approx \frac{E_{\mathrm{ex}}}{er_{\mathrm{ex}}}. \tag{2.38}$$

A quick estimate of the ionization field for a binding energy of $E_{\mathrm{ex}} = 250$ meV with a radius $r_{\mathrm{ex}} = 2.5$ nm suggests F_{i}~100 V/μm. This field is about ten times larger than we can achieve experimentally (see Chapter 5.4), but we note that quantum tunneling will become significant at a much lower electric field.

The exciton size, r_{ex}, is a function of the excition energy, E_{ex}. Therefore, we would like to rewrite Eq as function of E_ex alone. For this purpose, consider the potential energy landscape depicted in Figure 2.4 described by the equation

$$V(x) = -\frac{e^2}{4\pi\epsilon x} - F_0 ex \tag{2.39}$$

where F_0 is the field. The function described by Eq 2.39 has a maxima in the domain $x > 0$ which can be found from

$$\frac{dV(x)}{dx} = \frac{e^2}{4\pi\epsilon x^2} - F_0 e = 0\,. \tag{2.40}$$

Plugging the location of the maximum $x = \sqrt{\frac{e}{4\pi\epsilon F_0}}$ back into the potential we find

$$V_{\max} = -2\sqrt{\frac{F_0 e^3}{4\pi\epsilon}}\,. \tag{2.41}$$

As the field increases, the height of the maximum decreases. We estimate that exciton ionization will occur when the maximum crosses the exciton binding energy (as is depicted in Figure 2.4). Setting Eq. 2.41 equal to E_{ex} and solving for F_0 gives

$$F_{\mathrm{i}} = \frac{\pi \epsilon E_{\mathrm{ex}}^2}{e^3}. \tag{2.42}$$

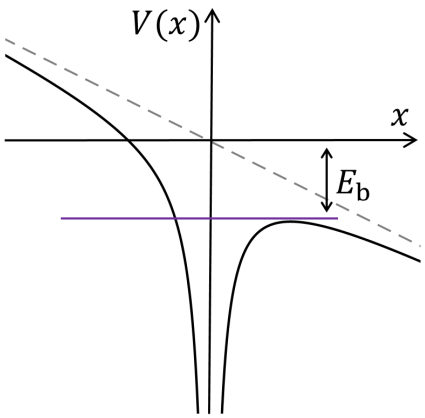

Figure 2.4 A Coulomb potential with a DC electric field with the exciton binding energy indicated.

Figure 2.5 shows the prediction of Eq. 2.42 (blue curve). More exact results using solutions to the Bethe-Salpeter equation are shown for comparison (open cirlces and orange trend line).[59] The estimated field from Eq. 2.42 has the correct quadratic dependence, and the correct order of magnitude. However, Eq 2.42 is a factor 4 lower than the more exact results. The discrepancy may be explained by a simplifying assumption made in deriving Eq 2.42: we incorrectly assumed that exciton binding enery is unaffected by electric field. Section 2.7 shows that the hydrogenic ground state energy becomes lower in the prescence of an electric field, which would explain a larger ionization field.

So far the ionization field analysis has ignored the possibility of tunneling. The more exact results calculated the probability that the electron tunnels from a tilted Coulomb potential. A large fraction of S_{11} excitons are predicted to dissociate at $\sim 10\ \mathrm{V/\mu m}$ if $E_{\mathrm{ex}} \sim 200$ meV.[59]

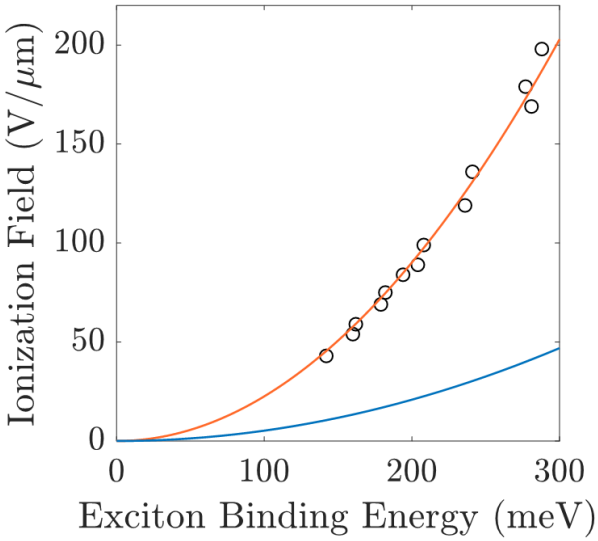

Figure 2.5 The estimated ionization field versus the exciton binding energy from the simple model described by Eq. 2.42 (blue). The ionization field calculated using solutions to the Bethe-Salpeter equation (circles) with a quadtratic fit (orange).[59]

2.7 Excitonic Stark effect

Analagous to a hydrogen atom, the energy levels of an exciton will shift when in an external electric field. In this discuss I'll treat the field as a perturbation in which the system has an unperturbed Hamiltonian of

$$H_0 = \frac{\boldsymbol{p^2}}{2\mu} - \frac{e^2}{4\pi\epsilon r} \tag{2.43}$$

which has ground state energies given by Eq. 2.31. The dipole moment is

$$\boldsymbol{d} = -e\boldsymbol{r}. \tag{2.44}$$

The perturbation Hamiltonian is the potential energy of the dipole, which for an electric field in the z-direction is given by

$$H' = -\boldsymbol{d} \cdot \boldsymbol{E} = eF_0 z \tag{2.45}$$

where E_0 is the strength of the field. Therefore, the first order perturbation is

$$E^{(1)} = eF_0\langle 1s|z|1s\rangle = eE_0 \int z|\psi(r,\theta,\phi)|^2\, dV. \tag{2.46}$$

This integrates to zero since z has odd parity with $\langle z \rangle = 0$ and the wavefunction squared has even parity. Therefore, I'll consider the energy of the second order perturbation which is given by

$$E^{(2)} = e^2 F_0^2 \sum_{n=2}^{\infty} \frac{|\langle 1|z|n\rangle|^2}{E_1 - E_n}.$$

From this, we expect the Stark shift to have a quadratic dependence on electric field. The infinite sum is challenging to deal with exactly, therefore I will make some approximations to get a rough estimate of the magnitude of Stark shifts to expect at the highest fields used in the experiment ($\sim 10\ V/\mu\text{m}$).

Revisiting the parity of the hydrogenic states, for all of the odd values of n, $\langle 1|z|n\rangle = 0$. I'm interested in estimating the magnitude of the Stark shift so I'm going to make approximations to evaluate the infinite sum. The dominant term in the sum will be the $n = 2$ state as they scale with $1/(E_1 - E_n)$, therefore I will only consider that term. The other approximation I'll make is that the integral will be on the same order as the exciton radius and therefore

$$\langle 1|z|n\rangle \approx r_{\text{ex}}.$$

To find the difference in the binding energies $(E_1 - E_2)$, I'll rely on experimental results which used two photon excitation to directly measure the energy difference the 1s and 2p exciton states. They found $(E_1 - E_2) = 300$ meV for nanotubes with a diameter of $D = 0.77$ nm and an exciton radius $r_{\text{ex}} \approx 1.2$ nm.[23] All together this becomes

$$E^{(2)} \approx \frac{-e^2 F_0^2 r_{\text{ex}}^2}{(E_2 - E_1)} = -0.5 \text{ meV}$$

for a field $F_0 = 10\ \text{V}/\mu\text{m}$. The nanotubes used in the experiments in this thesis have $D \approx 2.5$ nm. The energies are inversely proportional to diameter. If the exciton radius increases by the same factor then the expected shift becomes $E^{(2)} \approx -5$ meV. Section 4.2.1 discusses more exact predictions of the Stark shift.

3 Device background

This chapter describes the device geometry and fabrication process for dual-gated, fully suspended CNTs. Figure 3.1a shows the main features of these devices. A single CNT is suspended between source-drain electrodes and above two gate electrodes. Figure 3.1b shows an SEM image of an actual device. The two gate electrodes are in the trench below the nanotube. By applying opposite gate voltages (V_{g1}= -V_{g2}) a pn-junction can be formed in the CNT. This device is the basis for the field-dependent photocurrent studies described in this thesis.

Suspended CNTs are grown over the trench using a fast-heat chemical vapor deposition process (see §3.2) as the final fabrication step, which keeps them from being exposed to photoresist and other chemicals during fabrication.

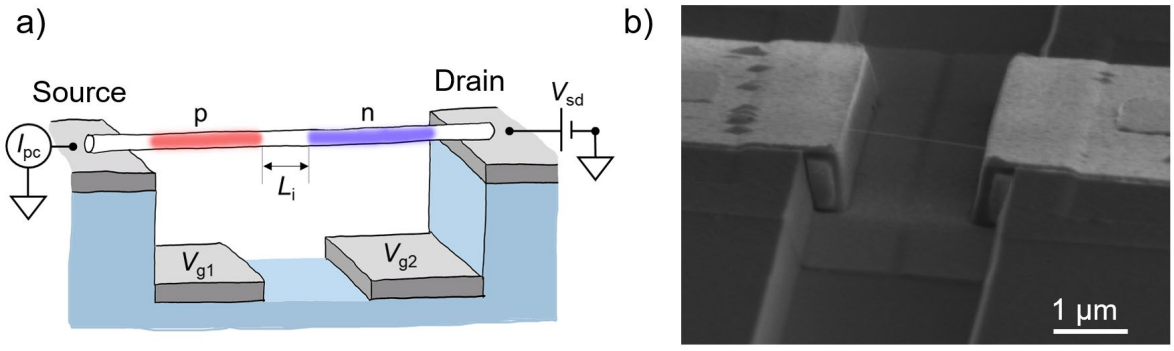

Figure 3.1 a) Schematic of split-gate electrode configuration creating a pn junction in a CNT. The blue is SiO_2 and the grey is platinum. b) An SEM image of the suspended CNT device.

3.1 Device dimensions

A 3-inch wafer of degenerately doped p++ Si is divided into approximately 200 die. The p++ silicon can serve as a back gate and maintains conductivity a low temperatures (this layer is not depicted Figure 3.1a as it is grounded during all experiments described in this thesis). Each die has a total of 48 source electrodes. There are two drain electrodes that can each connect with half 24 of the sources when a CNT bridges the gap. The common drain allows fast probing of the chip, and using 48 growth sites means there is a high likelihood of finding quality nanotubes after a growth (described further in §3.2). For high voltage measurements, there is a tradeoff between probing speed and risk that a leakage between the drain and gate ruins multiple devices.

The trench between the source-drain electrodes is 2.6 μm wide. The top of the source-drain electrodes is 650 nm above the top of the gate electrodes. The layer of SiO_2 between the source-drain electrodes and the gates is 600 nm thick. The separation distance between the gate electrodes is 500 nm. The actual chip dimensions can vary by 10 – 100 nm from the nominal dimensions.

Oxide thickness and the separation distance between electrodes can be increased to reduce the chance of leakage. One modification made for this work was to increase the separation distance between the gate electrodes. In previous designs used by Lee Aspitarte, the gate electrodes were separated by 250 nm rather than 500 nm. The trench separation distance was increased from 2 μm to 2.6 μm. We chose not to make dramatic changes so that the nanotube yield wasn't impacted.

3.2 Nanotube growth

A square of iron catalyst (seen in Figure 3.1b) is deposited on top of the source and drain electrodes 2 μm from the edge of the trench by patterning a photoresist mask and evaporating 2 nm of Ti, 30 nm, SiO_2, and then between 0.6 – 3 nm of Fe. Several growth factors can influence the diameter of the nanotubes including the growth gas composition[75] as well as the temperature and and catalyst thickness.[76]

The chip is placed inside of a one-inch diameter quartz tube within a tube furnace. Prior to heating the furnace, the chamber is purged for 3 minutes with the growth gasses. The chip is left in the cool region of quartz tube (outside the furnace) while the furnace heats to 800 °C. Once the furnace reaches 800 °C, the chip is shuttled into the hot zone of the tube furnace and annealed in H_2 gas for 1 minute (0.45 SLM) to chemically reduce the Fe catalyst. While the chip is in the hot zone, the gases are switched to a 2:1 mixture of ethanol and methanol vapor carried by Ar and H_2.[77] To create this growth gas, Ar is bubbled through reservoirs of liquid ethanol and methanol (the ethanol and methanol are kept at room temperature). Ar is bubbled through ethanol a rate of 0.15 SLM and Ar is bubbled through methanol at a rate of 0.3 SLM. The Ar + ethanol vapor, Ar + methanol vapor are combined with H_2 flowing at 0.45 SLM. The total flow rate of growth gases is 0.9 SLM. After 5 minutes, the gas flow is switched to 1 SLM Ar. The chip is promptly shuttled back into the cool region of the tube.

There are a few complications that can arise during the growth process. The growth process works best if the reservoires of methanol and ethanol are kept between 1/3 to ¾ full. Over or under filling the reservoires can increse or decresase the nanotube yield (respectively). A log of growth results is kept to keep track of the growth conditions and nanotube yield. The log suggests higher humidity in the room decreases nanotube yield, therefore a plastic tent was installed around the furnace with a dehumidifier inside to control the ambient humidity. Another complication during growth is the accumulation of a white/blue residue on the metal contacts after growth. A small amount of residue doesn't seem to impact the device performance, but a lot of residue can lead to low yield. Figure 3.2a shows an optical microscope image of a chip without much residue and Figure 3.2b shows a chip with a lot of residue.

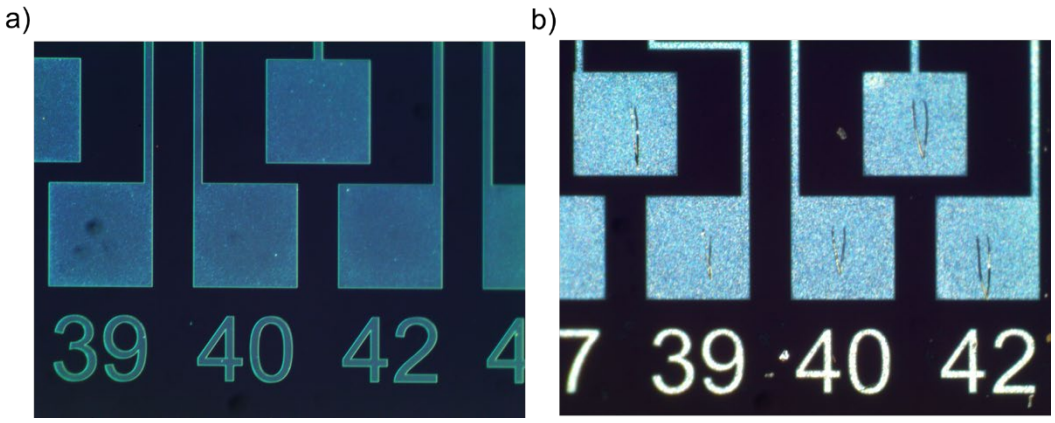

Figure 3.2 a) Optical microscope image of an electrode surface after CNT growth without much residue. **b)** Optical microscope image of an electrode surface after growth with residue. The scratches on the contacts were made while probing the chip and are related to the residue.

3.3 Transport Properties

The device depicted in Figure 3.1a can be used as either a field-effect transistor (FET) or as a diode, depending on the operating conditions. First, consider the FET mode. The split-gates are operated as a single gate ($V_{g1} = V_{g2}$). By meauring I_{sd} as a function of V_g the FET properties can be examined. The I-V_g curve can be used to quickly find single CNTs and assess their quality. The two main indicators of the device quality are the amount of hysteresis and the steepness of the transition from off-state to the on-state. Figure 3.3a shows a typical distribution of CNT FETs present on a chip after growth. The lack of hysteresis in the curves indicates they are

suspended and not in contact with the substrate below. The resistance of the nanotube (at V_g = -10 V) is typically in the range 10 MΩ – 1 GΩ which depends primarily on the contact resistance but the CNT bandgap as well.

The shape of the I-V_g curve provides information about the device quality. Figure 3.3b shows ideal transistor behavior acting as a switch with a sharp turn-on, and little to no hysteresis between forward and reverse traces. In the off state ($V_g \gtrsim -1$ V) the current is limited by the lack of carriers in the nanotube. As charge is added to the tube eventually a saturation current is reached and the conductance will stop changing with gate voltage ($V_g \lesssim -10$ V). In this regime the current is limited by the contact resistance.

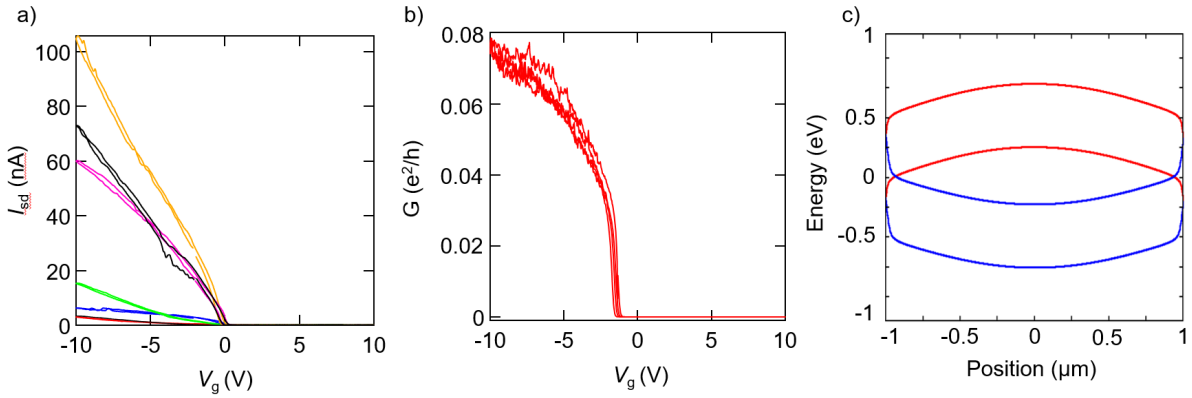

Figure 3.3 a) The variety of FET transport curves (V_{sd} = 25 mV) that can be expected for semiconducting CNTs on a good growth. **b)** An ideal CNT FET curve with a sharp turn-on and minimal hysteresis. c) Simulated band-bending diagram for $V_g < 0$ (red) and $V_g > 0$ (blue) for a CNT with E_g = 0.53 eV.

The suspended CNT devices can also be operated as a diode, as shown in Figure 3.1a. When $V_{g1} = -V_{g2}$, a pn-junction forms. The left side of the CNT electrostatically couples to the left gate, doping it with holes. Similarly, the right half of the CNT becomes n-doped. The diode transport properties can be characterized by measuring an I-V_{sd} curve, which can be understood through the non-ideal diode equation given by

$$I_{sd} = I_0\left(e^{\frac{eV_{sd}}{nk_BT}} - 1\right), \tag{3.1}$$

where I_0 is the dark saturation current, k_B is the Boltzmann constant, T is the temperature, and n is the ideality factor. Figure 3.4 shows a typical I-V_{sd} for the device design shown in Figure 3.1a. In forward bias there is an exponential turn-on whereas in reverse bias the diode displays

rectifying behavior with only the dark saturation current present. The large n-type Schottky barrier at the Pt contacts (in ambient environment) leads to dark saturation currents below the measurement level of our system (< 1 pA).[64] The ideality factor can range from 1 – 2. The CNT diodes made in these experiments typically have $n \approx 1.2$, but can be in the range 1.0 – 1.4.

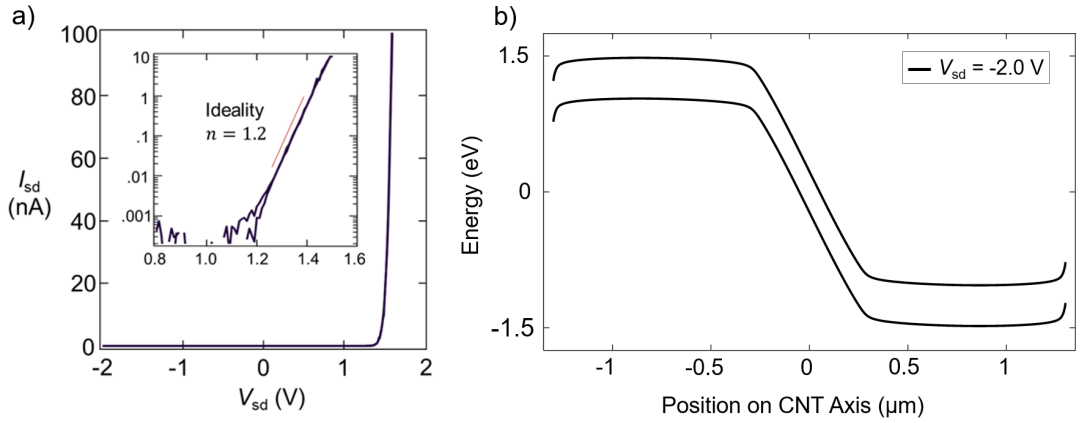

Figure 3.4 a) The Dark I-V_{sd} curve of a suspended carbon nanotube pn junction with $V_{g2} = -V_{g1} = 5$ V. **b)** Simulated band bending diagram for $V_{g1} = -V_{g2} = 5$ V with $E_g = 0.53$ eV.

3.4 Device Stability

The growth process described in §3.2 produces an ultra-clean system, ideal for measuring quantum transport phenomena. The devices can continue to perform for days to weeks after growth.[61,63] While the system can remain ultra-clean, the transport properties will change over time depending on the environment.[64] Figure 3.5 shows data taken by Lee Aspitarte (a former graduate student in the Minot lab) of a nanotube FET curve over time while left in vacuum. Immediately after growth (Day 0 curve), the device has a fully p-type contact indicated by high currents when doped with holes and currents below the noise level of system when doped with electrons. After 15 days in vacuum, the nanotube shifts from a fully p-type contact towards an ambipolar contact.

A possible explanation is that oxygen/surface adsorbates are removed from the contact when the device is left in vacuum for several days which causes the work function of the metal electrodes. When the alignment of the nanotube bands with the work function of the contact changes, the relative sizes of the n and p-type Schottky barriers change. As the n-type Schottky

barrier becomes smaller (and the p-type Schottky barrier becomes larger) the transport changes from favoring p-type conductance towards ambipolar. Lee Aspitarte has done further work in suspended nanotube devices studying the relationship between the transport properties of nanotube pn-junctions and the work function of the contacts.[64]

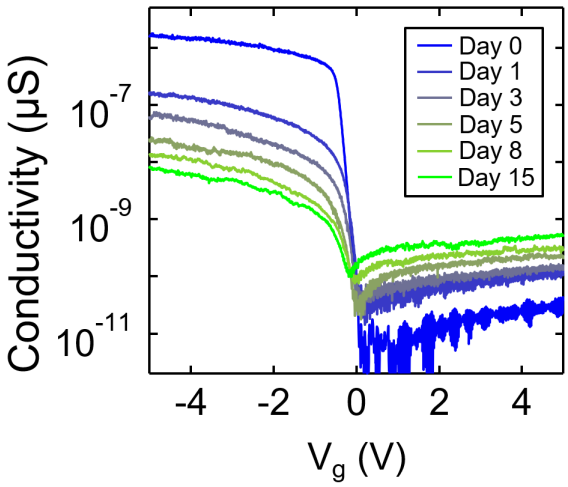

Figure 3.5 The change over time of the CNT FET curve while the device is left in vacuum and shifts from p-type toward n-type contact. This data was taken by Lee Aspitarte and his published work discusses it in further detail.[64]

3.5 Exceptional properties of the suspended CNTs

The devices are stable enough that after shipping them through the mail they exhibit low-temperature electron transport with phase coherence lengths greater than 2 μm. Our collaborators in Vikram Deshpande's group at University of Utah used the shipped CNTs to measure quantum interference phenomena.[61] They were able to observe Fabre-Perot oscillations as well as Sagnac electron interference related to the nanotube structure.[78,79] In some instances the CNT samples were shipped back and forth between OSU and University of Utah, surviving multiple shipments.

In more recent work, the Utah group was able to form a Wigner crystal and extract the compressibility of the electrons in the crystal.[61] They accomplished this by measuring the energy required to add an electron to the crystal. As more electrons are confined within the same amount of space the addition energy increases. By calculating the change in addition energy with increasing electron number they were able to extract the compressibility of electrons in the crystal. While the collaboration has ultimately been a success, there were challenges maintaining

sample quality. The next section describes the measures that were taken to address growth and shipment complications.

3.6 Optimizing nanotube growth and shipment

Numerous CNT shipments failed to provide clean CNTs both from issues during shipment and nanotube growth. This section describes what I learned about optimizing growth and shipment of CNTs. Section 3.2 discusses many of the challenges associated with the growth process. After addressing those challenges, the loss of nanotubes during shipment was the other main difficulty.

CNTs were probed before and after shipment to determine if the devices die during the process. During some shipments all of the devices were broken which motived a more secure way to package the chips. The initial precedure was to tape the chips down in chip carrier, vacuum pack the chip carrier, and ship it in a padded envelope. The chip carriers were packed in foam within a box to prevents direct contact with the chip carrier during shipmentn which showed improvement in the nanotube survival rate. The environment was also changed from a vacuum seal to a nitrogen environment to improve the stability. The chip carrier was placed within a ziplock bag and the bag was sealed around the end of the N_2 gun. The air was flushed out by N_2 gas for 30 seconds before removing the N_2 gun and immediately sealing the bag (careful to minimize exchange of air). We found that the dry nitrogen environment worked well to preserve the quality of I_{sd} vs V_g curves.

In summary, the humidity in the tent should be below 30% during growth, the chip should show no major signs of residue on the surface, the chip carrier should be sealed in a nitrogen environment and cushioned within a rigid container to minimize shock during transport.

4 Computational modeling

This chapter discusses three computational simulations used as part of the process I used to determine the PCQY from CNT photocurrent spectra. The first is self-consistent electrostatics simulations of the axial electric field (§4.1). The simulations were performed by our collaborator Dr. Andrea Bertoni at CNR Nano in Italy. The second is solutions to Bethe-Salpeter equation used to understand how the electric field influences the exciton decay dynamics (described in §4.2). These simulations were performed by our collaborator Dr. Vasili Perebeinos in Dept. of Electrical Engineering at SUNY Buffalo. The third are finite-difference-time-domain (FDTD) simulations to determine how the intensity of light incident on the nanotube is modulated by interference from reflections off the substrate surrounding the nanotube (§4.3). These simulations were performed by Mitchell Senger in the Minot group here at OSU.

4.1 Self-consistent field calculations

The main focus of this thesis is to determine and discuss the relationship between the PCQY and the axial electric field in the nanotube. The method of changing the axial electric field, F, in the suspended CNT devices is by modulating the magnitude of the split gate voltages. The main effect of increasing the gate voltage is to both increase the field and decrease the intrinsic region length, L_i, a key parameter in determing the PCQY.

Measurements of L_i at low field are presented in §5.2.3 as well as in previous work by Lee Aspitarte.[56] At high field, however, L_i is smaller than the point spread function of the laser spot. Therefore, we used self-consistent electrostatic-field (SCF) calculations to find the relationship between the V_{g1}, V_{g2}, V_{sd}, and L_i. In this section I describe the work done by Andrea Bertoni to perform the SCF simulations

Briefly, the first step of calculation finds the electrostatic potential field without any CNT connecting the source and drain electrodes. The voltages on the four electrodes and the cross-sectional geometry of the device (shown in Figure 4.1 and Figure 4.3a) define the electrostatic boundary conditions. The 2-d electrostatic potential field was calculated using a relaxation algorithm to solve the Laplace equation. This zeroth-order solution is a first estimate of the electric field at the center of the pn junction (grey dashed line in Figure 4.3d). In the next step of calculation, the CNT is populated with charge and an effective 1-d mean-field simulation is used to refine the results of the electrostatic potential model. This step is repeated many times until a

self-consistent solution is reached. The final result includes the charge density along the length of the CNT (Figure 4.3b), the band bending diagram (Figure 4.2 and Figure 4.3c), and the electric field at the center of the CNT (open circles in Figure 4.3d).

4.1.1 Self-consistent field calculation methods

As the first step, Dr. Bertoni calculated the electrostatic potential in the absence of the CNT, $V_{\text{ext}}(\mathbf{r})$. Figure 4.1 shows the metallic surfaces (constant potential) that are used as boundary conditions to calculate $V_{\text{ext}}(\mathbf{r})$. A numerical relaxation algorithm is used to solve the 2D Laplace equation in a non-homogeneous dielectric environment given by

$$\frac{\partial}{\partial x}\left[\epsilon(x,z)\frac{\partial}{\partial x}\right]V_{\text{ext}}(x,z)+\frac{\partial}{\partial z}\left[\epsilon(x,z)\frac{\partial}{\partial z}\right]V_{\text{ext}}(x,z)=0, \tag{4.1}$$

where $\epsilon(x,z)$ is the position-dependent relative permittivity of the dielectric environment.

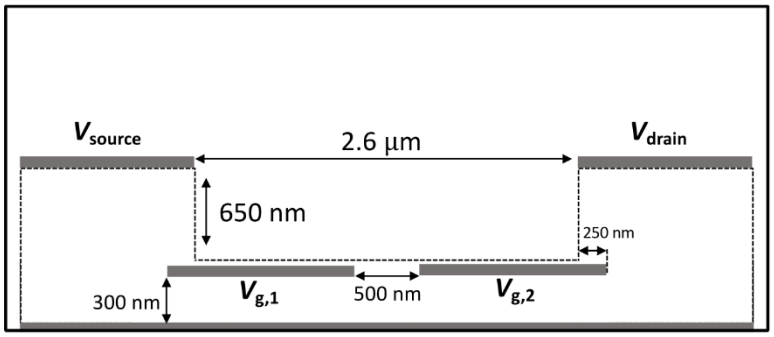

Figure 4.1 Cross sectional diagram of the dimensions used in the simulation. The metal electrode thickness is 60 nm. Dotted lines represent the SiO_2 in the device. We assume translation symmetry in the third dimension.

After computing $V_{\text{ext}}(\text{r})$, the charge on the doped regions of the semiconducting CNT is found by means of a self-consistent cycle as follows. First, the hole and electron concentrations, $n_h(x)$ and $n_e(x)$ respectively, are calculated from

$$n_e(x)=2\sqrt{\frac{m^*k_BT}{2\pi\hbar^2}}\mathcal{F}_{-\frac{1}{2}}\left(\frac{\mu_e-E_{\text{c}}(x)}{k_BT}\right) \tag{4.2}$$

$$n_h(x) = 2\sqrt{\frac{m^* k_B T}{2\pi\hbar^2}}\mathcal{F}_{-\frac{1}{2}}\left(\frac{\mu_h - E_{\mathrm{v}}(x)}{k_B T}\right) \tag{4.3}$$

where m^* is the effective mass of electrons and holes, T is the temperature, μ_{e} is the quasi-Fermi level for electrons, μ_{h} is the quasi-Fermi level for holes, and $\mathcal{F}_{1/2}$ is the complete Fermi-Dirac integral of order 1/2. For the semiconducting CNT, the relationship between m* and the CNT band gap is approximated to be:

$$m^* = \frac{E_{\mathrm{g}}}{v_{\mathrm{F}}^2} \approx m_{\mathrm{e}}\frac{E_{\mathrm{g}}}{[7\ \mathrm{eV}]}. \tag{4.4}$$

Figure 4.3b in the next section shows the net charge (linear charge density) which is given by

$$\lambda(x) = e\big(n_h(x) - n_e(x)\big). \tag{4.5}$$

At each point on the CNT, it is assumed that charge is spread uniformly around the circumference of the CNT. This charge density, $\lambda(x)$, generates an electrostatic potential $V_{\mathrm{int}}(\mathbf{r})$ which modifies the total electrostatic potential in the self-consistent cycle. The latter potential along the length of the CNT is given by

$$V_{\mathrm{tot}}(x) = V_{\mathrm{ext}}(x) + V_{\mathrm{int}}(x). \tag{4.6}$$

From $V_{\mathrm{tot}}(x)$, the energy of the valence band edge, $E_{\mathrm{v}}(x)$, and the energy of the conduction band edge, $E_{\mathrm{c}}(x)$, are found. In order to model the reverse-bias condition, the quasi Fermi level for holes is pinned mid gap at the left electrode and the quasi Fermi level for electrons is pinned mid gap at the right electrode which are given by the conditions

$$E_{\mathrm{v}}(x) = eV_{\mathrm{tot}}(x) - \frac{E_{\mathrm{g}}}{2} \tag{4.7}$$

$$E_{\mathrm{c}}(x) = eV_{\mathrm{tot}}(x) + \frac{E_{\mathrm{g}}}{2}. \tag{4.8}$$

Figure 4.2 shows the self-consistent band diagram at room temperature for $E_{\mathrm{v}}(x)$ and $E_{\mathrm{c}}(x)$ that go together with Figure 4.3c. The split-gate voltages induce hole accumulation on the left side and electron accumulation on the right side. An insulating intrinsic region is formed in the central part, where the two bands show a linear dependence on the position.

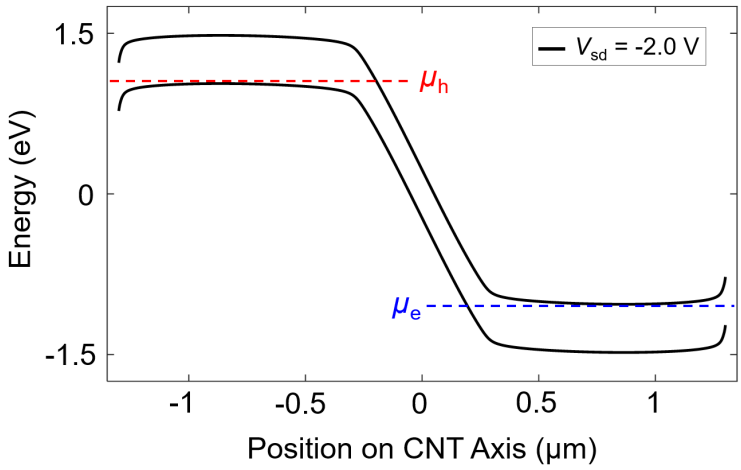

Figure 4.2 The energy bands along the length of the nanotube from SCF calculations. The chemical potential for holes, μ_h, is in equilibrium with the left electrode. The chemical potential for electrons, μ_e, is in equilibrium with the right electrode. We assume the middle of the CNT is insulating.

4.1.2 Self-consistent field calculation results and discussion

This section presents the relationship between V_{sd}, V_{g1}, V_{g2}, L_i, and F determined from the SCF calculations. Section 4.1.1 gives details of the simulations methods. Figure 4.3a shows the layout of the electrodes surrounding the nanotube and illustrates the electric field (orange lines) created by the gate electrodes when $V_{g1} = -V_{g2}$.

Figure 4.3b shows the SCF calculation of charge density along the length of the nanotube for different split gate voltages. The left side of the CNT is doped with holes and the right half is doped with electrons. The region of zero charge in the center of the CNT corresponds to the intrinsic region. The length of the intrinsic region length decreases as the split-gate voltages increase. The next section describes constancy checks on the capacitance between the nanotube and the gates that were determined by the simulation.

Figure 4.3c shows band bending diagrams for different values of V_{sd}. The slope of the band edges in Figure 4.3c correspond to the axial electric field. The field in the center of the CNT, F, is primarily determined by $V_{g1} = -V_{g2}$. Figure 4.3d shows the maximum axial electric field as a function of gate voltage for various source-drain voltages. The grey dashed line shows the zeroith order approximation of the field without taking into accound how the charge on the nanotube impacts the electrostatics. Note in Figure 4.3d that F is almost unaffected by the typical

V_{sd} voltages used in our experiment; the main effect of $V_{sd} < 0$ is to lengthen L_i. In summary, the results of the self-consistent field calculations are well described by the relationship

$$L_i \approx \frac{\left|V_{sd} - E_g/e\right|}{F} \quad \text{when } V_{sd} < 0, \tag{4.9}$$

where E_g is the band gap of the CNT. Eq. 4.9 is plotted in Figure 4.3e (dashed lines) and compared to the exact results of the SCF calculation (open circles).

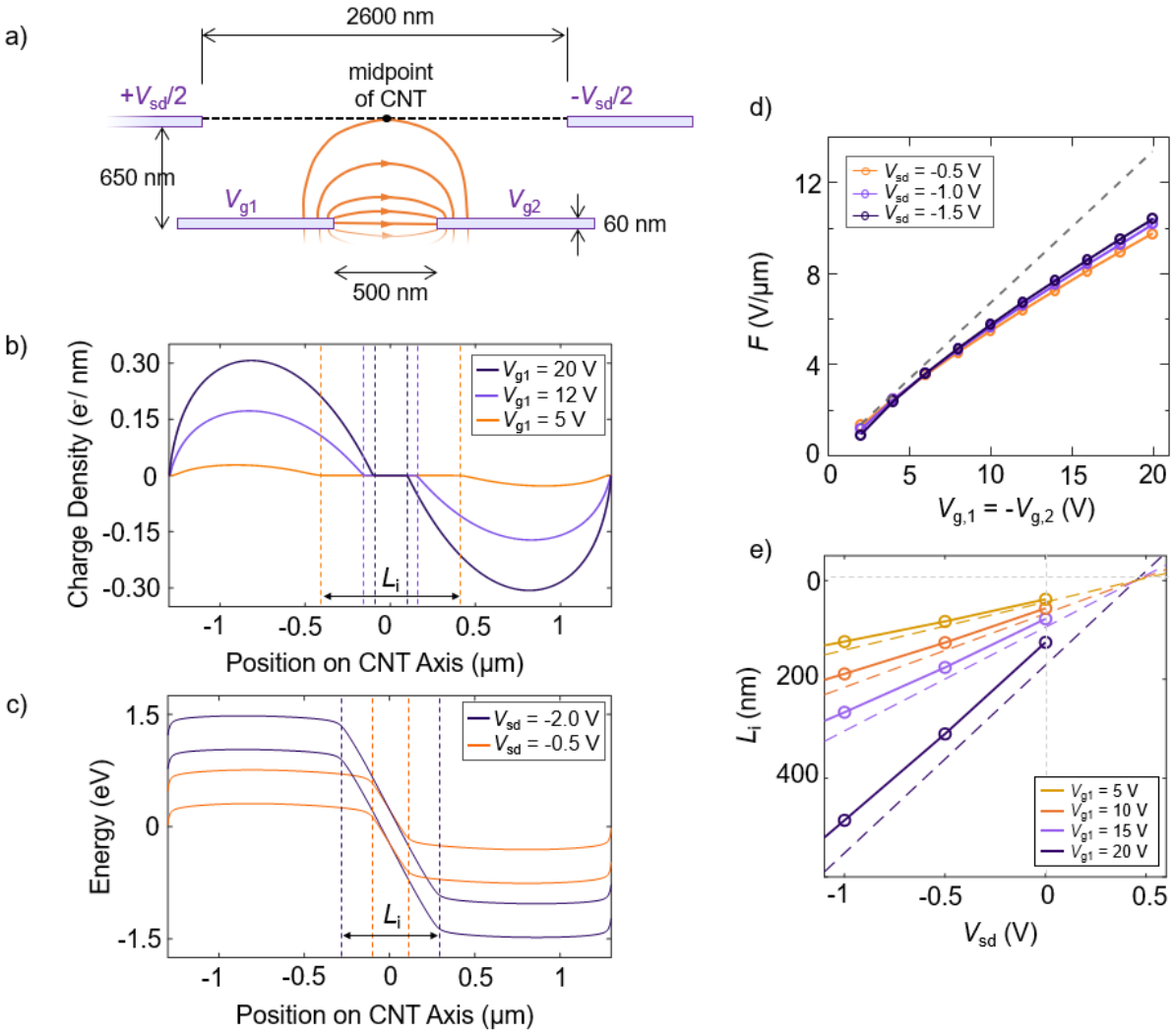

Figure 4.3 a) Schematic of the geometry used in the self-consistent electrostatic-field (SCF) calculations. Electric field lines are sketched in orange. **b)** Calculated charge density along the length of a CNT with E_g = 0.5 eV. The gate voltages are equal and opposite (V_{g1} = -V_{g2}). All three curves are calculated with V_{sd} = 0. **c)** Calculated band bending diagram (the edge of the valance and conduction bands) when $V_{g1} = -V_{g2}$ = 6 V and E_g = 0.5 eV. **d)** The axial-component of electric field at the center of the CNT. The grey dashed line shows the result of a zeroth-order calculation (assuming no charge on the CNT). Open circles show the results of the SCF calculations. **e)** Open circles show the calculated value of the intrinsic region length, L_i. The dashed lines shows values of L_i estimated using Eq. 4.9.

4.1.3 Extracting intrinsic region length from electrostatic modeling

Figure 4.4a illustrates the method for extracting L_i from our SCF electrostatics simulations. The linear charge density in the CNT, $\lambda(x)$, is plotted for various values of V_{sd} when V_{g1} = -V_{g2} =

4 V. The charge density is considered near the center of the CNT in a limited range $-10e\ \mu m^{-1} < \lambda(x) < 10e\ \mu m^{-1}$. When $10e\ \mu m^{-1} > \lambda > 1e\ \mu m^{-1}$, λ changes linearly with respect to position. We extrapolate this linear relationship to the x-axis and thus define the edge of the intrinsic region. Repeating this process on the right edge of this intrinsic region then determines L_i.

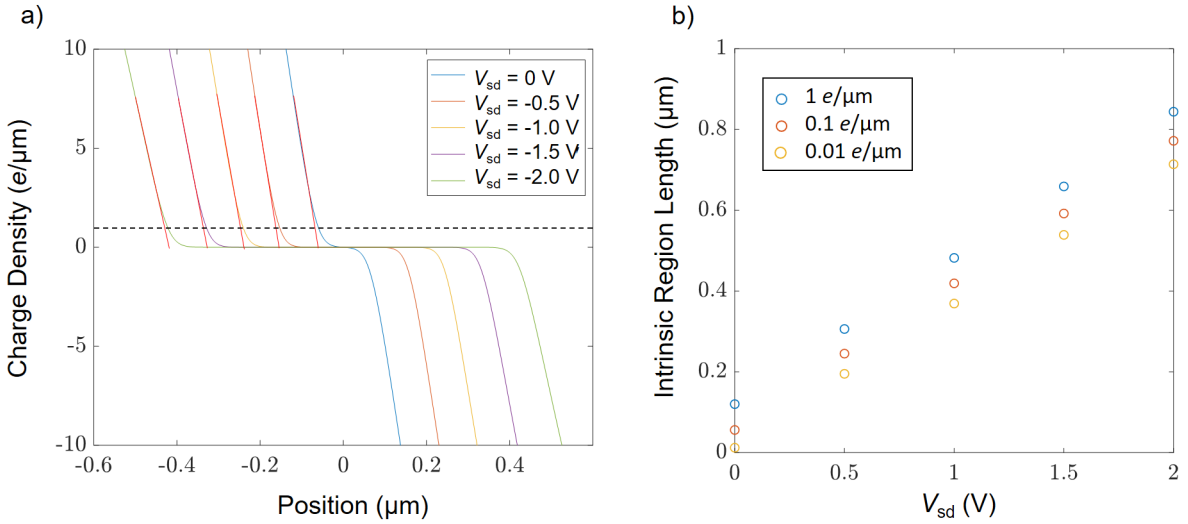

Figure 4.4 a) The charge density along the length of the CNT. Linear fits (red) are extrapolated to the x-axis to find the edge of the intrinsic region with V_{g1} = 4 V. The dashed line shows the value is comparable to using a cutoff charge density of $1e\ \mu m^{-1}$. **b)** The calculated intrinsic region length using different cutoff charge densities.

This extrapolation method is equivalent to setting a threshold $|\lambda| < 1e\ \mu m^{-1}$ to define the intrinsic region. Other threshold levels are considered in Figure 4.4b which shows the measured intrinsic region lengths for a threshold of $1e\ \mu m^{-1}$, $0.1e\ \mu m^{-1}$, and $0.01e\ \mu m^{-1}$. Reducing the threshold level reduces the calculated length of the intrinsic region. For the analysis of photocurrent quantum yield (PCQY), a conservative estimate of L_i is used that will not inflate the values of PCQY. Therefore, the linear extrapolation method is used (Figure 4.4) which results in the largest estimate of L_i.

4.1.4 Cross-check of calculated charge density

To verify the validity of the results from the SCF calculation we consider the capacitance determined by the calculation. Figure 4.5a displays the SCF calculation results for the charge

density of the nanotube in a pn junction configuration at various gate voltage. Figure 4.5b shows the maximum charge density on the p doped side of the nanotube. The maximum capacitance per length can be found from the slope of the line which gives $C_{\mathrm{L}} = 2.7$ aF/μm for the nanotube.

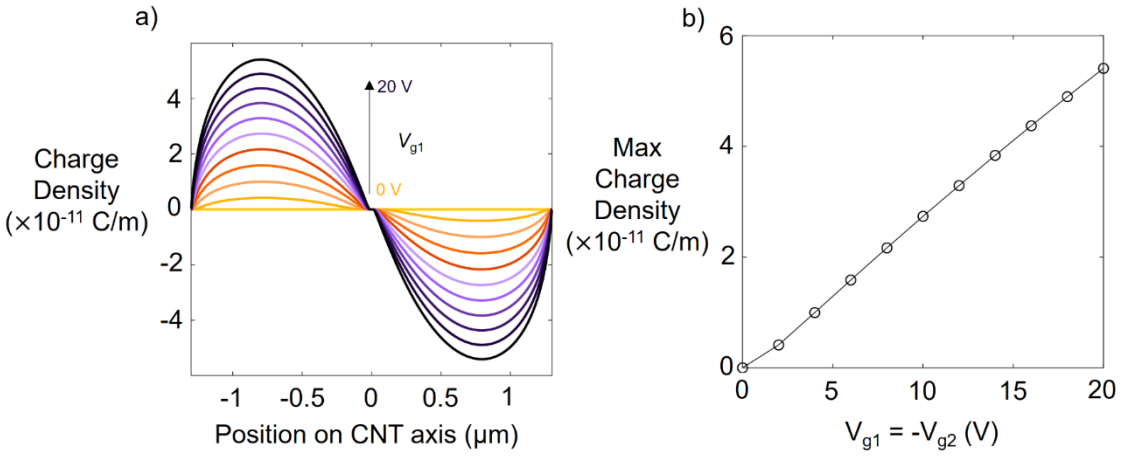

Figure 4.5 a) The charge density along the length of the nanotube as a function of gate voltage with Vsd = 0 V. **b)** The maximum charge density in p doped portion of the nanotube extracted from the SCF simulations shown in a).

An upper bound for the capacitance of the nanotube can be calculated using the simple case of an infinitely long wire over a conducting plane. The capacitance per length of our actual device will be less than that of an infinite wire because each side of the nanotube has some coupling to gate on the other side. The potential, *V,* of a wire with charge density λ can be found by first using method of images to treat the conducting plane as a mirror charge and then using Gauss's law to find the electric field of the two charged wires. Integrating the field gives the potential

$$V = \frac{\lambda \cdot L \cdot \ln\frac{4h}{D}}{2\pi\epsilon_0\epsilon_r} \tag{4.10}$$

where h is the tube height, and D is the diameter of the wire. The capacitance per length is then

$$C_{\mathrm{L}} = \frac{2\pi\epsilon_0\epsilon_r}{\ln\frac{4h}{D}}. \tag{4.11}$$

For h = 650 nm and D = 2 - 3 nm the capacitance is C_{L} = 7.76 – 8.22 aF/μm. The capacitance in the SCF calculation is the same order of magnitude but lower as expected.

A more realistic upper bound can be found through Coulomb blockade spectroscopy of devices with a single back gate. For a single gate device with a 2 micron long CNT suspended 750 nm above the gates, we have measured the capacitance to be CL = 3.5 aF/μm.[56] In this work we are considering the capacitance of half of a split-gate device, therefore, we explicit slightly lower capacitance than a full single gate device.

4.2 Computational modeling of excited states in carbon nanotubes

Modern computing power enables sophisticated approximations of many-body interactions to model real systems with high accuracy. The GW approximation is the state of the art for handling many-body interactions which treats the self-energy of electrons as dynamic unlike less sophisticated approximations. Using the GW approximation in DFT to calculate the ground-state electronic structure has been accomplished for many types of materials including crystals, metals, nanostructures, and molecules.[80] Despite the power of these computational predictions, the have clear limitations. A good example of which is that they do not accurately predict the band gap. Nevertheless, this method has been extended beyond predictions of the ground state system.

The frontier of calculations using the GW approximation is in combine DFT with the Bethe-Salpeter equation to predict the dynamics of electronic excited states. This approach has successfully been applied to the excited states of a wide variety systems including nanomaterials. However, the calculations are computationally intentsive, and therefore it is limited to a subset of the systems that can be modeled in the ground state.[81] Large systems remain a major challenge along with systems with highly localized electronic states or systems with large unit cells.[82] Carbon nanotubes are one of such systems that push the limits of computing power. The accuracy of this approach continues to improve every year. As with any theory predicition, it is most powerful when used in comparison to experimental data. Sections 4.2.1 – 4.2.3 show computed solutions to the Bethe-Salpeter equation for an exciton in a CNT in the presence of an axial electric field which were performed by Dr. Vasili Perebeinos in 2019.

4.2.1 Shift in exciton absorption peak location with field

Solutions to the Bethe-Salpeter equation were used to predict changes in the absorption spectrum of CNTs. Figure 4.6a shows the absorption spectrum around the S_{22} exciton resonance at different electric field strengths. The calculation of the absorption spectrum is performed by

applying Gaussian broadening to the solution of the Bethe-Salpeter equation for an exciton in a static electric field along the CNT axis. Figure 4.6b show the average shift of the S22 exciton resonance for eight chiralities. The peak positions for all eight CNTs show redshifts in response to field with some nonmonatomic behavior. This calculation is compared to experimental data in §5.3.1.

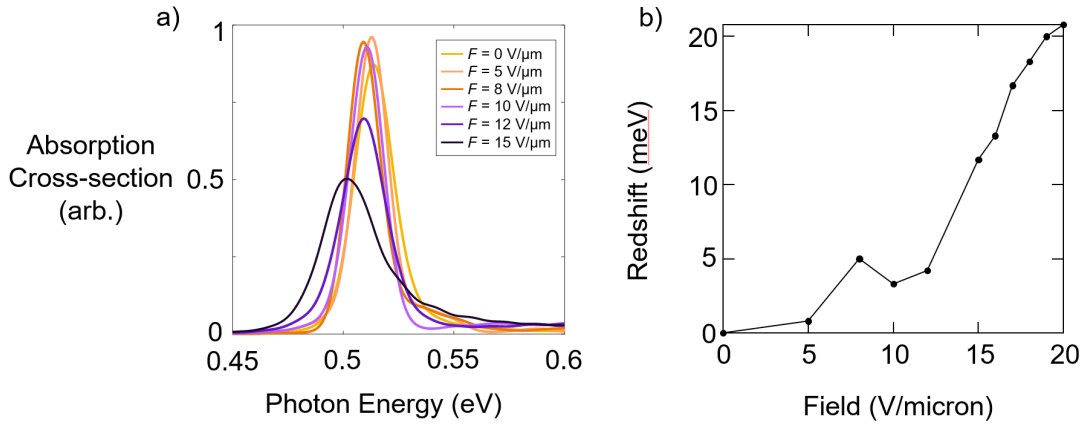

Figure 4.6 a) The calculated absorption spectrum of a (20,16) CNT for difference values of electric field strength. **b)** The calculated average Stark shift of the S_{22} resonance for eight CNTs with different chiralities that are relevant to experiments discussed in chapter 5.

4.2.2 Calculation of change in carbon nanotube oscillator strength

In addition to the position of the absorption peak changing, the shape of the peak changes as well. This section discusses changes in the peak area. The oscillator strength of an exciton resonance in a CNT with a specific chiral index is calculated using the equation[67]

$$\int_{S_{ii}} \sigma_c \, d(\hbar\omega) = \frac{45.9}{(p+7.5)D} \times 10^{-18}\text{eV}\cdot\text{cm}^2, \tag{4.12}$$

where D is the nanotube diameter and p is an integer indexing the optical transitions of both semiconducting and metallic nanotubes ($p = 2$ for S_{22} and $p = 4$ for S_{33}). The atoms per length in the nanotube, N_L, is given by

$$N_L = \frac{4(n^2 + m^2 + 2nm)}{\sqrt{3}a_c}, \tag{4.13}$$

where (n, m) are the chiral indices of the CNT and a_c = 0.14 nm is the carbon-carbon bond length. The absorption cross section per atom, σ_c, can be multiplied by N_L to find an effective absorptive width of the nanotube.

To verify that Eq. 4.12 is valid at large *F*, we calculated the expected absorption cross-section spectrum as a function of *F*. For this calculation, we used the Bethe-Salpeter equation for an exciton in the presence of a static axial electric field similar to the methods used by Perebeinos and Avouris in 2007.[59] Figure 4.7b shows that the oscillator strength decreases by only ~5% at the highest fields used in our experiments.

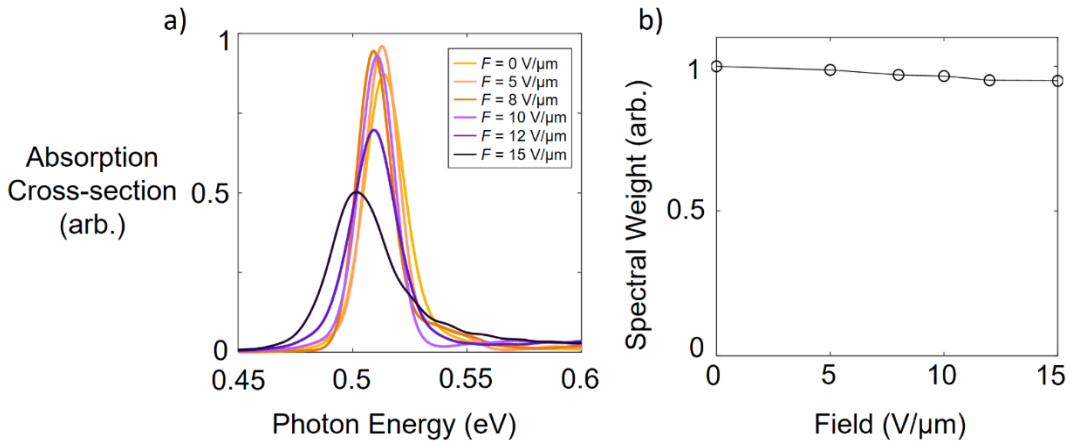

Figure 4.7 a) The calculated S22 absorption for a (20,16) CNT. **b)** The change in oscillator strength with field found by integrating the peaks in a).

4.2.3 Change in spectral width of exciton peaks

While the oscillator strength does not change substantially with field, the peaks widths can. If the width of a peak is lifetime limited, an increase in the peak width with field will correspond to a lower lifetime. Figure 4.8 shows the calculated change in FWHM of the S_{22} absorption peak as a function of field. From the calculation, we expect to see rapid oscillations in FWHM as a function of *F*. We also expect the smallest diameter CNTs to be the least sensitive to field (CNTs D and F). The sharp changes in FWHM with field could be due to the Franz-Keldysh oscillations[59] in the E_{11} continuum which overlaps in energy with the position of the S_{22} exciton. A comparison to data is made in §5.3.2.

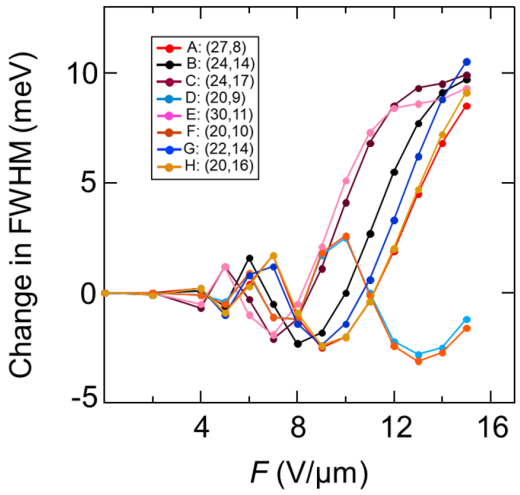

Figure 4.8 Calculated changes in the FWHM of the S_{22} absorption peak as a function of field for eight different CNT chiralities. The changes are relative to FWHM values of 13 – 22 meV. The chiralities shown here are relevant to the experiments discussed in the next section.

Figure 4.9a shows the calculated changes in the S_{11} absorption peak with field. Zero-field broadening of Γ_0 = 15 meV is added to our simulation to match previous measurements by Malapanis et al.[54] There is a monotonic increase in FWHM with field. Figure 4.9a shows the S_{11} absorption peak changing with field for the largest (left) and smallest (right) diameter CNTs in the study.

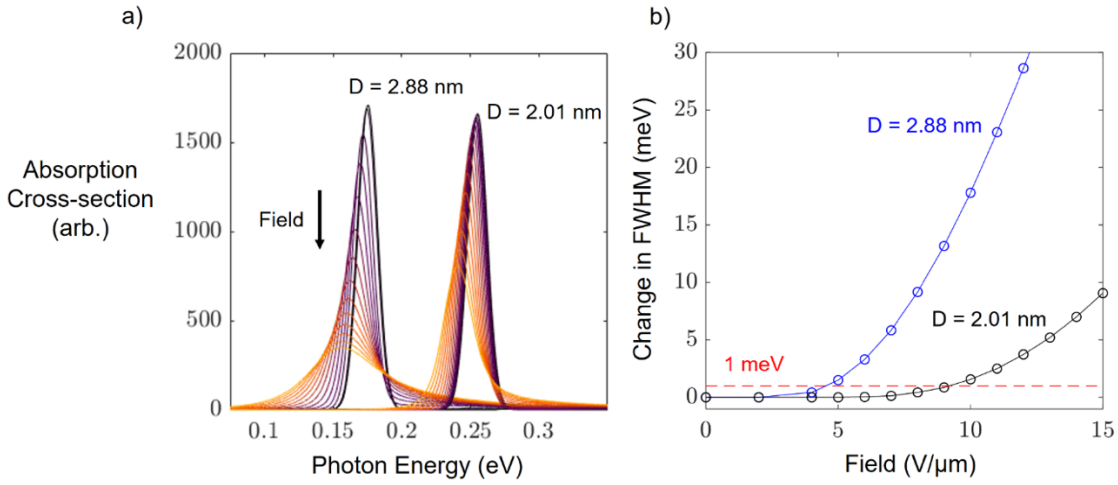

Figure 4.9 a) The calculated S11 absorption peak for CNT D and CNT E, the smallest and largest diameter CNTs in the study. The changing color indicated the field increasing from F = 0 V/μm (violet) to F = 15 V/μm (yellow). **b)** The change in FWHM for the S11 peaks shown in a).

Figure 4.9b shows the change in the FWHM of the S_{11} peak for the same CNTs as Figure 4.9a. The predicted linewidth at fields larger 5 V/μm suggests that the auto ionization broadening is at least 1 meV, which corresponds to lifetime of ~200 fs. No experimental comparison to S_{11} can be made as it lies outside the spectral range of the instruments, however the calculated peak shape gives information about the field induced exciton dissociation process. This is substantially lower than the estimated timescale of the non-radiative decay ($\tau_{non\text{-}rad}$) discussed throughout section 5. This theoretical result supports our assumption of fully ionized S_{11} excitons contributing to the photocurrent.

4.3 Simulation of optical interference from back reflection

The intensity light hitting the CNT is a key parameter required to determine the PCQY. Reflection of light from the substrate below the nanotube modulates the intensity. Commercial software can be used to simulate the interference pattern above the substrate where the nanotube is suspended.

A finite difference time domain (FDTD) simulation was used to determine the enhancement of optical power caused by back reflection from the split-gate electrodes. Inputs to the simulation included the device geometry, the dielectric functions of the device materials (platinum and silicon oxide) and the profile of the incident light beam. The beam profile was either a focused or defocused Gaussian beam profile coming from a numerical aperture that matches the microscope objective used in our experiment. The optical power is determined at a position corresponding to the center of the suspended carbon nanotube (CNT). The exact height of the nanotube could be 650 nm above the split gates (i.e. level with the top of the source and drain electrodes as shown in Figure 3.1a) or slightly less than 650 nm if the CNT adheres to the side wall of the source or drain electrode (Figure 4.10b). The best match between simulations and experiments was achieved when CNT height is assumed to be 617 nm above the split gates.

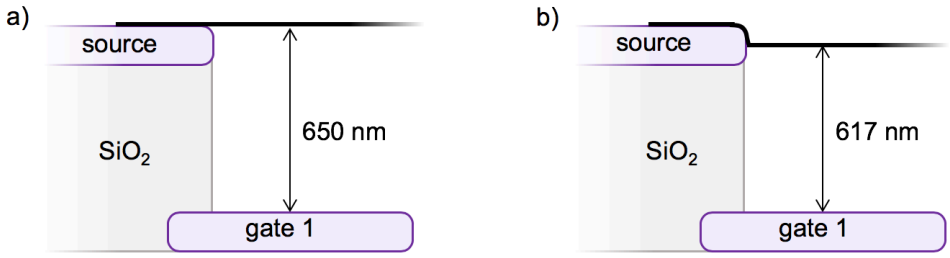

Figure 4.10 a) Cross sectional diagram of a CNT grown flat across the surface of the electrodes. **b)** Cross sectional diagram of a CNT that has adhered to the side of the electrode before crossing the trench

Figure 4.11a shows the boundary of the FDTD simulation as well as the Gaussian profile of a plane wave propagated through a 50X objective with a numerical aperture of 0.55. Figure 4.11b shows the interference strength β (the enhancement of the incident power due to back reflection) when the incident wavelength is 1630 nm. Figure 4.11c shows β at the center of the CNT when the incident light is either a focused beam and defocused beam. We also plot the ratio, β_{def}/β_{foc}, which we discuss in the next section. Due to uncertainty in the exact height of the CNT, there is uncertainty in β. Figure 4.11d shows the effect of changing the CNT height by ±17 nm.

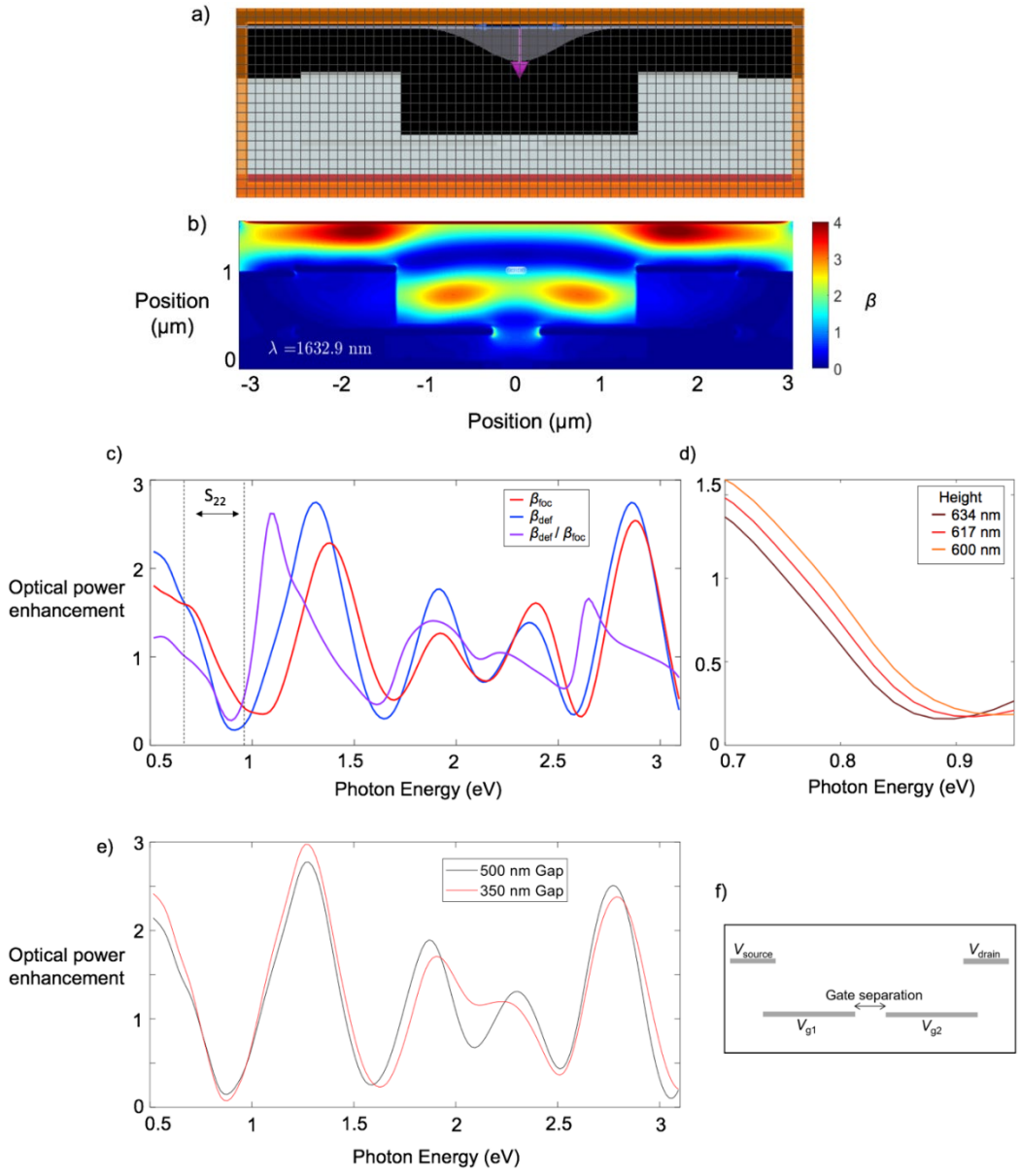

Figure 4.11 a) The FDTD simulation window with a focused Gaussian beam profile incident on the electrode geometry. **b)** The optical interference strength, β, at a wavelength of 1630 nm. **c)** Interference strength vs. photon energy measured at the center of the CNT, 616 nm above the top surface of the split gate electrodes. The range of S22 peak energies for the eight CNTs discussed in the main text is indicated. **d)** The interference strength vs. photon energy at different heights above the top surface of the split gate electrodes. **e)** The change in interference strength (defocused beam, height 616 nm) when the separation distance between the split-gates is reduced from 500 nm to 350 nm. **f)** Cross-sectional diagram of the electrode layout showing the separation between the gates.

The optical interference strength is affected by the separation distance between the split-gate electrodes (Figure 4.11e). The effect is most prominent when the wavelength is similar to the size of the gap. The nominal gap size (from the photolithography mask) is 500 nm, but SEM characterization shows that the gap can be as small as 350 nm. Figure 4.11e shows the effect of changing the gap from 500 nm to 350 nm. The spectrum is most affected in the range 1.5 – 2.5 eV. For measurements in the spectral range of the S_{22} resonance, the uncertainty in β due to the gap size is negligible.

Figure 4.12 shows a series of optical power enhancement simulations for a plane wave incident on different device structures. The panels below Figure 4.12a are illustrations of each interference simulation. The simplest simulation is a plane wave incident on a perfect conductor (black curve). The reflectivity decreases when the dielectric function of platinum in used in place of a perfect conductor (purple curve). The reflectivity decreases further and a phase shift is introduced when a layer of SiO_2 is added on top of the platinum (blue curve). The full simulation incorporates includes a gap in the middle of the electrodes (red curve).

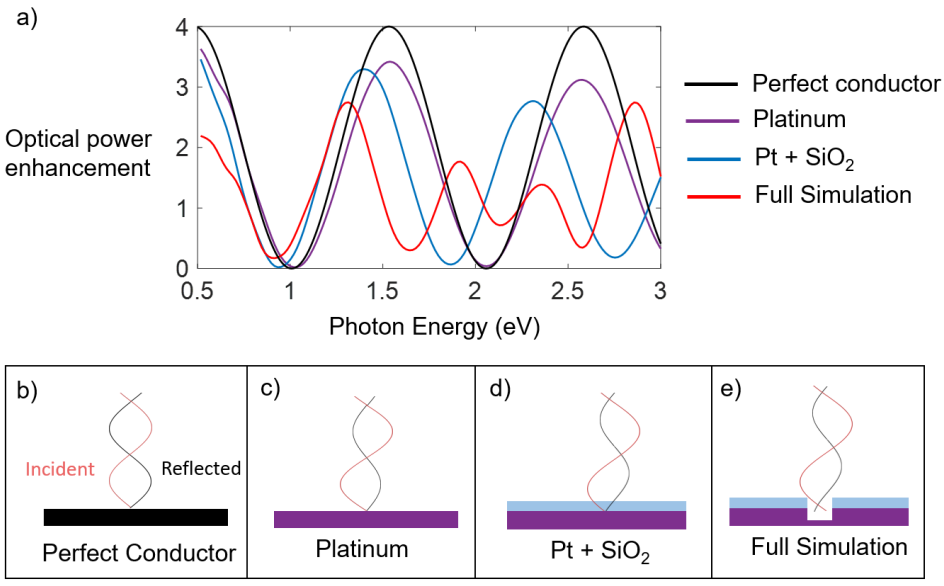

Figure 4.12 a) The change in optical power enhancement as different elements of the similuation are included. **b)** Illustration of a plane wave incident on a perfect conductor (corresponds to black curve) **c)** Illustration of a plane wave incident on a layer of platinum (corresponds to purple curve). **d)** Illustration of a plane wave incident on a layer SiO_2 on top of platinum (corresponds to blue curve). **e)** Illustration of a plane wave incident on layers of SiO_2 and platinum with a gap in middle (corresponds to red curve).

5 Field dependence of photocurrent quantum yield

The relationship between the photocurrent quantum yield (PCQY) and the electric field is the focus of Chapter 5. This chapter is adapted from our published work in Nano Letters.[83] Section 5.1 describes photocurrent measurements in CNT pn junctions, including the measurement of spatial photocurrent maps and photocurrent spectra. Section 5.2 explains how PCQY is determined as well as how each parameter involved is characterized. Section 5.3 discusses changes in photocurrent spectra with changing electric field field. Section 5.4 presents the main result of this thesis: the field dependence of the PCQY. Section 5.5 presents our interpretation of the PCQY field dependence in the context of computed theoretical contributions (explained in §4.2) from Dr. Vasili Perebeinos.

5.1 Photocurrent measurement of carbon nanotube photodiodes

In this thesis I use three measurement techniques to study photocurrent generation in CNT pn junctions. The first technique is scanning photocurrent imaging discussed in §5.1.1. The second technique, covered in §5.1.2, is measuring an illuminated I_{sd} vs V_{sd} curve (also referred to as an illuminated diode curve). The third technique is photocurrent spectroscopy described in §5.1.3.

5.1.1 Scanning Photocurrent Imaging

Photocurrent imaging is performed by focusing the laser near a CNT pn junction and raster scanning the surface. The photocurrent is recorded as a function of laser position. Figure 5.1 shows a photocurrent image of the CNT photodiode. The electrodes and axis of the carbon nanotube are indicated in the figure. Photocurrent is only generated in the intrinsic region at the center of the CNT which is smaller than the point spread function of the laser. This is evidenced by the lack of elongation of the photocurrent spot along the axis of the nanotube. Optical excitation of the p-doped and n-doped region does not lead to photocurrent because non-radiative decay processes cause rapid recombination of electron-hole pairs in the doped regions.[84,85]

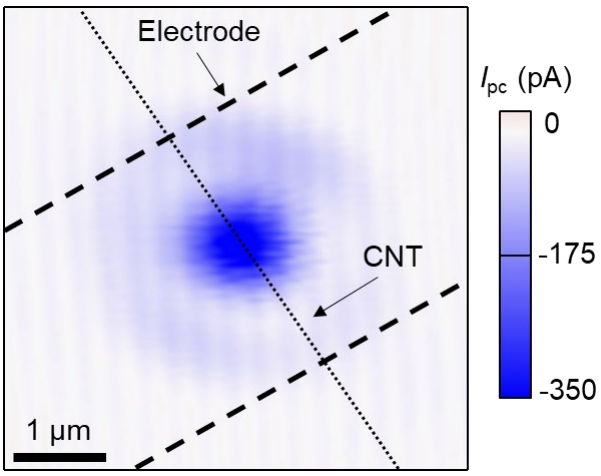

Figure 5.1 Scanning photocurrent image of a CNT photodiode. The location of the source-drain electrodes and the axis of the CNT are indicated.

Scanning photocurrent imaging can be used to measure the point spread function of the laser and determine the optical intensity in the incident laser (described in §5.2.2). The spatial photocurrent map can also be used to image the intrinsic region length. In Figure 5.1 the instrinic region length is smaller than the PSF of the laser spot so it cannot be resolved. However, under different gating conditions the intrinsic region length can be resolved. This process is described further in §5.2.3.

5.1.2 Illuminated diode curve

5.1.2.1 General features

Figure 5.2 shows the I_{sd} vs V_{sd} curve under illumination. In reverse bias, the photocurrent increases linearly with source-drain voltage. The change in photocurrent with V_{sd} corresponds to a change in the intrinsic region length. §4.1 describes the relationship between V_{g1}, V_{g2}, V_{sd}, and L_i in detail. Linear extrapolations of the curves are indicated with dashed lines in Figure 5.2. To understand the I_{sd} vs V_{sd} curve consider the simple model for intrinsic region length from §4.1.

$$L_i = \frac{|V_{sd} - E_g/e|}{F}. \tag{5.1}$$

The photocurrent is proportional to the intrinsic region length and quantum yield, η. The other quantities affecting the photocurrent are assumed to be constant with V_{sd} and $V_{g1} = -V_{g2}$. Therefore,

$$I_{\mathrm{pc}} \propto \eta \frac{\left|V_{\mathrm{sd}} - E_{\mathrm{g}}/e\right|}{F}. \tag{5.2}$$

where the bandgap, E_g, is the x-intercept. The bandgaps measured from experiments seem ~100 meV smaller than what is found from transport measurements. The source of the discrepancy isn't clear. The changes in slope can be understood as changes F η, which results in

$$\frac{dI_{\mathrm{pc}}}{dV_{\mathrm{sd}}} \propto \frac{\eta}{F}. \tag{5.3}$$

This relationship provides a way to calculate η from the slope of the illuminated diode curve if the field is known.

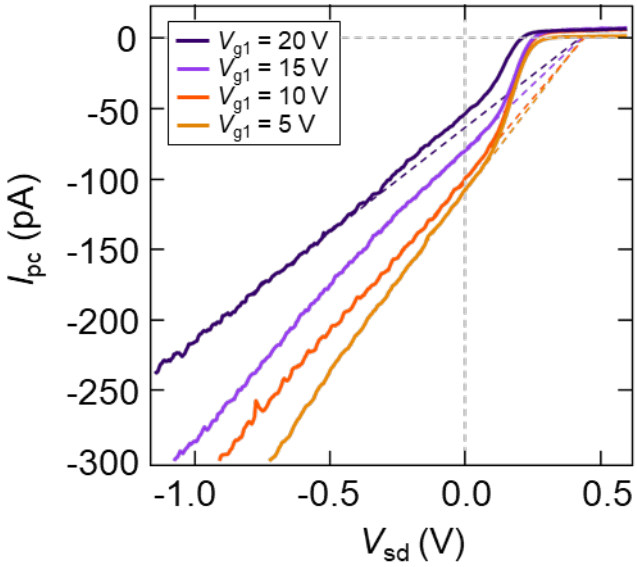

Figure 5.2 Experimental measurement of photocurrent for a (20,16) CNT excited at the S_{44} resonance ($\hbar\omega = 1.92$ eV). Photocurrent grows linearly with V_{sd} when for $V_{sd} < 0$. Linear extrapolations of these curves intercept the x-axis at the $V_{sd} = 0.4$ V, corresponding to the expected band gap of this CNT

5.1.2.2 Cross check for photo-conductance

The I_{sd} vs V_{sd} curve can be examined for evidence of a photoconduction mechanism. The photocurrent increases linearly in response to a bias voltage. Therefore, we expect to see a non-linear change in the reverse bias photocurrent if a photoconduction mechanism is present.

Figure 5.3 shows illuminated *IV* curves for two CNTs at the S_{22} resonance. As discussed in the main text, a linear increase in photocurrent is expected with increasing reverse bias as the intrinsic region of the CNT elongates. To first approximation, the photocurrent quantum yield

(PCQY) is independent of V_{sd}. Figure 5.3 shows lines of best fit (red dashed lines) based on Eqs. 4.9 and 5.4 with η_{22} = constant. Our procedure for extracting PCQY from the experimental data would give the same result for any V_{sd} between 0 and -0.5 V. It is worth noting in Figure 5.3 a and b that, despite nearly identical experimental conditions, we see different curvature beyond V_{sd} = -0.5 V which is not understood.

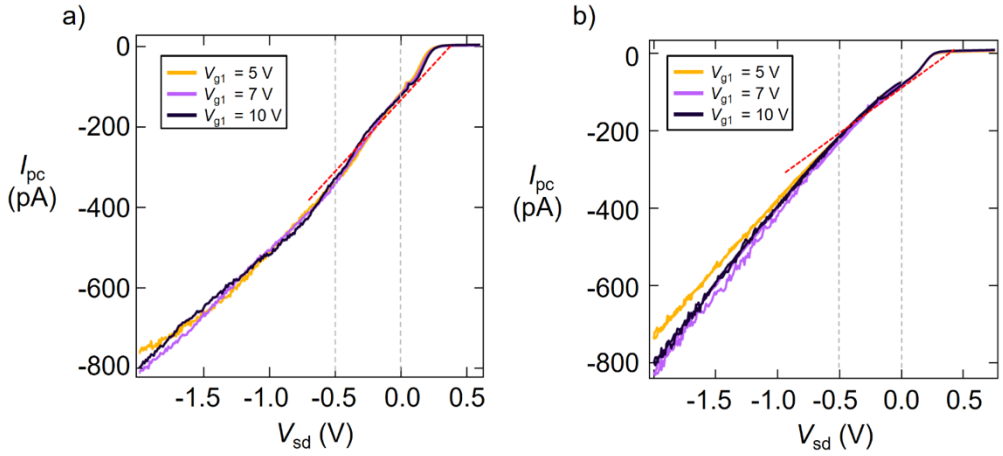

Figure 5.3 a) Illuminated IV curve of a (22,11) CNT excited at the resonance S_{22} = 0.86 eV. **b)** Illuminated IV curve of a (23,12) CNT excited at the resonance $_{S22}$ = 0.795 eV.

5.1.3 Carbon nanotube photocurrent spectroscopy

Photocurrent spectroscopy is a powerful tool that can be used to determine the precise structure of a CNT, and therefore, its absorption cross-section.[53,67,86] It is also useful for studying the response of excitons with different energies to the external field. A representative photocurrent spectrum is shown in Figure 5.4. The photocurrent is generated using a defocused laser spot with an intensity of approximately 10 W/cm^2. The optical intensity is sufficiently low that photocurrent is linear with respect to laser power (see Figure 5.6a). The light source is a supercontinuum laser with 320 MHz pulse rate (NKT Photonics). White light from the supercontinuum is filtered by a double monochromator to give monochromatic light with a 5 nm bandwidth.[87] For photocurrent spectra in this thesis, a reverse bias is applied to the photodiode of V_{sd} = -0.5 V unless otherwise stated. This bias is applied to elongate L_i and increased the photocurrent signal. The photocurrent and optical power can be monitored simultaneously to allow accurate power normalization (discussed further in §5.2). The spectral peaks are associated with excitonic resonances.[23] In Figure 5.4 observed peak positions (black) are compared to peak

position of the absorption cross section (blue), and are used to identify the chiral index.[88] The absorption cross section is found from an empirical model based on an atlas of CNT optical properties.[86]

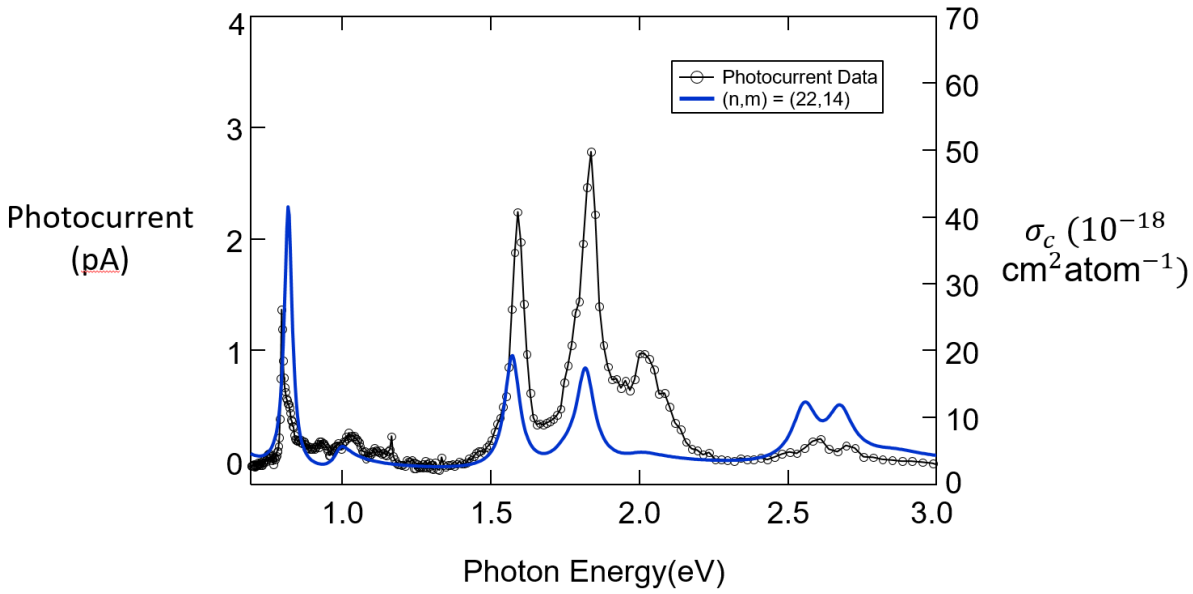

Figure 5.4 Photocurrent spectrum (black) around the S_{22}, S_{33}, S_{44}, S_{55}, and S_{66} exciton resonances. The spectrum was obtained with V_{sd} = -0.5 V and optical power ~ 10 μW spread over an area ~100 μm^2. The empirical absorption cross section of a CNT with chiral index (22,14) and diameter = 2.56 nm (blue).[67]

5.2 Calculation of photocurrent quantum yield

The photocurrent quantum yield (PCQY) is the ratio of electrons that get out of the device, measured as photocurrent, to the number of photons that are absorbed within the intrinsic region of the nanotube. Section 5.2.1 describes the process of extracting the PCQY from a photocurrent spectrum. Counting the number of electrons getting out of the device is as straightforward as measuring the current. The primary challenge of determining the PCQY lies in calculating the number of photons absorbed. Sections 5.2.2 and 5.2.3 discuss the two most important parameters used to find the number of photons absorbed: the photon flux and the intrinsic region length.

5.2.1 Extracting quantum yield from a photocurrent spectrum

The area underneath the photocurrent peak is proportional to the PCQY. To understand all of the factors contributing to peak area, consider the integral of the i^{th} photocurrent peak,

$$\int_{S_{ii}} I_{\mathrm{pc}}\, d(\hbar\omega) = e \cdot \eta_{ii} \cdot \Phi \cdot L_{\mathrm{i}} \cdot N_{\mathrm{L}} \int_{S_{ii}} \sigma_c\, d(\hbar\omega) \tag{5.4}$$

where e is the electron charge, η_{ii} is the PCQY at the i^{th} exciton resonance, Φ is the photon flux, L_{i} is the intrinsic region length, N_{L} is the number of atoms per length on the nanotube given by Eq. 4.13, σ_{c} is the absorption cross-section per carbon atom, and $\int \sigma_c d(\hbar\omega)$ is the oscillator strength per carbon atom. The product ($N_{\mathrm{L}} \cdot \int \sigma_c d(\hbar\omega)$) can be found from the chiral index of the CNT.[67]

Figure 5.5 illustrates how Eq. 5.4 is applied to $I_{\mathrm{pc}}(\hbar\omega)$ measurements to determine the PCQY. The CNT diameter is 2.51 nm and the photon energy is scanned over the S_{33} resonance ($\hbar\omega \approx 4E_{\mathrm{g}}$). The laser power (Figure 5.5b) is measured alongside the photocurrent. The power is corrected for interference from the substrate below the nanotube to accurately show the power incident on the nanotube (described in §4.3).

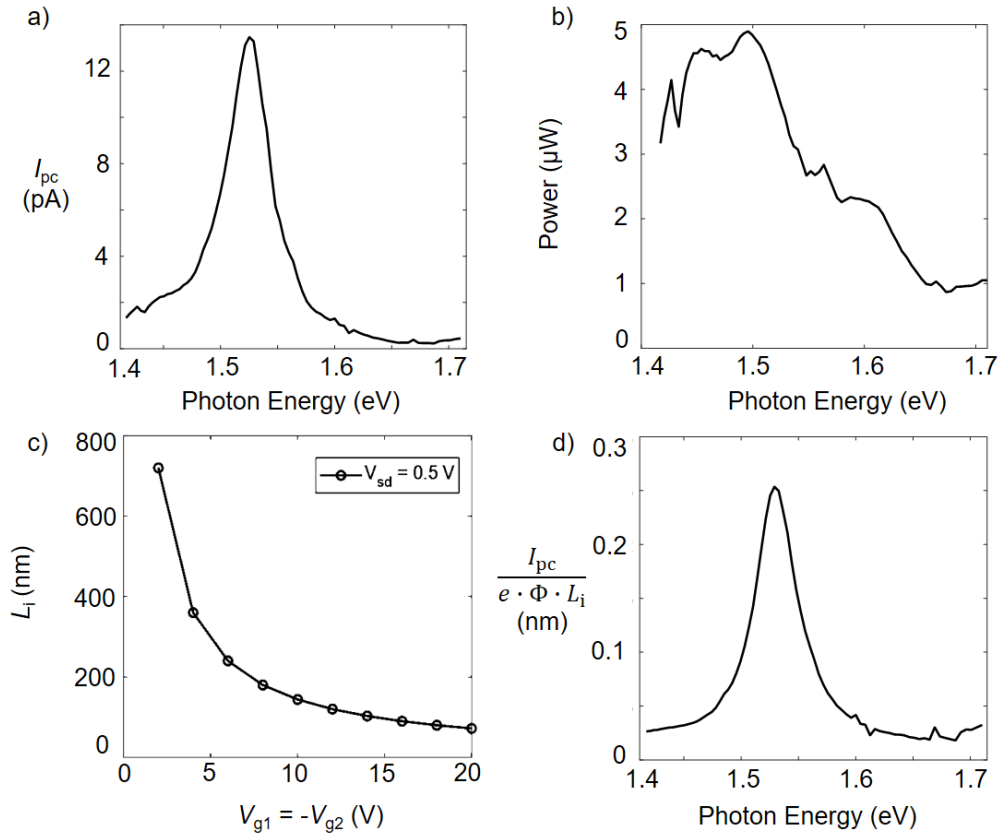

Figure 5.5 a) Photocurrent spectrum around the S_{33} exciton resonance of a CNT with chiral index (19,18) and diameter = 2.51 nm for V_{g1} = -V_{g2} = 4 V and V_{sd} = -0.5 V. **b)** The laser power at the height of the nanotube. **c)** The intrinsic region length calculated using the SCF simulations discussed in Section 4.1. **d)** The photocurrent peak corrected for photon flux and the intrinsic region length. Further analysis details in Appendix A for Device J.

First, the photocurrent spectrum was measured at V_{g1} = -V_{g2} = 4 V with a small reverse bias applied to the device of V_{sd} = -0.5 V (Figure 5.4a). Next, a combination of SCF simulations and photocurrent imaging were used to characterize L_i (Figure 5.5c). Section 4.1.3 describes how L_i is extracted from SCF simulations and Section 5.2.3 describes how values of L_i determined from photocurrent imaging are used to verify the electrostatics model. The photocurrent data was divided by $e \cdot \Phi \cdot L_i$ (Figure 5.5d). Section 5.2.2 describes in detail how Φ is characterized. Last, the photocurrent peak (shown in Figure 5.5d) is integrated and compared with the expected oscillator strength per unit length, $N_L \int_{S_{33}} \sigma_c \, d(\hbar\omega)$. The integration was performed by fitting the data with a Lorenztian. We use a Lorentzian fit to minimize the impact of the offset.

For this CNT chirality N_L = 307.1 atoms/nm and $\int_{S_{33}} \sigma_c \, d(\hbar\omega) = 1.63 \times 10^{-18}$eV cm^2 (further discussion of oscillator strength is provided in the §4.2.2). The PCQY is then given by

$$\eta_{33} = \int_{S_{33}} \frac{I_{\mathrm{pc}}(\hbar\omega)}{e \cdot \Phi \cdot L_{\mathrm{i}}} d(\hbar\omega) \Bigg/ \left(N_{\mathrm{L}} \int_{S_{33}} \sigma_c \, d(\hbar\omega) \right) = 0.35. \tag{5.5}$$

The field dependence of the PCQY for this device is discussed in §5.4.

5.2.2 Determination of photon flux

The photon flux can be calculated from the relationship

$$\Phi = \frac{P_0 \cdot \beta}{\hbar\omega \cdot A_{\mathrm{spot}}}, \tag{5.6}$$

where P_0 is the laser power, A_{spot} is the effective area of the laser point spread function (PSF), and β is the strength of interference from the substrate below the nanotube (discussed in §4.3). After determining β, the remaining challenge is to find A_{spot}.

The effective area of the PSF for the focused laser spot, $A_{\mathrm{spot,foc}}$, can be found from the scanning photocurrent image (Figure 5.6b). Because the intrinsic region of the CNT photodiode is much smaller than the laser spot, the photocurrent image samples the PSF. The spot area is found by integrating the PSF

$$A_{\mathrm{spot}} = \int PSF(x, y) \, dxdy \tag{5.7}$$

where $PSF(0,0) = 1$. The integral of Eq. 5.7 is calculated by fitting Gaussians to the experimental data. For the simplest PSF, A_{spot} can be calculated from a single Gaussian fit where

$$A_{\mathrm{spot}} = \int exp\left(\frac{-x^2}{a^2}\right) \cdot exp\left(\frac{-y^2}{b^2}\right) \mathrm{d}x\mathrm{d}y = \pi ab. \tag{5.8}$$

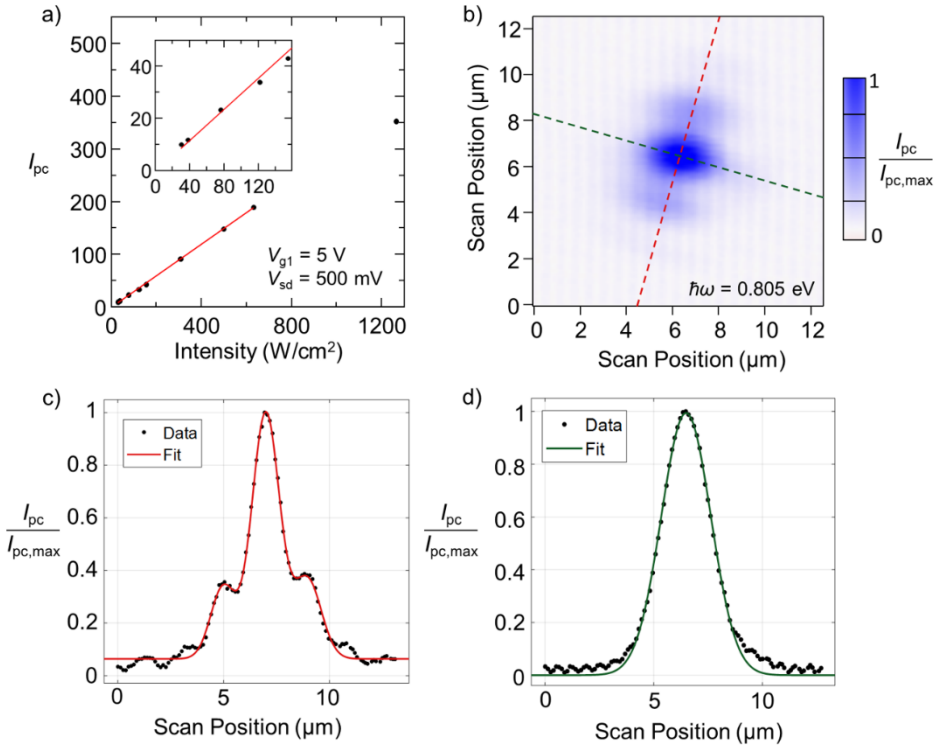

Figure 5.6 a) The typical photocurrent response as a function of laser intensity. The red linear fit has a slope of 0.3 pA cm^2 W^{-1}. **b)** A scanning photocurrent image sampling the PSF of the laser spot. **c)** Cross section of the photocurrent image in b) along the dashed red line along with a fit using the sum of three Gaussians (fit parameters in Appendix A: Device A summary) **d)** Cross section of the photocurrent image in b) along the dashed green line along with a Gaussian fit (fit parameters in Appendix A: Device A summary)

The photocurrent spot in Figure 5.6b has a more complicated PSF. To fit the PSF in Figure Figure 5.6b, we used a single Gaussian along one axis (Figure 5.6d) and three Gaussians along the other (Figure 5.6c). The spot area is then given by

$$A_{\text{spot}} = \int exp\left(\frac{-y^2}{w_y^2}\right) \cdot \left(a_{x,0} \cdot exp\left(\frac{-(x-x_0)^2}{w_{x,0}^2}\right) + a_{x,1} \cdot exp\left(\frac{-(x-x_1)^2}{w_{x,1}^2}\right) + a_{x,-1} \cdot exp\left(\frac{-(x-x_{-1})^2}{w_{x,-1}}\right)\right) \tag{5.9}$$

which results in

$$A_{\text{spot}} = \pi w_{y,0}\left(a_{x,0}w_{x,0} + a_{x,1}w_{x,1} + a_{x,-1}w_{x,-1}\right) \tag{5.10}$$

For the image in Figure 5.6b we found A_{spot} = 6.7 μm^2 (see Device A summary in Appendix A for the fit parameters).

The protocol for measuring a photocurrent spectrum used a defocused laser such that A_{spot} > 100 μm^2. This is done because, in the limit that $L_i << a$, the photon flux is constant across L_i. For these large spot areas, photocurrent imaging was not feasible and we used a different approach to find A_{spot}. We rely on the linear relationship between photocurrent and intensity (Figure 5.6a). The linear response of the photocurrent signal implies that the ratio of photocurrent to photon flux remains constant, which is given by

$$\frac{I_{pc,foc}}{\Phi_{foc}} = \frac{I_{pc,def}}{\Phi_{def}}, \tag{5.11}$$

where $I_{pc,foc}$ and $I_{pc,def}$ are the focused and defocused photocurrent respectively. Combining Eq. 5.6 and 5.11 we find that the area of the defocused spot can be calculated from

$$A_{spot,def} = \left(\frac{\beta_{def} \cdot P_{0,def}}{\beta_{foc} \cdot P_{0,foc}}\right) \cdot \left(\frac{I_{pc,foc}}{I_{pc,def}}\right) \cdot A_{spot,foc} \tag{5.12}$$

where P_{foc}/P_{def} is the ratio of laser powers for focused and defocused light, and β_{foc}/β_{def} is the ratio of enhancement factors for focused and defocused light.

5.2.3 Imaging the intrinsic region length

The length of the intrinsic region, L_i, can be measured in scanning photocurrent microscopy (SPCM) images when L_i is larger than the laser spot.[56] This section describes the process used to determine L_i from scanning photocurrentes images such as in Figure 5.1. These measured values of L_i are used to verify the electrostatics model (from §4.1) at particular values of V_{sd} and V_{g1} = - V_{g2}.

Figure 5.7 illustrates the process of extracting L_i from a pair of SPCM images. Both images were taken in an ambient environment at room temperature. The first image (Figure 5.7a) reveals the axis of the CNT. The image is acquired by setting V_{sd} = 0 and V_{g1} = - V_{g2} = 0. Positive current is generated at one end of the CNT by the electric field associated with the Schottky barrier contact. Negative current is generated at the other end of the CNT by the other Schottky barrier contact (electric field pointing in the reverse direction). The dashed lines in Figure 5.7a correspond to the edge of the metal electrodes. The electrode edges are determined from the reflection image (Figure 5.7c) which was acquired simultaneously. The second SPCM image

(Figure 5.7b) shows the photocurrent generated by the photodiode. A pn junction was established in the center of the CNT by setting V_{g1} = - V_{g2} = 6 V. The intrinsic region is elongated by applying a reverse bias V_{sd} = -3V. Figure 5.7d shows a cross-section of the photocurrent image, taken along the CNT axis.

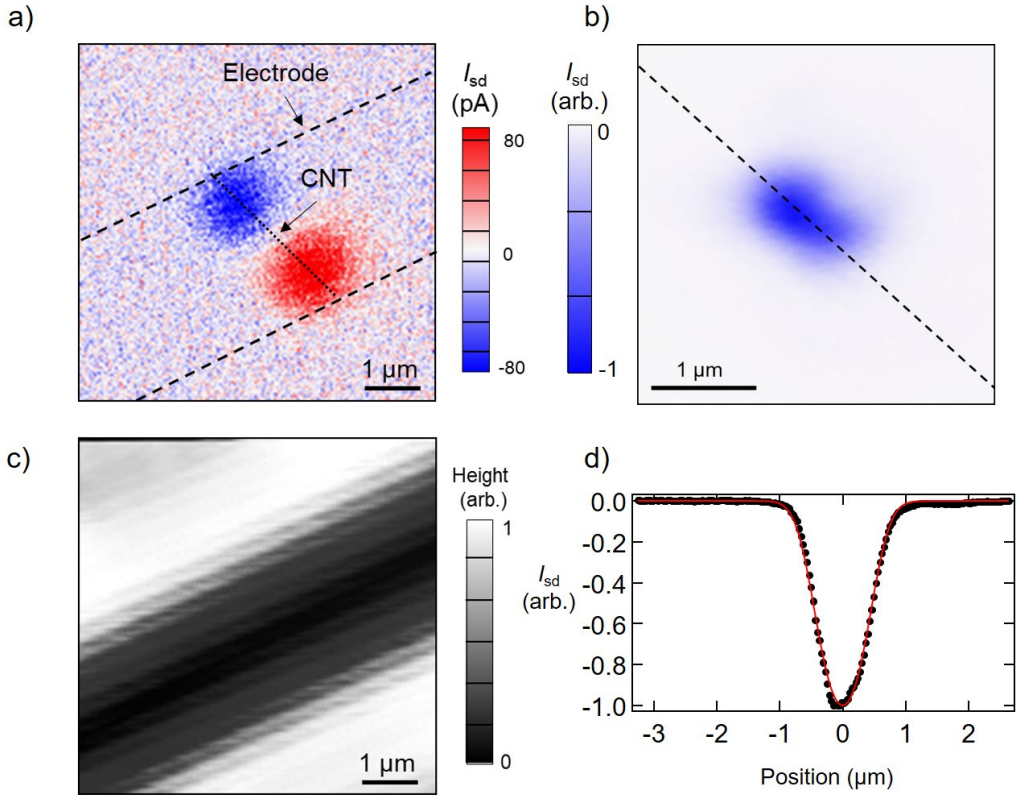

Figure 5.7 a) Scanning photocurrent image of the Schottky barriers at each contact with V_{sd} =0 and V_{g1} = V_{g2} = 0. The axis of the CNT is indicated with a dotted line. **b)** Scanning photocurrent image of an elongated photocurrent spot when V_{sd} = -3 V and V_{g1} = -V_{g2} = 6 V. **c)** An image of the reflected light from the scanning photocurrent image. The images shows the edges of the electrodes (white) the gate electrodes (grey) and the gap between the gate electrodes (black). **d)** A cross section of the photocurrent image shown in b) along the CNT axis. The fit from Eq. 5.15 is shown in red for L = 0.9 μm and a = 0.347 μm.

The photocurrent cross-section (shown in Figure 5.7d) is a convolution of the point spread function (PSF) of the laser spot and the position-dependent quantum yield, $\eta(x)$, of the CNT. Along the axis of the CNT (the x direction), the PSF of the laser spot is treated as a Gaussian given by

$$f(x) = \exp\left(-\frac{x^2}{a^2}\right). \tag{5.13}$$

We estimate $\eta(x)$ as a top-hat function

$$\eta(x) = \begin{cases} 0 & \text{when } x < -L_\mathrm{i}/2 \\ \eta_0 & \text{when } -L_\mathrm{i}/2 < x < L_\mathrm{i}/2. \\ 0 & \text{when } x > L_\mathrm{i}/2 \end{cases} \tag{5.14}$$

The expected photocurrent profile along the axis of the CNT, $I_\mathrm{sd}(x)$, is then a convolution of $f(x)$ and $\eta(x)$

$$I_\mathrm{sd}(x) \propto \mathrm{erf}\left(\frac{x - \frac{L_\mathrm{i}}{2}}{a}\right) - \mathrm{erf}\left(\frac{x + \frac{L_\mathrm{i}}{2}}{a}\right). \tag{5.15}$$

To determine intrinsic region length from Figure 5.7d, we fit Eq.5.15, using L_i and peak current as fitting parameters. We note that Eq. 5.15 becomes indistinguishable from a Gaussian when $L_\mathrm{i} < a$, therefore, fitted values of L_i are only reliable for $L_\mathrm{i} \gtrsim 2a$.

For PCQY calculations from a photocurrent spectrum (as is done in §5.2.1), the laser is defocused. For the defocused laser, $L_\mathrm{i} \ll a$. In this regime, the intensity doesn't change appreciably across the intrinsic region, and it is more straightforward to calculate the PCQY as $I_\mathrm{sd}(x) \propto L_\mathrm{i}$.

Figure 5.8a and c show the cross-sections of photocurrent images of pn junctions corresponding to various V_g1 = -V_g2 and V_sd. Figure S11a shows the decrease in L_i as V_g1 = V_g2 increases. Figure 5.8c shows the increase in L_i as $|V_\mathrm{sd}|$ increases. In both Figures, we not that the width of the peak stops changing when $L_\mathrm{i} \lesssim 2a$, due to the spatial resolution of our microscope. Figure 5.8d compares the fitted value of L_i with the model described in §4.1.3 (Eq.4.9). We see excellent agreement between experiment and modeling when L_i > 600 nm, giving us confidence in the electrostatics modeling.

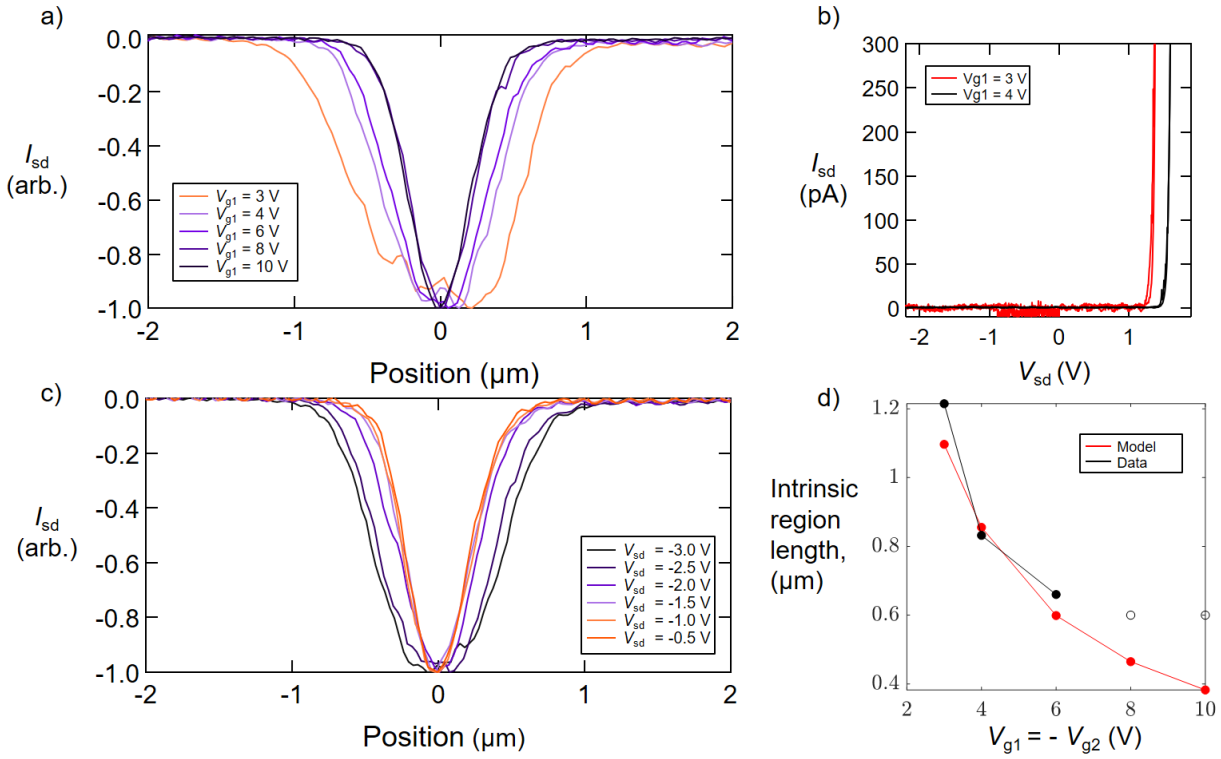

Figure 5.8 a) Cross sections of photocurrent images along the CNT axis for various $V_{g1} = -V_{g2}$. $V_{sd} = -2$ V for all 5 curves. **b)** Diode characteristics at the highest ratios of V_{sd}/V_{g1} used in (a). There is no reverse-bias break down. **c)** Cross sections of photocurrent images along the CNT axis at various V_{sd}. $V_{g1} = -V_{g2} = 6$ V for all 6 curves. **d)** Comparison of the model in Eq. 2 of the main text (red) with experimental measurement of L_i extracted from the cross sections shown in (a) (black). The fitting procedure to find L_i becomes unreliable when $V_{g1} > 6$ V (open circles), because L_i is below the spatial resolution of the microscope. The nanotube chirality is (17,12).

Examples of the images used to make the cross-sections are shown in Figure 5.9, where the elongation of the instrinsic region can be seen when $|V_{sd}|$ increases (the change from panel b to a) and when $V_{g1} = -V_{g2}$ decreases (the change from panel b to c).

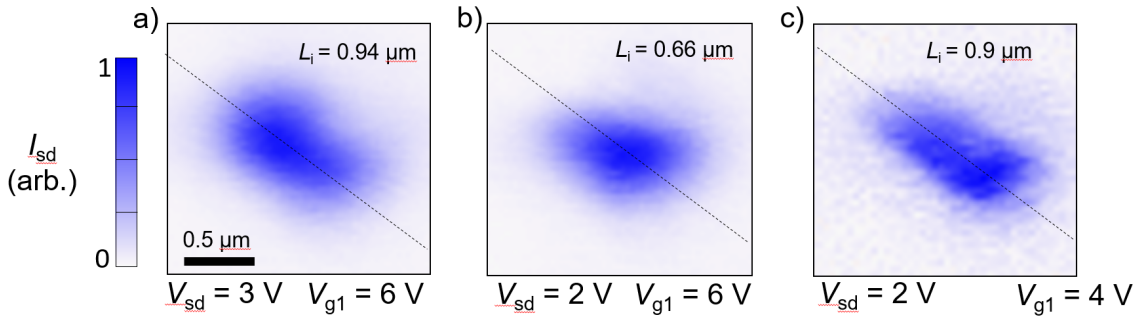

Figure 5.9 Scanning photocurrent images showing elongation of the intrinsic region when $|V_{sd}|$ increases or $V_{g1} = -V_{g2}$ decreases. The scale bar is 0.5 µm. Dashed lines indicate the CNT axis.

5.2.4 Effect of angle on axial field

The angle that the CNT grows across the trench changes the electric field experienced by the gates. Figure 5.10 shows a nanotube that has grown at a fairly large angle relative to the . A first order estimate of the axial field in CNT is that it's simply the component parallel to the axis of the CNT. Therefore

$$F_{\parallel} = \mathrm{F}_0 \cos\theta \tag{5.16}$$

where F_0 is the magnitude of the electric field, $F_{\parallel}$ is the axial component, and θ is the angle shown in Figure 5.10.

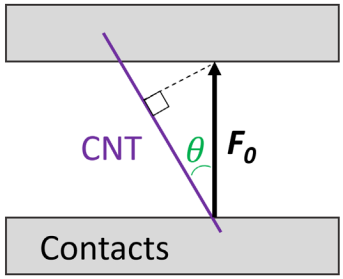

Figure 5.10 Depection of a carbon nanotube grown across two electrodes at an angle θ relative to the electric field, F_0.

The angle between the nanotube and contacts can be determined from scanning photocurrent images. Figure 5.7a shows how the angle can be determined from scanning photocurrent imaging. Table 5.1 shows the values of θ for CNTs used in the study. The results shown in Figure 5.15 are not corrected for the angle. The values can be corrected by multiply both the field and the PCQY by $\cos\theta$ from the angles listed in Table 5.1.

CNT	A	B	C	D	E	F	G	H	J	K
θ	21°	NA	NA	13°	NA	NA	47°	22°	16°	23°

Table 5.1 The angles of the nanotubes relative to the electrodes for the CNTs used in the study. The angle could not be determined for some CNTs, indicated as NA.

5.3 Photocurrent spectra in changing axial electric field

Now that we have established a method to find PCQY from a photocurrent spectrum (§5.2) as well as a method to determine the axial electric field (§4.1) we have the tools to determine the field dependence of the photocurrent quantum yield. Figure 5.11 shows a representative set of photocurrent spectra at increasing axial field. The peak position, peak height, and peak width all change in response to field. Section 5.3.1 discusses the change in peak position. Section 5.3.2 discusses the change in width.

Since we are interested in quantifying PCQY as we increase the split-gate voltages (i.e. strengthen the axial electric field in the center of the CNT), the area of each photocurrent peak in Figure 5.11 is integrated. The S_{22} photocurrent peak area increases by a factor of 6.5. In contrast, the S_{33} and S_{44} peak areas decrease by a factor of 2.2 and 1.4 respectively. The dramatic increase in peak area for S_{22} motivated a detailed study of the field dependence of the PCQY excited at the S_{22} resonance (discussed in §5.4).

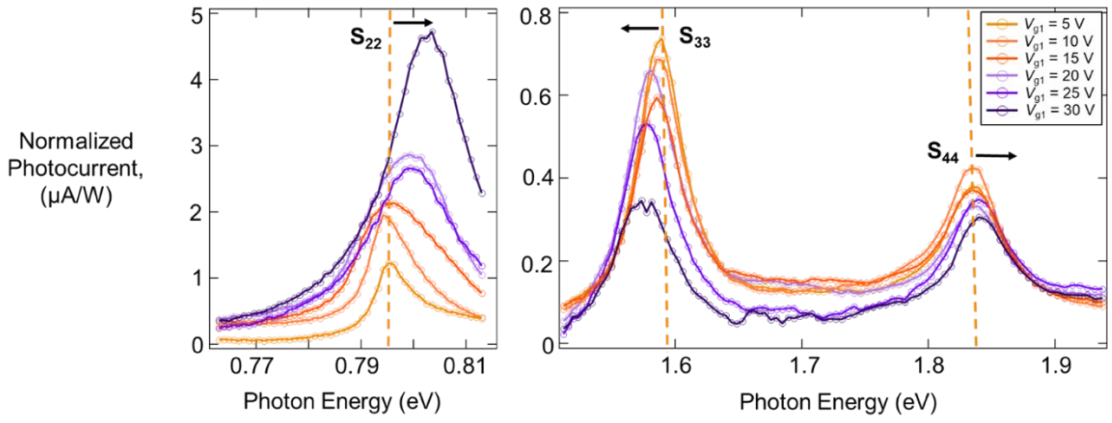

Figure 5.11 Power normalized photocurrent spectrum around the S_{22}, S_{33}, and S_{44} exciton resonances of a CNT with chiral index (22,14) and diameter = 2.46 nm. The spectrum was obtained with V_{sd} = -0.5 V and optical power ~ 10 μW spread over an area ~100 μm^2 (see Device G summary in Appendix A for more details).

5.3.1 Peak shifting

We propose that the observed spectral shifts of exciton resonances are caused by two independent mechanisms. The first mechanism is the axial strain that is generated by the electrostatic force pulling down on the CNT. The second mechanism is the Stark shift.

The magnitudes of the shifts are higher than expected from the Stark effect (see §4.2.1). Shifts of alternating sign are consistent with axial strain from the electrostatic force pulling the CNT towards the gates. Comparing the measured peak shifts to previous studies of strained CNTs,[89,90] we estimate that axial strain reaches ~ 0.2%. Theory work has studied an interaction-driven diameter dependence of strain on the CNT absorption spectrum.[91] This voltage-controlled tuning of optical resonances is an interesting effect, and potentially useful for CNT-based quantum-light sources.[92] However, the effect is not central to the main focus of this thesis so it discussed briefly.

We have studied the S_{22} resonance of 8 different CNTs. The CNT diameters range from 2.0 to 2.9 nm (the S_{22} energies range from 1.05 to 0.72 eV). As the split gate voltage is increased, we track the spectral position of the S_{22} peak. The peaks shift upward or downward in energy depending on the interplay between axial strain and CNT band structure.[90] We independently verified the CNT "family index" by performing chiral index assignment. Six CNTs are from the family $(n - m) \bmod 3 = 1$, and two CNTs are from the family $(n - m) \bmod 3 = 2$ (see Figure 5.12a). The family index correctly predicts the direction of the peak shift.

Given a large sample of CNTs, the average spectral shift caused by axial strain should be zero. CNTs with $(n - m) \bmod 3 = 1$ will exhibit strain-induced redshift, while an equal number of CNTs with $(n - m) \bmod 3 = 2$ will exhibit strain-induced blueshift. Using our experimental data (Fig. 4a of main text) we calculated the average spectral shift of all eight CNTs. The $(n - m) \bmod 3 = 2$ family of CNT was weighted more heavily, because only 2 out 8 CNTs were from this family. The weighted average (Figure 5.12b) shows a clear trend toward redshift. We expect that strain should only cause a redshift, therefore we compared the average redshift to the average shift expected from strain.

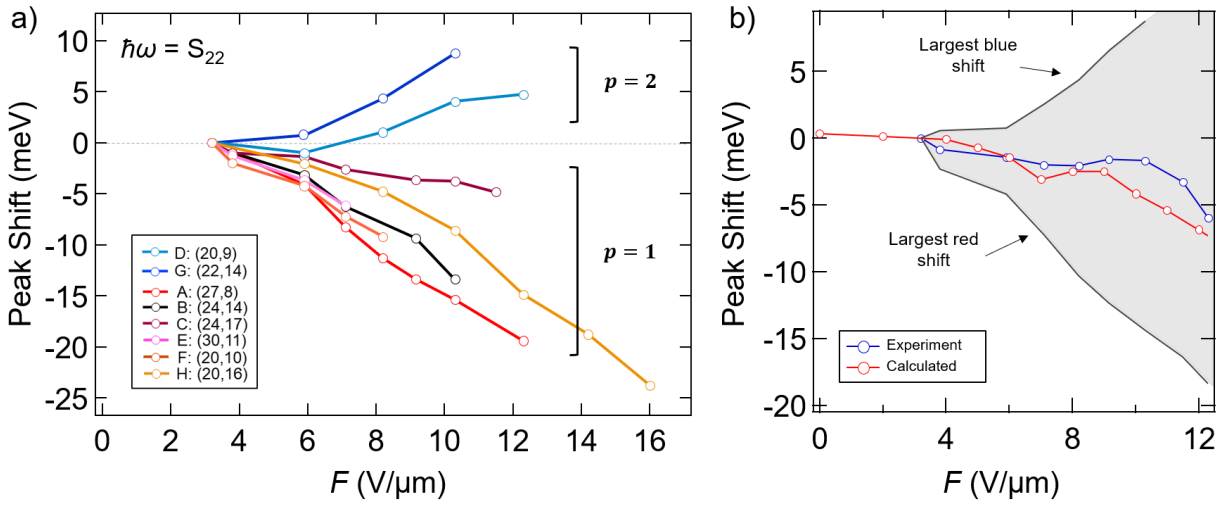

Figure 5.12 a) S_{22} peak position as a function of axial electric field for eight different CNTs with known chirality. **b)** The blue curve shows the weighted average of the S_{22} peak shift for the eight CNTs discussed in the main text. The red curve shows the calculated average Stark shift of the S_{22} resonance for the same eight CNTs. The grey boundaries show the spread of peak shifts observed in the experiment.

There is good agreement between theory and the observed average shift. This agreement supports our proposed interpretation that strain causes most of the observed peak shift, but the Stark effect causes a small but noticeable shift towards lower energies.

5.3.2 Peak width

From computational modeling (§4.2.3), we expect the width of the exciton peak to change with F (Figure 5.13d). Figure 5.13a shows the FWHM of the S_{22} photocurrent peak for the same eight CNTs discussed in the previous section. For some CNTs in the study, the FWHM changes as a function of the axial field (summaries of the data for each device are presented in Appendix A).

The data and theory both show non-monotonic changes in FWHM, however the step size for F in the experiment may be too large to resolve the sharp features present in the calculation. The largest experimentally observed change in FWHM at high field (~10 V/μm, shown in Figure 5.13c) is on the order of 10 meV which agrees with the calculation (Figure 5.13d).

The FWHM of the S_{22} photocurrent peak (at low F) is plotted as a function the peak energy in Figure 5.13b. Based on previous work we expect a linear relationship between the FWHM

(Γ_p) and the transition energy (E_{peak}).[67,93] Liu et al. found $\Gamma_p = 0.0388 \cdot E_{peak}$. We find that our measured FWHM values also follow a linear trend, but with overall smaller values of

$$\Gamma_p = 0.02 \cdot E_{peak} \tag{5.17}$$

as shown by the dashed line in Figure 5.13b.

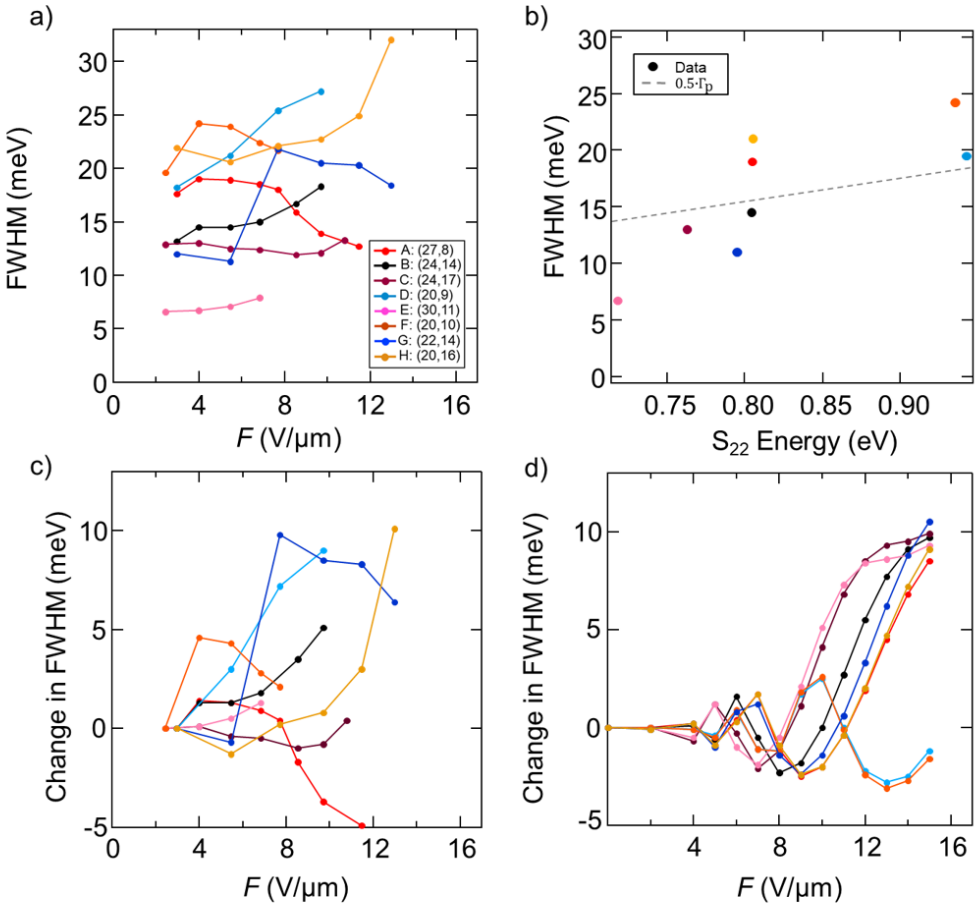

Figure 5.13 a) The FWHM of the S_{22} photocurrent peaks at increasing axial field for the eight different chiralities discussed in the main text. **b)** The FWHM of the S_{22} photocurrent peak with an applied axial field of 4 V/μm. The dashed line is the relationship in Eq. S9. **c)** The change in FWHM of the S_{22} photocurrent peaks. **d)** Calculated changes in the FWHM of the S_{22} absorption peak as a function of field for each chirality of CNT in the study. The color coding in the inset of panel (a) applies to all of the panels.

5.4 Photocurrent quantum yield as a function of axial electric field

This section presents the field dependence of the PCQY, which is the main result of this thesis. Figure 5.14 shows the PCQY extracted from a CNT at the S_{33} resonance using the process

described in §5.2. The PCQY at low field ($\eta_{33} \approx 35\%$) is similar to previously reported PCQY at S_{44} and S_{55} exciton resonances.[56] As the field increases from 2.4 V/μm to 8.5 V/μm, however, η_{33} increases by more than a factor of 3 and begins to exceed 100% PCQY. The upward trend in $\eta_{33}(F)$ suggests that even higher values of η_{33} would be possible if our device could sustain larger split gate voltages. This result suggests that room temperature carrier multiplication can be achieved when $\hbar\omega \approx 4E_g$.

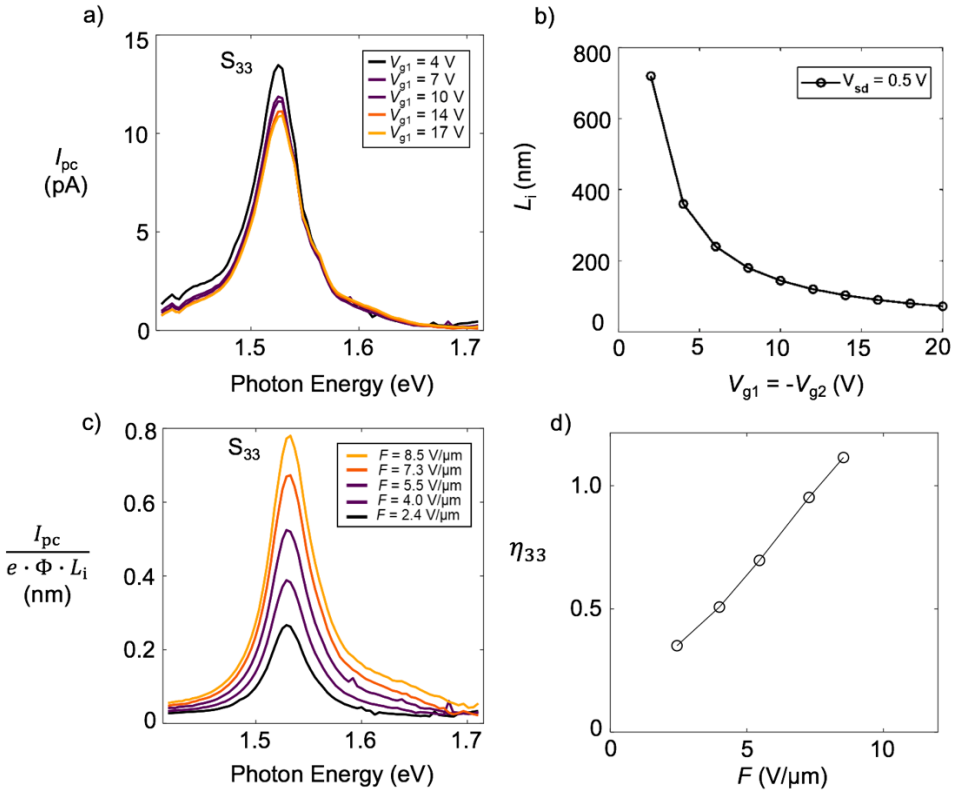

Figure 5.14 a) The photocurrent spectrum at increasing gate voltage centered on the S_{33} exciton resonance of a (19,18) CNT with a diameter of 2.51 nm. **b)** The intrinsic region length at increasing gate voltage**. c)** The photocurrent spectrum normalized by the photon flux and intrinsic region length. **d)** The photocurrent quantum yield of the device versus increasing axial field.

For efficient light-harvesting applications, the most intriguing possibility is carrier multiplication when $\hbar\omega \approx 2E_g$. Therefore, I now want to focus on measurement of $\eta_{22}(F)$. We have studied the S_{22} resonance of 8 different CNTs. The CNT diameters range from 2.0 to 2.9 nm (the S_{22} energies range from 1.05 to 0.72 eV).

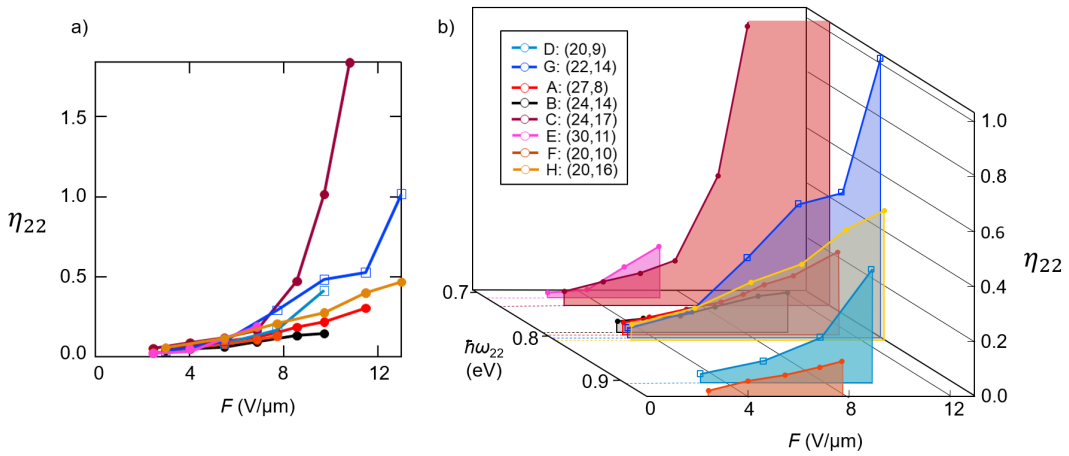

Figure 5.15. **a)** The photocurrent quantum yield at the S_{22} exciton resonance for 8 different CNTs as a function of increasing axial electric field. V_{sd} = -0.5 V. Squares indicate insufficient data to determine photon flux. **b)** The PCQY as a function of field for the same 8 CNTs plotted on a third axis against the S_{22} resonance energy.

For each CNT, we measured $I_{pc}(\hbar\omega)$ and divided the spectra by $e \cdot \Phi \cdot L_i$ (see Appendix A: Device A-J Summaries). The integrated spectral peaks were then compared with the expected oscillator strength per unit length, $N_L \int_{S_{22}} \sigma_c \, d(\hbar\omega)$. The resulting values of η_{22} are plotted in Fig. 4b. The $\eta_{22}(F)$ curves have been sorted by $\hbar\omega_{22}$ (the photon energy corresponding to S_{22} at low F). When interpreting Figure 5.15, the $\hbar\omega_{22}$ axis can be used as proxy for CNT diameter ($\hbar\omega_{22} \propto 1/D$) or exciton binding energy ($\hbar\omega_{22} \propto E_b$). We find the largest values of η_{22} when $\hbar\omega_{22}$ is small.

At low F, $\eta_{22} = 0.03$ - 0.05, in agreement with previous measurements of η_{22} . In the smallest diameter CNTs (large $\hbar\omega_{22}$), we find that η_{22} increases modestly with F. In the larger diameter CNTs (smaller $\hbar\omega_{22}$), however, we find that η_{22} increases as much as 35-fold. One device exhibits η_{22} = 1.7 (see Figure 5.15b and Figure 8.5). All curves get steeper at high field suggesting that η_{22} would increase further if our devices could sustain higher split-gate voltages.

The calibration process to quantify PCQY has multiple steps and we have attempted to crosscheck the process as much as possible. First, we note that low-field PCQY agrees with previous work.[54] [56] Second, when photocurrent spectra are normalized by β, the resonance line shapes match the expected Lorentzian line shape. Third, our model for L_i was verified by photocurrent imaging and by measuring I_{pc} vs. V_{sd} (Figure 5.8d & Figure 5.9). Fourth, we

crosschecked the calculated values of F by comparing the average spectral shift to the expected Stark shift of S_{22} resonances (§4.2.1). Overall, we estimate that our calibration process yields PCQY values with ~±30% uncertainty. An additional source of uncertainty, which we cannot mitigate with our experimental design, is uncertainty in the integrated absorption cross-section $\int_{S_{ii}} \sigma_c \, d(\hbar\omega)$. Liu et al. measured $\int_{S_{ii}} \sigma_c \, d(\hbar\omega)$ for more than 50 individual suspended CNTs.[67] Their measured values were distributed above/below the line of best fit by ~ ±30%. We used Liu's line of best fit for our analysis, thus the overall uncertainty in our PCQY determination is ~ ±40%. We note there is significantly less uncertainty associated with our measurements of the *relative* change in PCQY as a function of F for a particular CNT.

5.5 Exciton dissociation pathways and timescales

The measurements of PCQY are interpreted by considering the relaxation pathways of S_{22} and S_{33} excitons, and the expected field-dependence of these pathways (Figure 5.16). First, consider the relaxation of the S_{22} excitons when F is too small to induce exciton dissociation. In this low-field regime, η_{22} increases almost linearly with F (Figure 5.15). Kumamoto et al. studied this regime in detail and proposed that free carriers are produced by spontaneous dissociation of S_{22} excitons (Figure 5.16a). These free carriers are then converted to photocurrent if the electric field sweeps out the free carriers faster than they form bound states.[58] To verify that Kumamoto's model is applicable to our system Vasili calculated the decay products for spontaneous dissociation of S_{22} excitons in an experimentally relevant CNT (Figure 5.16b). Spontaneous dissociation occurs via either an electronic pathway or a phonon-mediated pathway, with a branching ratio ~ 1:10 (the phonon pathway is about 10 times more probable).[93] The electronic pathway produces only free e-h pairs ($e_1 + h_1$).[93,94] The phonon-mediated pathway produces a variety of products: free e-h pairs ($e_1 + h_1$, $e_2 + h_1$, $e_1 + h_2$), bound, and partially bound excitons.[93,94] We solved the Bethe-Salpeter equation for the phonon decay mechanism.[93,94] Our calculations for the experimentally relevant (20,9) CNT show that most of the products of the phonon-mediated S_{22} decay pathway have electron-hole separation greater than the bound S_{11} or S_{12} exciton radiuses i.e. >> 2 nm (Figure 5.16b).

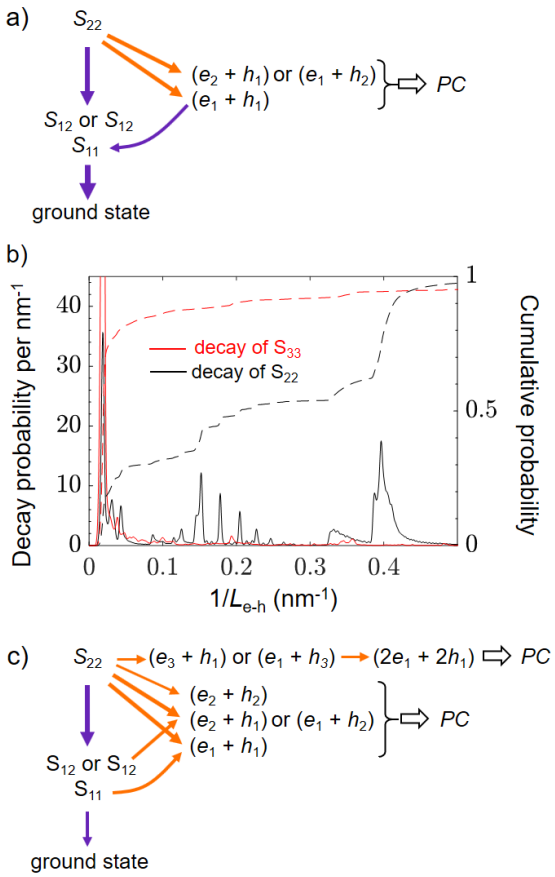

Figure 5.16 a) Proposed pathways for relaxation of the S_{22} exciton at low field (no field-induced exciton dissociation). Pathways that can lead to photocurrent (PC) are shown in orange. White arrows represent free carriers that are swept out by electric field. **b)** Computational modeling of a (20, 9) CNT. The model calculates the size distribution of the e-h separation of the decay products of the S_{22} and S_{33} phonon decay mechanism. The x-axis is the inverse size of the e-h separation using a two-particle wavefunction from the Bethe-Salpeter Equation solution. Solid lines represent the probability of generating the decay product with a certain e-h separation, and dashed lines represent the cumulative probability. The leftmost peaks in probability correspond to free carriers (Le-h = 50 nm = one quarter of the length of the simulated supercell). The rightmost peak for S_{22} decay (about 40% of the total decay products) corresponds to fully bound S_{11} and S_{12} excitons (Le-h ≈ 2.5 nm). **c)** Possible relaxation pathways of the S_{22} exciton at high field, including field-induced dissociation of S_{11}, S_{12}, S_{21} and S_{22} excitons

If S_{22} decay products are not swept out of the intrinsic region, they will likely reach the S_{11} exciton state. At low field, the S_{11} exciton can undergo either radiative recombination (τ_{rad} ~ 10 ns [84,95,96]) or non-radiative recombination. To estimate the non-radiative recombination time in our system, $\tau_{non\text{-}rad}$, excitons are assumed to diffuse to the ends of the intrinsic region where end

quenching occurs.[85,97] The typical length of the intrinsic region is $L_i \approx 100$ nm, and the exciton diffusion constant is approximately 10 cm^2/s,[98] therefore, $\tau_{non\text{-}rad} \approx 10$ ps.

When F is sufficiently large, field-induced exciton dissociation may occur. There is previous experimental evidence that S_{11} excitons can be dissociated by large electric fields. In that previous work, electric field was applied perpendicular to the CNT axis.[99] In contrast, our experiment uses axial electric field and carriers are kept inside the CNT. A theoretical description of our system (at the perturbation level) predicts that the S_{11} dissociation time is given by[59]

$$\tau_{\text{diss}} = \frac{\hbar F}{4E_b F_0} \cdot \exp\left(\frac{F_0}{F}\right) \tag{5.18}$$

where E_b is the exciton binding energy and F_0 is a characteristic field which scales with E_b. For our CNT diameters, E_b ranges from approximately 130 to 160 meV,[100] and F_0 ranges from approximately 60 to 80 V/μm.[59] S_{11} dissociation becomes significant when τ_{diss} is short compared to $\tau_{non\text{-}rad}$. Eq. 5.18 predicts that $\tau_{diss} < \tau_{non\text{-}rad}$ when F exceeds 5 to 10 V/μm (the field threshold depends on E_b). The predictions of Eq. 5.18 are verified by solving the Bethe-Salpeter equation for an exciton in the presence of a static axial electric field (§4.2). Both theoretical approaches are consistent with our experimental observation that η_{22} grows dramatically for larger diameter CNTs when F exceeds ~ 8 V/μm (Figure 5.15). We conclude that field-assisted dissociation of S_{11} can explain much of the observed increase in η_{22}. However, field-assisted dissociation is not sufficient to explain $\eta_{22} > 1$.

Our observation that η_{22} may exceed 100% suggests that carrier multiplication can occur at room-temperature in large-diameter suspended CNTs ($\gtrsim$ 2.6 nm) when F is sufficiently large ($\gtrsim$ 10 V/μm). Previous authors have hypothesized that such carrier multiplication can be expected from impact ionization.[50,60] However, it is difficult to reconcile momentum conservation with impact ionization in the second subband of semiconducting CNTs.[47] Our measurements, together with previous evidence,[50] suggest that impact ionization models may have to incorporate phonons (or additional carriers) to describe experiments. The details of S_{22} decay in the presence of strong electric field has been the subject of additional theoretical work,[60] and remains an open question. Some possible pathways are illustrated in Figure 5.16c.

Photocurrent quantum yield from the S_{33} exciton (Figure 5.14d) exhibits a different field dependence than PCQY from S_{22}. At low field, η_{33} is significantly higher than η_{22} (~ 30% compared to 5%) which may be explained by the spontaneous decay products of S_{33}. Figure 5.16b shows that almost 100% of the products from the phonon-mediated S_{33} decay pathway are free carriers. The electronic pathway for spontaneous dissociation of S_{33} also generates only free carriers.[94] Therefore, it's expected that $\eta_{33} > \eta_{22}$ at low field, and as F is increased, η_{33} is expected to grow and remain larger than η_{22}.

In conclusion, when photons of energy ~ $2E_g$ are absorbed in the intrinsic region of a CNT photodiode, our data suggest it is possible to extract a photocurrent that corresponds to more than one electron per photon. This high-efficiency process is observed by increasing CNT diameter to $\gtrsim$ 2.6 nm, and increasing the axial electric field to $\gtrsim$ 10 V/μm (a regime of diameter and field that have not been studied previously). Higher energy optical excitation (for example S_{33} resonant excitation) gives even higher PCQY. The observed diameter dependence of PCQY is consistent with the diameter dependence of exciton binding energy (large diameter CNTs have lower exciton binding energy). Interestingly, increasing diameter is also expected to reduce the rate of impact ionization,[47] however, our experiments suggest there are CNT diameters for which rapid impact ionization can co-exist with exciton dissociation. Possible directions for future work include the use of dielectric environment to tune the strength of the Coulomb interaction in the CNT,[63] so that high-efficiency photocurrent generation could be achieved at lower electric field.

6 Conclusion

We have demonstrated that, in carbon nanotubes (CNTs), the photocurrent quantum yield (PCQY) can be increased by applying electric fields along the axis of the CNT. Furthermore, our data shows that, for the largest diameter CNTs in our study, the PCQY can exceed 100%.

In Chapter 2, I introduced a series of models that are useful for understanding carbon nanotube light-matter interactions in the presence of external electric fields. Fundamental properties of the system were revealed by considering simple systems like a harmonic oscillator. Finer details of CNT optical properties were uncovered by considering more advanced models that incorporate quantum mechanics.

The general features of the dual-gated, suspended carbon nanotube device are discussed in Chapter 3. I describe the growth procedure that can produce transparent contacts, form near ideal diodes, and maintain their properties over several days.

The computation models discussed in Chapter 4 laid a foundation to quantify the PCQY. First we used an electrostatics model to quantify the relationship between the voltages applied to the device and the axial electric field. This model was later validated through comparison to experimental observations of the instrinsic region length. Next, optically excited states in CNTs were modeled using solutions to the Bethe-Salpeter equation. The model showed the changes we expect in the CNT absorption spectrum in the presence of an axial electric field. We compared these predictions to the observed changes in the photocurrent spectrum in Chapter 5. Finally, in Chapter 4 a finite-difference-time-domain simulation was used to determine how the intensity of light incident on the nanotube is modulated by interference from light reflected off of the substrate below.

In Chapter 5, a method of extracting the PCQY from photocurrent spectra is laid out. Once a method is established, the field dependence of the PCQY is calculated from a series of photocurrent spectra taken with different electric fields. For light resonant with the S_{22} exciton energy, we saw that the PCQY increased with axial field. The most dramatic increases in PCQY occurred in the largest diameter CNTs. In one CNT, when the field changed from $F = 2$ –10 V/μm , the PCQY changed by a factor of 35 and reached a value of $\eta = 1.8$. We saw that while the PCQY of S_{22} excitons showed a strong dependence on the electric field, a less dramatic change in PCQY was observed from S_{33} over the same range of fields.

Theoretical modeling of the decay products from the S_{22} and S_{33} excitons was used to interpret our data. The modeling showed that the decay products of S_{33} form almost exclusively free carriers, whereas a large fraction of decay producs from S_{22} excitons form S_{11} and S_{12} excitons. Our interpretation is that the electric field can increase the PCQY in two ways. The first is by sweeping free carriers out of the device more quickly which increases the fraction of free carriers contributing to the photocurrent. The second is by assisting in the dissociation of the bound S_{11} and S_{12} decay product from excitation at the S_{22} exciton resonance. Furthermore, our data suggests that in the presence of a large electric field impact ionization can coexist with exciton dissociation in large diameter CNTs (D > 2.5 nm) when $\hbar\omega \approx 2E_g$.

7 Bibiliography

(1) Onnes, H. K. Proceedings of the Section of Sciences. *Koninklijke Akademie van Wetenschappen (Netherlands)* **1911**, *13*.

(2) Allen, J. F.; Misener, A. D. Flow of Liquid Helium II. *Nature* **1938**, *141* (3558), 75–75. https://doi.org/10.1038/141075a0.

(3) Kapitza, P. Viscosity of Liquid Helium below the λ-Point. *Nature* **1938**, *141* (3558), 74–74. https://doi.org/10.1038/141074a0.

(4) Bardeen, J.; Cooper, L. N.; Schrieffer, J. R. Theory of Superconductivity. *Phys. Rev.* **1957**, *108* (5), 1175–1204. https://doi.org/10.1103/PhysRev.108.1175.

(5) Valla, T.; Drozdov, I. K.; Gu, G. D. Disappearance of Superconductivity Due to Vanishing Coupling in the Overdoped Bi $$_{2}$$2 Sr $$_{2}$$2 CaCu $$_{2}$$2 O $$_{8+\delta }$$8+δ. *Nat Commun* **2020**, *11* (1), 1–7. https://doi.org/10.1038/s41467-020-14282-4.

(6) Klitzing, K. v.; Dorda, G.; Pepper, M. New Method for High-Accuracy Determination of the Fine-Structure Constant Based on Quantized Hall Resistance. *Phys. Rev. Lett.* **1980**, *45* (6), 494–497. https://doi.org/10.1103/PhysRevLett.45.494.

(7) Tsui, D. C.; Stormer, H. L.; Gossard, A. C. Two-Dimensional Magnetotransport in the Extreme Quantum Limit. *Phys. Rev. Lett.* **1982**, *48* (22), 1559–1562. https://doi.org/10.1103/PhysRevLett.48.1559.

(8) Laughlin, R. B. Anomalous Quantum Hall Effect: An Incompressible Quantum Fluid with Fractionally Charged Excitations. *Phys. Rev. Lett.* **1983**, *50* (18), 1395–1398. https://doi.org/10.1103/PhysRevLett.50.1395.

(9) Kane, C.; Balents, L.; Fisher, M. P. A. Coulomb Interactions and Mesoscopic Effects in Carbon Nanotubes. *Phys. Rev. Lett.* **1997**, *79* (25), 5086–5089. https://doi.org/10.1103/PhysRevLett.79.5086.

(10) Egger, R.; Gogolin, A. O. Effective Low-Energy Theory for Correlated Carbon Nanotubes. *Phys. Rev. Lett.* **1997**, *79* (25), 5082–5085. https://doi.org/10.1103/PhysRevLett.79.5082.

(11) Bockrath, M.; Cobden, D. H.; Lu, J.; Rinzler, A. G.; Smalley, R. E.; Balents, L.; McEuen, P. L. Luttinger-Liquid Behaviour in Carbon Nanotubes. *Nature* **1999**, *397* (6720), 598–601. https://doi.org/10.1038/17569.

(12) Deshpande, V. V.; Bockrath, M. The One-Dimensional Wigner Crystal in Carbon Nanotubes. *Nature Phys* **2008**, *4* (4), 314–318. https://doi.org/10.1038/nphys895.

(13) Shapir, I.; Hamo, A.; Pecker, S.; Moca, C. P.; Legeza, Ö.; Zarand, G.; Ilani, S. Imaging the Electronic Wigner Crystal in One Dimension. *Science* **2019**, *364* (6443), 870–875. https://doi.org/10.1126/science.aat0905.

(14) Shyu, F. L.; Lin, M. F. \ensuremath{\pi} Plasmons in Two-Dimensional Arrays of Aligned Carbon Nanotubes. *Phys. Rev. B* **1999**, *60* (20), 14434–14440. https://doi.org/10.1103/PhysRevB.60.14434.

(15) Lin, M. F.; Chuu, D. S. \ensuremath{\pi} Plasmons in Carbon Nanotube Bundles. *Phys. Rev. B* **1998**, *57* (16), 10183–10187. https://doi.org/10.1103/PhysRevB.57.10183.

(16) Krotov, Yu. A.; Lee, D.-H.; Louie, S. G. Low Energy Properties of (n,n) Carbon Nanotubes. *Phys. Rev. Lett.* **1997**, *78* (22), 4245–4248. https://doi.org/10.1103/PhysRevLett.78.4245.

(17) Odintsov, A. A.; Yoshioka, H. Universality of Electron Correlations in Conducting Carbon Nanotubes. *Phys. Rev. B* **1999**, *59* (16), R10457–R10460. https://doi.org/10.1103/PhysRevB.59.R10457.
(18) Nersesyan, A. A.; Tsvelik, A. M. Coulomb Blockade Regime of a Single-Wall Carbon Nanotube. *Phys. Rev. B* **2003**, *68* (23), 235419. https://doi.org/10.1103/PhysRevB.68.235419.
(19) Yoshioka, H.; Odintsov, A. A. Electronic Properties of Armchair Carbon Nanotubes: Bosonization Approach. *Phys. Rev. Lett.* **1999**, *82* (2), 374–377. https://doi.org/10.1103/PhysRevLett.82.374.
(20) Deshpande, V. V.; Chandra, B.; Caldwell, R.; Novikov, D. S.; Hone, J.; Bockrath, M. Mott Insulating State in Ultraclean Carbon Nanotubes. *Science* **2009**, *323* (5910), 106–110. https://doi.org/10.1126/science.1165799.
(21) Varsano, D.; Sorella, S.; Sangalli, D.; Barborini, M.; Corni, S.; Molinari, E.; Rontani, M. Carbon Nanotubes as Excitonic Insulators. *Nat Commun* **2017**, *8* (1), 1–9. https://doi.org/10.1038/s41467-017-01660-8.
(22) Senger, M. J.; McCulley, D. R.; Lotfizadeh, N.; Deshpande, V. V.; Minot, E. D. Universal Interaction-Driven Gap in Metallic Carbon Nanotubes. *Phys. Rev. B* **2018**, *97* (3), 035445. https://doi.org/10.1103/PhysRevB.97.035445.
(23) Wang, F.; Dukovic, G.; Brus, L. E.; Heinz, T. F. The Optical Resonances in Carbon Nanotubes Arise from Excitons. *Science* **2005**, *308* (5723), 838–841. https://doi.org/10.1126/science.1110265.
(24) Peng, B.; Zhang, H.; Shao, H.; Xu, K.; Ni, G.; Wu, L.; Li, J.; Lu, H.; Jin, Q.; Zhu, H. Room-Temperature Bound Exciton with Long Lifetime in Monolayer GaN. *ACS Photonics* **2018**, *5* (10), 4081–4088. https://doi.org/10.1021/acsphotonics.8b00757.
(25) Miller, R. C.; Kleinman, D. A. Excitons in GaAs Quantum Wells. *Journal of Luminescence* **1985**, *30* (1), 520–540. https://doi.org/10.1016/0022-2313(85)90075-4.
(26) Li, J.; Zhong, Y. L.; Zhang, D. Excitons in Monolayer Transition Metal Dichalcogenides. *J. Phys.: Condens. Matter* **2015**, *27* (31), 315301. https://doi.org/10.1088/0953-8984/27/31/315301.
(27) Ostroverkhova, O. Organic Optoelectronic Materials: Mechanisms and Applications. *Chem. Rev.* **2016**, *116* (22), 13279–13412. https://doi.org/10.1021/acs.chemrev.6b00127.
(28) Shockley, W.; Queisser, H. J. Detailed Balance Limit of Efficiency of *P-n* Junction Solar Cells. *Journal of Applied Physics* **1961**, *32* (3), 510–519. https://doi.org/10.1063/1.1736034.
(29) Werner, J. H.; Kolodinski, S.; Queisser, H. J. Novel Optimization Principles and Efficiency Limits for Semiconductor Solar Cells. *Phys. Rev. Lett.* **1994**, *72* (24), 3851–3854. https://doi.org/10.1103/PhysRevLett.72.3851.
(30) Beard, M. C. Multiple Exciton Generation in Semiconductor Quantum Dots. *J. Phys. Chem. Lett.* **2011**, *2* (11), 1282–1288. https://doi.org/10.1021/jz200166y.
(31) Pijpers, J. J. H.; Ulbricht, R.; Tielrooij, K. J.; Osherov, A.; Golan, Y.; Delerue, C.; Allan, G.; Bonn, M. Assessment of Carrier-Multiplication Efficiency in Bulk PbSe and PbS. *Nature Physics; London* **2009**, *5* (11), 811–814. http://dx.doi.org.ezproxy.proxy.library.oregonstate.edu/10.1038/nphys1393.
(32) Pandey, A.; Guyot-Sionnest, P. Slow Electron Cooling in Colloidal Quantum Dots. *Science* **2008**, *322* (5903), 929–932. https://doi.org/10.1126/science.1159832.

(33) Jiao, S.; Shen, Q.; Mora-Seró, I.; Wang, J.; Pan, Z.; Zhao, K.; Kuga, Y.; Zhong, X.; Bisquert, J. Band Engineering in Core/Shell ZnTe/CdSe for Photovoltage and Efficiency Enhancement in Exciplex Quantum Dot Sensitized Solar Cells. *ACS Nano* **2015**, *9* (1), 908–915. https://doi.org/10.1021/nn506638n.

(34) Tomić, S.; Miloszewski, J. M.; Tyrrell, E. J.; Binks, D. J. Design of Core/Shell Colloidal Quantum Dots for MEG Solar Cells. *IEEE J. Photovolt.* **2016**, *6* (1), 179–184. https://doi.org/10.1109/JPHOTOV.2015.2483368.

(35) Cirloganu, C. M.; Padilha, L. A.; Lin, Q.; Makarov, N. S.; Velizhanin, K. A.; Luo, H.; Robel, I.; Pietryga, J. M.; Klimov, V. I. Enhanced Carrier Multiplication in Engineered Quasi-Type-II Quantum Dots. *Nat. Commun.* **2014**, *5*, 4148. https://doi.org/10.1038/ncomms5148.

(36) Stewart, J. T.; Padilha, L. A.; Qazilbash, M. M.; Pietryga, J. M.; Midgett, A. G.; Luther, J. M.; Beard, M. C.; Nozik, A. J.; Klimov, V. I. Comparison of Carrier Multiplication Yields in PbS and PbSe Nanocrystals: The Role of Competing Energy-Loss Processes. *Nano Lett.* **2012**, *12* (2), 622–628. https://doi.org/10.1021/nl203367m.

(37) Davis, N. J. L. K.; Böhm, M. L.; Tabachnyk, M.; Wisnivesky-Rocca-Rivarola, F.; Jellicoe, T. C.; Ducati, C.; Ehrler, B.; Greenham, N. C. Multiple-Exciton Generation in Lead Selenide Nanorod Solar Cells with External Quantum Efficiencies Exceeding 120%. *Nat. Commun.* **2015**, *6*, 8259. https://doi.org/10.1038/ncomms9259.

(38) Semonin, O. E.; Luther, J. M.; Choi, S.; Chen, H.-Y.; Gao, J.; Nozik, A. J.; Beard, M. C. Peak External Photocurrent Quantum Efficiency Exceeding 100% via MEG in a Quantum Dot Solar Cell. *Science* **2011**, *334* (6062), 1530–1533. https://doi.org/10.1126/science.1209845.

(39) Sambur, J. B.; Novet, T.; Parkinson, B. A. Multiple Exciton Collection in a Sensitized Photovoltaic System. *Science* **2010**, *330* (6000), 63–66. https://doi.org/10.1126/science.1191462.

(40) Ridley, B. K. *Quantum Processes in Semiconductors*, 5th ed.; Oxford University Press, 2013. https://doi.org/10.1093/acprof:oso/9780199677214.001.0001.

(41) Tirino, L.; Weber, M.; Brennan, K. F.; Bellotti, E.; Goano, M. Temperature Dependence of the Impact Ionization Coefficients in GaAs, Cubic SiC, and Zinc-Blende GaN. *Journal of Applied Physics* **2003**, *94* (1), 423–430. https://doi.org/10.1063/1.1579129.

(42) Rees, G. J.; David, J. P. R. Nonlocal Impact Ionization and Avalanche Multiplication. *J. Phys. D: Appl. Phys.* **2010**, *43* (24), 243001. https://doi.org/10.1088/0022-3727/43/24/243001.

(43) Buller, G. S.; Collins, R. J. Single-Photon Generation and Detection. *Meas. Sci. Technol.* **2009**, *21* (1), 012002. https://doi.org/10.1088/0957-0233/21/1/012002.

(44) Canfield, L. R.; Vest, R. E.; Korde, R.; Schmidtke, H.; Desor, R. Absolute Silicon Photodiodes for 160 Nm to 254 Nm Photons. *Metrologia* **1998**, *35* (4), 329–334. https://doi.org/10.1088/0026-1394/35/4/19.

(45) Impact Ionization Can Explain Carrier Multiplication in PbSe Quantum Dots | Nano Letters https://pubs-acs-org.ezproxy.proxy.library.oregonstate.edu/doi/abs/10.1021/nl0612401 (accessed Apr 13, 2020).

(46) Chen, J.; Perebeinos, V.; Freitag, M.; Tsang, J.; Fu, Q.; Liu, J.; Avouris, P. Bright Infrared Emission from Electrically Induced Excitons in Carbon Nanotubes. *Science* **2005**, *310* (5751), 1171–1174. https://doi.org/10.1126/science.1119177.

(47) Perebeinos, V.; Avouris, P. Impact Excitation by Hot Carriers in Carbon Nanotubes. *Phys. Rev. B* **2006**, *74* (12), 121410. https://doi.org/10.1103/PhysRevB.74.121410.
(48) Gabor, N. M. Impact Excitation and Electron–Hole Multiplication in Graphene and Carbon Nanotubes. *Acc. Chem. Res.* **2013**, *46* (6), 1348–1357. https://doi.org/10.1021/ar300189j.
(49) Javey, A.; Guo, J.; Wang, Q.; Lundstrom, M.; Dai, H. Ballistic Carbon Nanotube Field-Effect Transistors. *Nature* **2003**, *424* (6949), 654–657. https://doi.org/10.1038/nature01797.
(50) Gabor, N. M.; Zhong, Z.; Bosnick, K.; Park, J.; McEuen, P. L. Extremely Efficient Multiple Electron-Hole Pair Generation in Carbon Nanotube Photodiodes. *Science* **2009**, *325* (5946), 1367–1371. https://doi.org/10.1126/science.1176112.
(51) Wang, S.; Khafizov, M.; Tu, X.; Zheng, M.; Krauss, T. D. Multiple Exciton Generation in Single-Walled Carbon Nanotubes. *Nano Lett.* **2010**, *10* (7), 2381–2386. https://doi.org/10.1021/nl100343j.
(52) Wang, B.; Yang, S.; Shen, L.; Cronin, S. B. Ultra-Low Power Light Emission via Avalanche and Sub-Avalanche Breakdown in Suspended Carbon Nanotubes. *ACS Photonics* **2018**, *5* (11), 4432–4436. https://doi.org/10.1021/acsphotonics.8b00896.
(53) Barkelid, M.; Steele, G. A.; Zwiller, V. Probing Optical Transitions in Individual Carbon Nanotubes Using Polarized Photocurrent Spectroscopy. *Nano Lett.* **2012**, *12* (11), 5649–5653. https://doi.org/10.1021/nl302789k.
(54) Malapanis, A.; Perebeinos, V.; Sinha, D. P.; Comfort, E.; Lee, J. U. Quantum Efficiency and Capture Cross Section of First and Second Excitonic Transitions of Single-Walled Carbon Nanotubes Measured through Photoconductivity. *Nano Lett.* **2013**, *13* (8), 3531–3538. https://doi.org/10.1021/nl400939b.
(55) Chang, S.-W.; Theiss, J.; Hazra, J.; Aykol, M.; Kapadia, R.; Cronin, S. B. Photocurrent Spectroscopy of Exciton and Free Particle Optical Transitions in Suspended Carbon Nanotube Pn-Junctions. *Appl. Phys. Lett.* **2015**, *107* (5), 053107. https://doi.org/10.1063/1.4928196.
(56) Aspitarte, L.; McCulley, D. R.; Minot, E. D. Photocurrent Quantum Yield in Suspended Carbon Nanotube p–n Junctions. *Nano Lett.* **2016**, *16* (9), 5589–5593. https://doi.org/10.1021/acs.nanolett.6b02148.
(57) Wang, F.; Wang, S.; Yao, F.; Xu, H.; Wei, N.; Liu, K.; Peng, L.-M. High Conversion Efficiency Carbon Nanotube-Based Barrier-Free Bipolar-Diode Photodetector. *ACS Nano* **2016**, *10* (10), 9595–9601. https://doi.org/10.1021/acsnano.6b05047.
(58) Kumamoto, Y.; Yoshida, M.; Ishii, A.; Yokoyama, A.; Shimada, T.; Kato, Y. K. Spontaneous Exciton Dissociation in Carbon Nanotubes. *Phys. Rev. Lett.* **2014**, *112* (11), 117401. https://doi.org/10.1103/PhysRevLett.112.117401.
(59) Perebeinos, V.; Avouris, P. Exciton Ionization, Franz−Keldysh, and Stark Effects in Carbon Nanotubes. *Nano Lett.* **2007**, *7* (3), 609–613. https://doi.org/10.1021/nl0625022.
(60) Baer, R.; Rabani, E. Can Impact Excitation Explain Efficient Carrier Multiplication in Carbon Nanotube Photodiodes? *Nano Lett.* **2010**, *10* (9), 3277–3282. https://doi.org/10.1021/nl100639h.
(61) Lotfizadeh, N.; McCulley, D. R.; Senger, M. J.; Fu, H.; Minot, E. D.; Skinner, B.; Deshpande, V. V. Band-Gap-Dependent Electronic Compressibility of Carbon Nanotubes in the Wigner Crystal Regime. *Phys. Rev. Lett.* **2019**, *123* (19), 197701. https://doi.org/10.1103/PhysRevLett.123.197701.

(62) Amer, Moh. R.; Bushmaker, A.; Cronin, S. B. The Influence of Substrate in Determining the Band Gap of Metallic Carbon Nanotubes. *Nano Lett.* **2012**, *12* (9), 4843–4847. https://doi.org/10.1021/nl302321k.
(63) Aspitarte, L.; McCulley, D. R.; Bertoni, A.; Island, J. O.; Ostermann, M.; Rontani, M.; Steele, G. A.; Minot, E. D. Giant Modulation of the Electronic Band Gap of Carbon Nanotubes by Dielectric Screening. *Sci. Rep.* **2017**, *7* (1), 8828. https://doi.org/10.1038/s41598-017-09372-1.
(64) Aspitarte, L.; McCulley, D. R.; Minot, E. D. A Nanoscale Pn Junction in Series with Tunable Schottky Barriers. *J. Appl. Phys.* **2017**, *122* (13), 134304. https://doi.org/10.1063/1.4994194.
(65) Taylor, J. R. *Classical Mechanics*; University Science Books, 2005.
(66) Gordon, R. G. Three Sum Rules for Total Optical Absorption Cross Sections. *J. Chem. Phys.* **1963**, *38* (7), 1724–1729. https://doi.org/10.1063/1.1776946.
(67) Liu, K.; Hong, X.; Choi, S.; Jin, C.; Capaz, R. B.; Kim, J.; Wang, W.; Bai, X.; Louie, S. G.; Wang, E.; Wang, F. Systematic Determination of Absolute Absorption Cross-Section of Individual Carbon Nanotubes. *PNAS* **2014**, *111* (21), 7564–7569. https://doi.org/10.1073/pnas.1318851111.
(68) Shankar, R. *Principles of Quantum Mechanics*; Springer, 1994.
(69) McIntyre, D. H.; Manogue, C. A.; Tate, J. *Quantum Mechanics: A Paradigms Approach*; Pearson, 2012.
(70) Sakurai, J. J.; Napolitano, J. *Modern Quantum Mechanics*; Addison-Wesley, 2011.
(71) Introduction to Quantum Mechanics - David J. Griffiths - Google Books https://books.google.com/books/about/Introduction_to_Quantum_Mechanics.html?id=0h-nDAAAQBAJ (accessed Mar 25, 2020).
(72) Fox, A. M.; Fox, D. of P. and A. M. *Optical Properties of Solids*; Oxford University Press, 2001.
(73) Introduction to Quantum Optics: From the Semi-classical Approach to ... - Gilbert Grynberg, Alain Aspect, Claude Fabre - Google Books https://books.google.com/books/about/Introduction_to_Quantum_Optics.html?id=l-l0L8YInA0C (accessed Mar 25, 2020).
(74) Wilder, J. W. G.; Venema, L. C.; Rinzler, A. G.; Smalley, R. E.; Dekker, C. Electronic Structure of Atomically Resolved Carbon Nanotubes. *Nature* **1998**, *391* (6662), 59–62. https://doi.org/10.1038/34139.
(75) Lu, C.; Liu, J. Controlling the Diameter of Carbon Nanotubes in Chemical Vapor Deposition Method by Carbon Feeding. *J. Phys. Chem. B* **2006**, *110* (41), 20254–20257. https://doi.org/10.1021/jp0632283.
(76) Almaqwashi, A. A.; Kevek, J. W.; Burton, R. M.; DeBorde, T.; Minot, E. D. Variable-Force Microscopy for Advanced Characterization of Horizontally Aligned Carbon Nanotubes. *Nanotechnology* **2011**, *22* (27), 275717. https://doi.org/10.1088/0957-4484/22/27/275717.
(77) Ding, L.; Tselev, A.; Wang, J.; Yuan, D.; Chu, H.; McNicholas, T. P.; Li, Y.; Liu, J. Selective Growth of Well-Aligned Semiconducting Single-Walled Carbon Nanotubes. *Nano Lett.* **2009**, *9* (2), 800–805. https://doi.org/10.1021/nl803496s.
(78) Dirnaichner, A.; del Valle, M.; Götz, K. J. G.; Schupp, F. J.; Paradiso, N.; Grifoni, M.; Strunk, Ch.; Hüttel, A. K. Secondary Electron Interference from Trigonal Warping in

Clean Carbon Nanotubes. *Phys. Rev. Lett.* **2016**, *117* (16), 166804. https://doi.org/10.1103/PhysRevLett.117.166804.

(79) Lotfizadeh, N.; Senger, M. J.; McCulley, D. R.; Minot, E. D.; Deshpande, V. V. Sagnac Electron Interference as a Probe of Electronic Structure. *arXiv:1808.01341 [cond-mat]* **2018**.

(80) Reining, L. The GW Approximation: Content, Successes and Limitations. *WIREs Computational Molecular Science* **2018**, *8* (3), e1344. https://doi.org/10.1002/wcms.1344.

(81) Leng, X.; Jin, F.; Wei, M.; Ma, Y. GW Method and Bethe–Salpeter Equation for Calculating Electronic Excitations. *WIREs Computational Molecular Science* **2016**, *6* (5), 532–550. https://doi.org/10.1002/wcms.1265.

(82) Gao, W.; Xia, W.; Gao, X.; Zhang, P. Speeding up GW Calculations to Meet the Challenge of Large Scale Quasiparticle Predictions. *Sci Rep* **2016**, *6* (1), 1–8. https://doi.org/10.1038/srep36849.

(83) McCulley, D. R.; Senger, M. J.; Bertoni, A.; Perebeinos, V.; Minot, E. D. Extremely Efficient Photocurrent Generation in Carbon Nanotube Photodiodes Enabled by a Strong Axial Electric Field. *Nano Lett.* **2020**, *20* (1), 433–440. https://doi.org/10.1021/acs.nanolett.9b04151.

(84) Perebeinos, V.; Avouris, P. Phonon and Electronic Nonradiative Decay Mechanisms of Excitons in Carbon Nanotubes. *Phys. Rev. Lett.* **2008**, *101* (5), 057401. https://doi.org/10.1103/PhysRevLett.101.057401.

(85) Yasukochi, S.; Murai, T.; Moritsubo, S.; Shimada, T.; Chiashi, S.; Maruyama, S.; Kato, Y. K. Gate-Induced Blueshift and Quenching of Photoluminescence in Suspended Single-Walled Carbon Nanotubes. *Phys. Rev. B* **2011**, *84* (12), 121409. https://doi.org/10.1103/PhysRevB.84.121409.

(86) Liu, K.; Deslippe, J.; Xiao, F.; Capaz, R. B.; Hong, X.; Aloni, S.; Zettl, A.; Wang, W.; Bai, X.; Louie, S. G.; Wang, E.; Wang, F. An Atlas of Carbon Nanotube Optical Transitions. *Nat. Nanotechnol.* **2012**, *7* (5), 325–329. https://doi.org/10.1038/nnano.2012.52.

(87) DeBorde, T.; Kevek, J. W.; Sharf, T.; Wardini, J. L.; Minot, E. D. A Spectrally-Tunable Photocurrent Microscope for Characterizing Nanoelectronic Devices. In *2011 11th IEEE International Conference on Nanotechnology*; 2011; pp 382–386. https://doi.org/10.1109/NANO.2011.6144644.

(88) DeBorde, T.; Aspitarte, L.; Sharf, T.; Kevek, J. W.; Minot, E. D. Determining the Chiral Index of Semiconducting Carbon Nanotubes Using Photoconductivity Resonances. *J. Phys. Chem. C* **2014**, *118* (19), 9946–9950. https://doi.org/10.1021/jp502149c.

(89) Minot, E. D.; Yaish, Y.; Sazonova, V.; Park, J.-Y.; Brink, M.; McEuen, P. L. Tuning Carbon Nanotube Band Gaps with Strain. *Phys. Rev. Lett.* **2003**, *90* (15), 156401. https://doi.org/10.1103/PhysRevLett.90.156401.

(90) Huang, M.; Wu, Y.; Chandra, B.; Yan, H.; Shan, Y.; Heinz, T. F.; Hone, J. Direct Measurement of Strain-Induced Changes in the Band Structure of Carbon Nanotubes. *Phys. Rev. Lett.* **2008**, *100* (13), 136803. https://doi.org/10.1103/PhysRevLett.100.136803.

(91) Ando, T. Excitons in Carbon Nanotubes Revisited: Dependence on Diameter, Aharonov–Bohm Flux, and Strain. *Journal of the Physical Society of Japan* **2004**, *73* (12), 3351–3363. https://doi.org/10.1143/JPSJ.73.3351.

(92) He, X.; Htoon, H.; Doorn, S. K.; Pernice, W. H. P.; Pyatkov, F.; Krupke, R.; Jeantet, A.; Chassagneux, Y.; Voisin, C. Carbon Nanotubes as Emerging Quantum-Light Sources. *Nat. Mater.* **2018**, *17* (8), 663. https://doi.org/10.1038/s41563-018-0109-2.

(93) Hertel, T.; Perebeinos, V.; Crochet, J.; Arnold, K.; Kappes, M.; Avouris, P. Intersubband Decay of 1-D Exciton Resonances in Carbon Nanotubes. *Nano Lett.* **2008**, *8* (1), 87–91. https://doi.org/10.1021/nl0720915.

(94) Steiner, M.; Freitag, M.; Perebeinos, V.; Tsang, J. C.; Small, J. P.; Kinoshita, M.; Yuan, D.; Liu, J.; Avouris, P. Phonon Populations and Electrical Power Dissipation in Carbon Nanotube Transistors. *Nat. Nanotechnol.* **2009**, *4* (5), 320–324. https://doi.org/10.1038/nnano.2009.22.

(95) Hofmann, M. S.; Glückert, J. T.; Noé, J.; Bourjau, C.; Dehmel, R.; Högele, A. Bright, Long-Lived and Coherent Excitons in Carbon Nanotube Quantum Dots. *Nat. Nanotechnol.* **2013**, *8* (7), 502–505. https://doi.org/10.1038/nnano.2013.119.

(96) Sarpkaya, I.; Zhang, Z.; Walden-Newman, W.; Wang, X.; Hone, J.; Wong, C. W.; Strauf, S. Prolonged Spontaneous Emission and Dephasing of Localized Excitons in Air-Bridged Carbon Nanotubes. *Nat. Commun.* **2013**, *4* (1), 2152. https://doi.org/10.1038/ncomms3152.

(97) Ishii, A.; Yoshida, M.; Kato, Y. K. Exciton Diffusion, End Quenching, and Exciton-Exciton Annihilation in Individual Air-Suspended Carbon Nanotubes. *Phys. Rev. B* **2015**, *91* (12), 125427. https://doi.org/10.1103/PhysRevB.91.125427.

(98) Hertel, T.; Himmelein, S.; Ackermann, T.; Stich, D.; Crochet, J. Diffusion Limited Photoluminescence Quantum Yields in 1-D Semiconductors: Single-Wall Carbon Nanotubes. *ACS Nano* **2010**, *4* (12), 7161–7168. https://doi.org/10.1021/nn101612b.

(99) Mohite, A. D.; Gopinath, P.; Shah, H. M.; Alphenaar, B. W. Exciton Dissociation and Stark Effect in the Carbon Nanotube Photocurrent Spectrum. *Nano Lett.* **2008**, *8* (1), 142–146. https://doi.org/10.1021/nl0722525.

(100) Dukovic, G.; Wang, F.; Song, D.; Sfeir, M. Y.; Heinz, T. F.; Brus, L. E. Structural Dependence of Excitonic Optical Transitions and Band-Gap Energies in Carbon Nanotubes. *Nano Lett.* **2005**, *5* (11), 2314–2318. https://doi.org/10.1021/nl0518122.

8 Appendix: Extended data for devices A-J

(see next page)

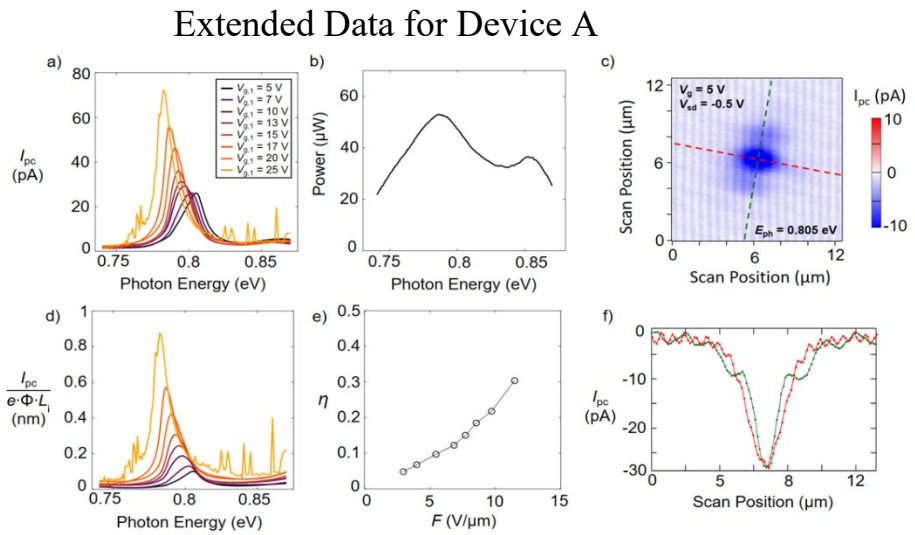

Figure 8.1 Device A Summary. a) Raw photocurrent spectrum of a (27,8) carbon nanotube. **b)** Laser power at the height of nanotube. **c)** Photocurrent image of the nanotube. The power is $P = 2.02$ μW with $\beta_{\mathrm{foc}} = 1.07$. **d)** The photocurrent spectrum corrected for photon flux and intrinsic region length. **e)** The photocurrent quantum yield as a function of the axial field at the center of the CNT. **f)** Cross sections along the photocurrent spot used to calculate an area A = 6.7 μm^2.

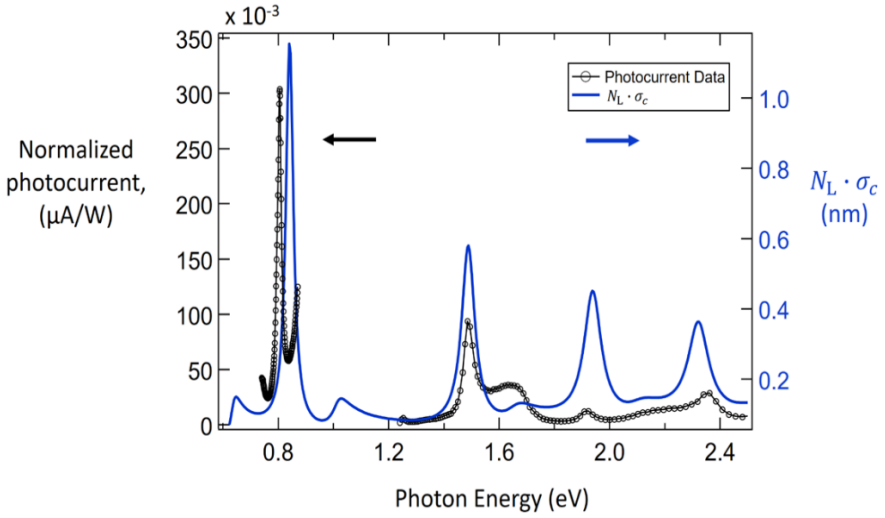

Figure 8.2 Photocurrent spectrum normalized by the laser power at the height of the nanotube 34 nm below the electrode (black). The product of absorption cross section per carbon atom and the number of atoms per length of a (27,8) CNT (blue).

$w_{y,0}$ (μm)	$a_{x,1}$	$a_{x,-1}$	$w_{x,0}$ (μm)	$w_{x,1}$(μm)	$w_{x,-1}$(μm)
1.49	0.29	0.32	0.88	0.89	0.93

Table 8.1 The fitting parameters for scanning photocurrent image cross sections for Device A. The extra lobes in the photocurrent image are fit using three Gaussians. The total area under them is $A_{\mathrm{foc}} = \pi w_{y,0}(w_{x,0} + a_{x,1}w_{x,1} + a_{x,-1}w_{x,-1})$.

Extended Data for Device B

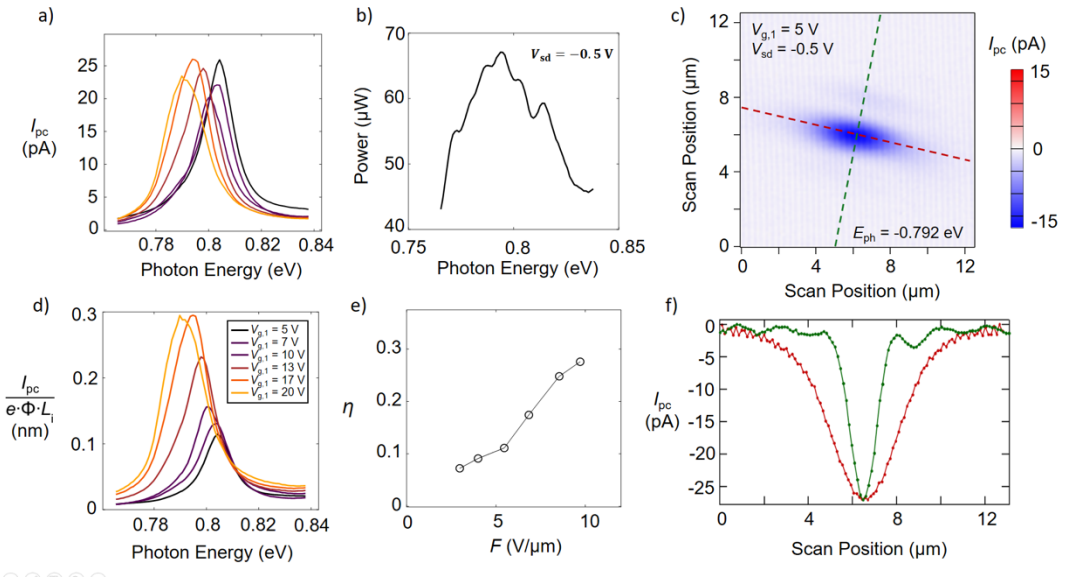

Figure 8.3 Device B Summary. **a)** The photocurrent spectrum of a (24,14) CNT. **b)** Laser power at the height of nanotube at 34 nm below the electrode surface. **c)** Photocurrent image of the nanotube. The power is $P = 8.36$ μW with $\beta_{\mathrm{foc}} = 1.14$. **d)** The photocurrent spectrum corrected for photon flux and intrinsic region length. **e)** The photocurrent quantum yield as a function of the axial field at the center of the CNT. **f)** Cross sections along the photocurrent spot used to calculate an area A =5.4 μm^2.

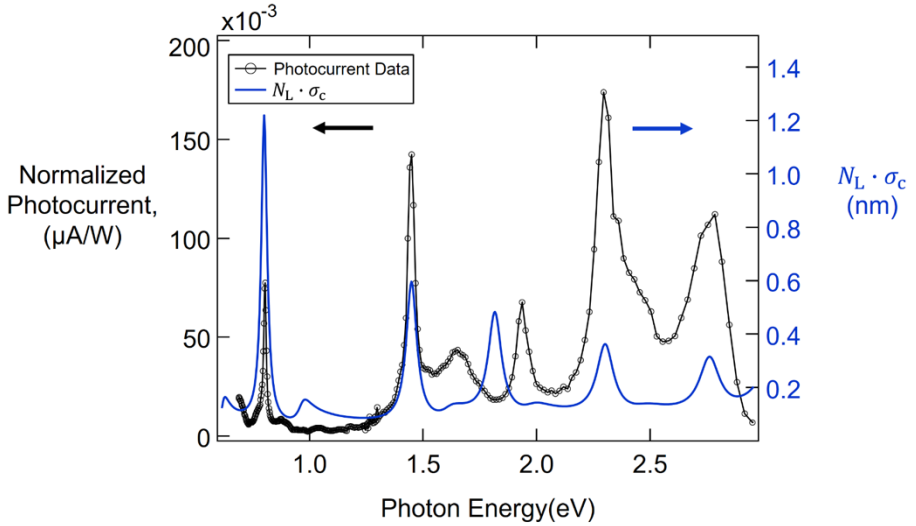

Figure 8.4 Photocurrent spectrum normalized by the laser power at the height of the nanotube 34 nm below the electrode (black). The product of absorption cross section per carbon atom and the number of atoms per length of a (24,14) CNT (blue).

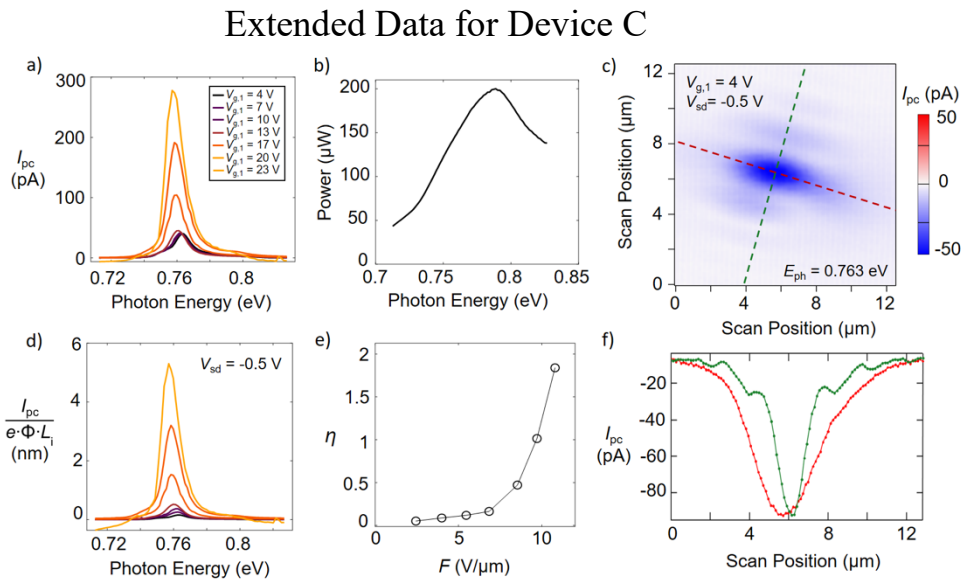

Figure 8.5 Device C Summary. Raw photocurrent spectrum of a (24,17) carbon nanotube. b) Laser power at the height of nanotube at 34 nm below the electrode surface. c) Photocurrent image of the nanotube. The power is $P = 23.1$ μW with $\beta_{\mathrm{foc}} = 1.31$. d) The photocurrent spectrum corrected for photon flux and intrinsic region length. e) The photocurrent quantum yield as a function of the axial field at the center of the CNT. f) Cross sections along the photocurrent spot used to calculate an area A = 9.1 μm^2.

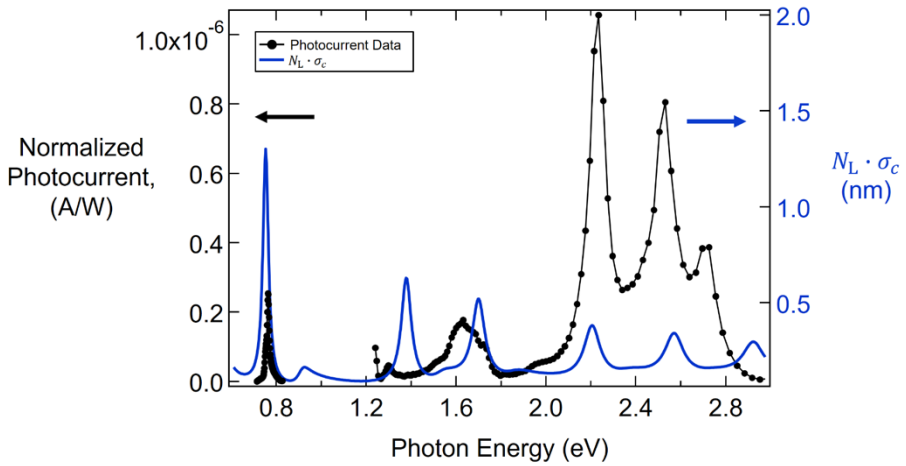

Figure 8.6 Photocurrent spectrum normalized by the laser power at the height of the nanotube 34 nm below the electrode (black). The product of absorption cross section per carbon atom and the number of atoms per length of a (24,17) CNT (blue).

$w_{y,0}$ (μm)	$a_{x,1}$	$a_{x,-1}$	$w_{x,0}$ (μm)	$w_{x,1}$ (μm)	$w_{x,-1}$ (μm)
2.38	0.20	0.17	0.99	0.84	0.94

Table 8.2 The fitting parameters for scanning photocurrent image cross sections for Device C. The extra lobes in the photocurrent image can be well fit using three Gaussians. The total area under them is $A_{\mathrm{foc}} = \pi w_{y,0}(w_{x,0} + a_{x,1}w_{x,1} + a_{x,-1}w_{x,-1})$.

Extended Data for Device D

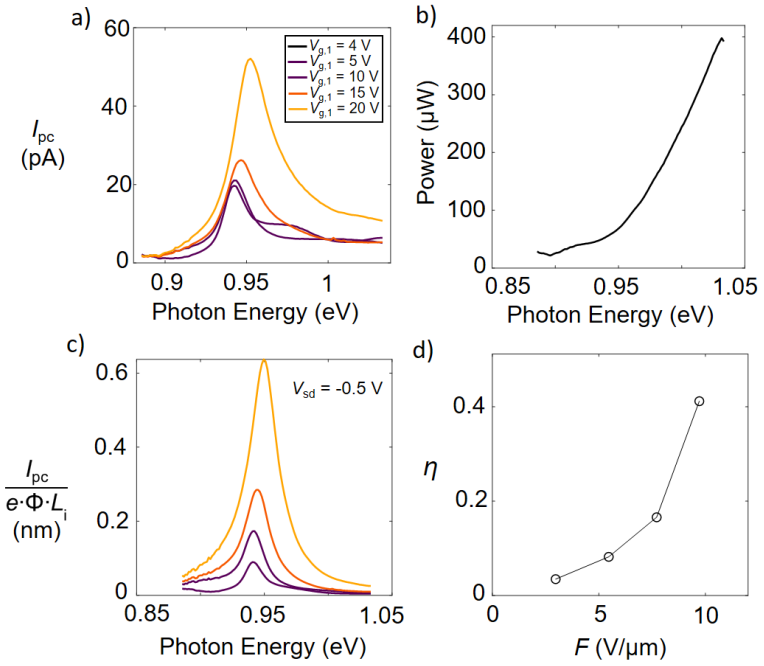

Figure 8.7 Device D Summary. Raw photocurrent spectrum of a (20,9) carbon nanotube. b) Laser power at the height of nanotube at 34 nm below the electrode surface. c) The photocurrent spectrum corrected for photon flux and intrinsic region length. d) The photocurrent quantum yield as a function of the axial field at the center of the CNT.

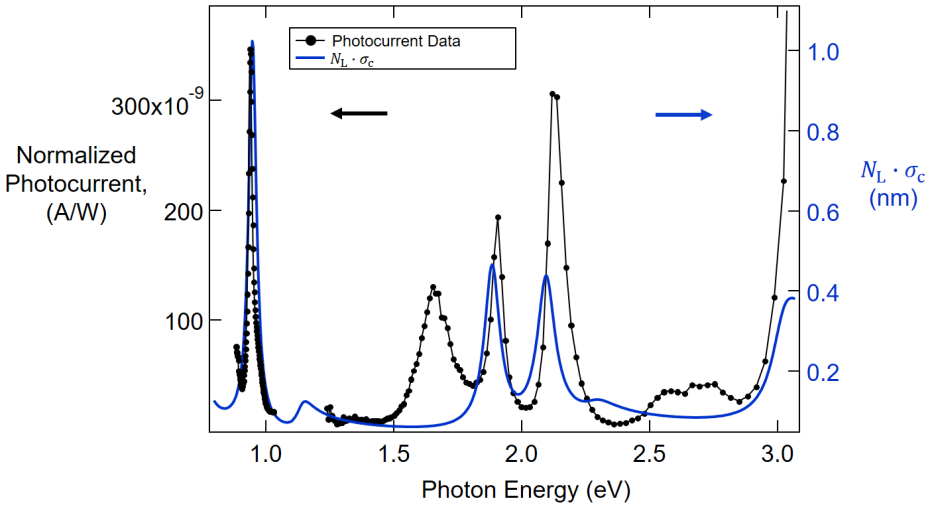

Figure 8.8 Photocurrent spectrum normalized by the laser power at the height of the nanotube 34 nm below the electrode (black). The product of absorption cross section per carbon atom and the number of atoms per length of a (20,9) CNT (blue).

Extended Data for Device E

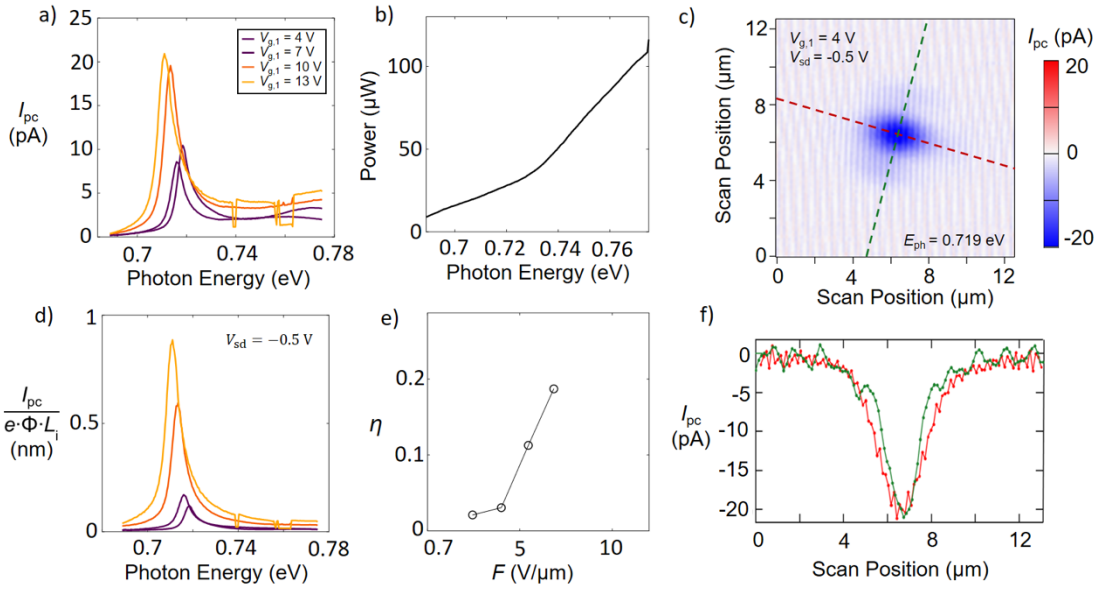

Figure 8.9 Device E Summary. Raw photocurrent spectrum of a (30,11) carbon nanotube. b) Laser power at the height of nanotube at 34 nm below the electrode surface. c) Photocurrent image of the nanotube. The power is $P = 1.63$ μW with $\beta_{foc} = 1.52$. d) The photocurrent spectrum corrected for photon flux and intrinsic region length. e) The photocurrent quantum yield as a function of the axial field at the center of the CNT. f) Cross sections along the photocurrent spot used to calculate an area A = 5.4 μm^2.

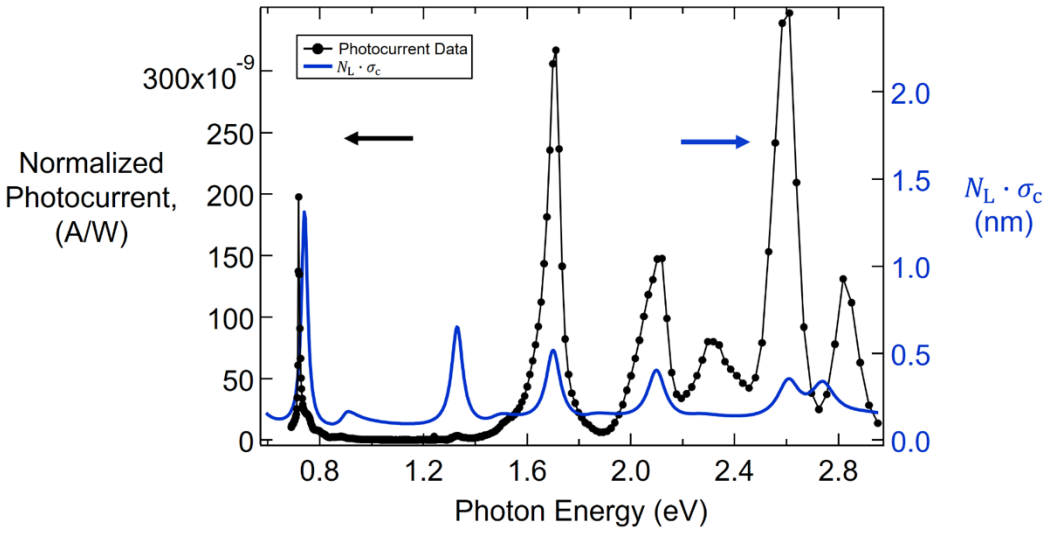

Figure 8.10 Photocurrent spectrum normalized by the laser power at the height of the nanotube at 34 nm below the electrode (black). The product of absorption cross section per carbon atom and the number of atoms per length of a (30,11) CNT (blue).

Extended Data for Device F

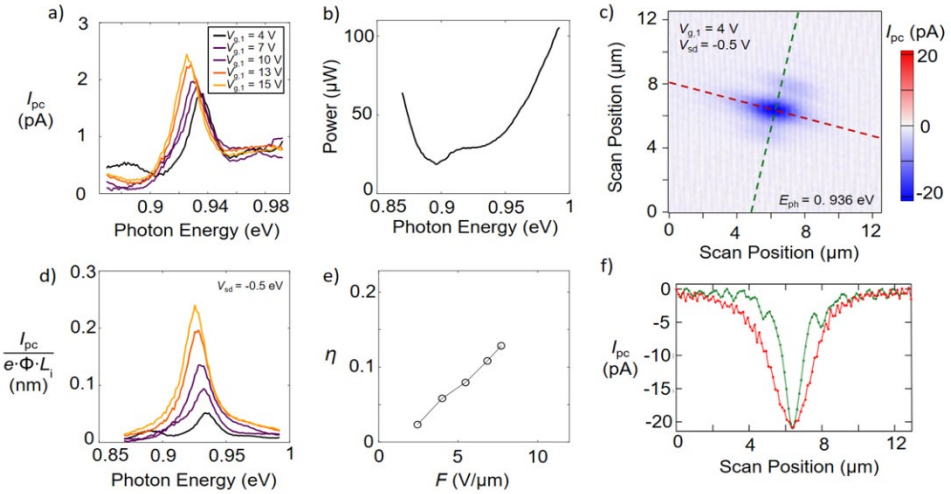

Figure 8.11 S25 Device F Summary. Raw photocurrent spectrum of a (20,10) carbon nanotube. b) Laser power at the height of nanotube at 34 nm below the electrode surface. c) Photocurrent image of the nanotube. The power is $P = 5.6$ μW with $\beta_{\mathrm{foc}} = 0.49$. d) The photocurrent spectrum corrected for photon flux and intrinsic region length. e) The photocurrent quantum yield as a function of the axial field at the center of the CNT. f) Cross sections along the photocurrent spot used to calculate an area A = 5.5 μm^2.

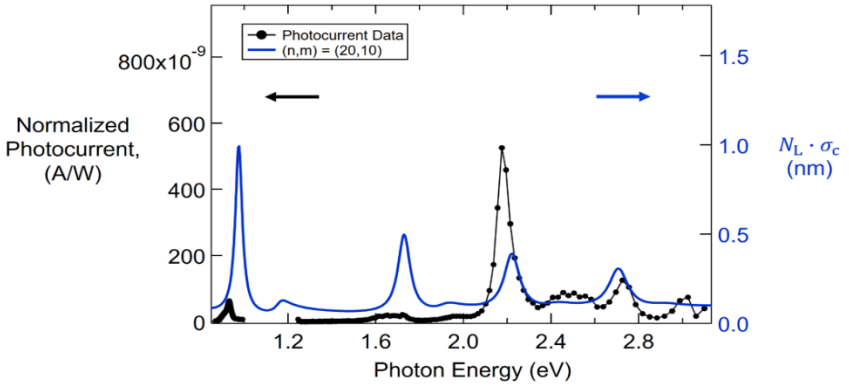

Figure 8.12 Photocurrent spectrum normalized by the laser power at the height of the nanotube 34 nm below the electrode (black). The product of absorption cross section per carbon atom and the number of atoms per length of a (20,10) CNT (blue).

$w_{y,0}$ (μm)	$a_{x,1}$	$a_{x,-1}$	$w_{x,0}$ (μm)	$w_{x,1}$ (μm)	$w_{x,-1}$ (μm)
1.66	0.25	0.16	0.79	0.69	0.68

Table 8.3 The fitting parameters for scanning photocurrent image cross sections for Device F. The extra lobes in the photocurrent image can be well fit using three Gaussians. The total area under them is $A_{\mathrm{foc}} = \pi w_{y,0}(a_{x,0}w_{x,0} + a_{x,1}w_{x,1} + a_{x,-1}w_{x,-1})$.

Extended Data for Device G

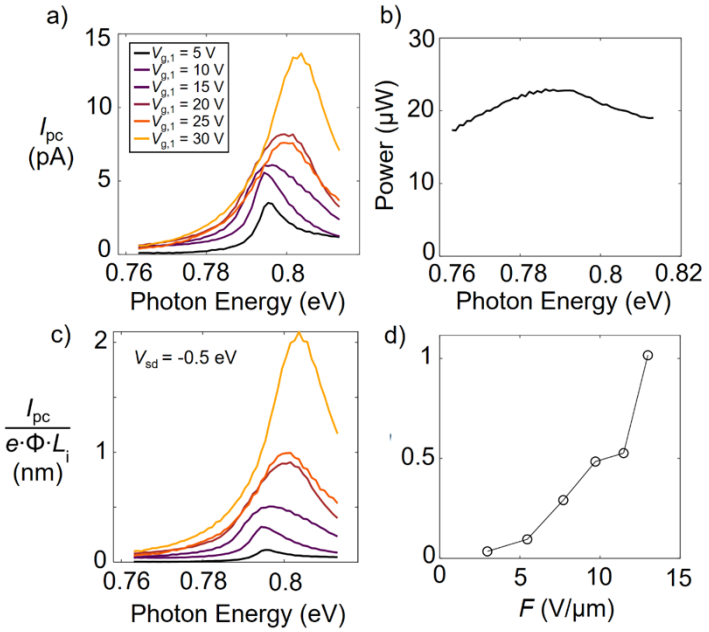

Figure 8.13 Device G Summary a) Raw photocurrent spectrum of a (22,14) carbon nanotube. b) Laser power at the height of nanotube at 34 nm below the electrode surface. c) The photocurrent spectrum corrected for photon flux and intrinsic region length. d) The photocurrent quantum yield as a function of the axial field at the center of the CNT.

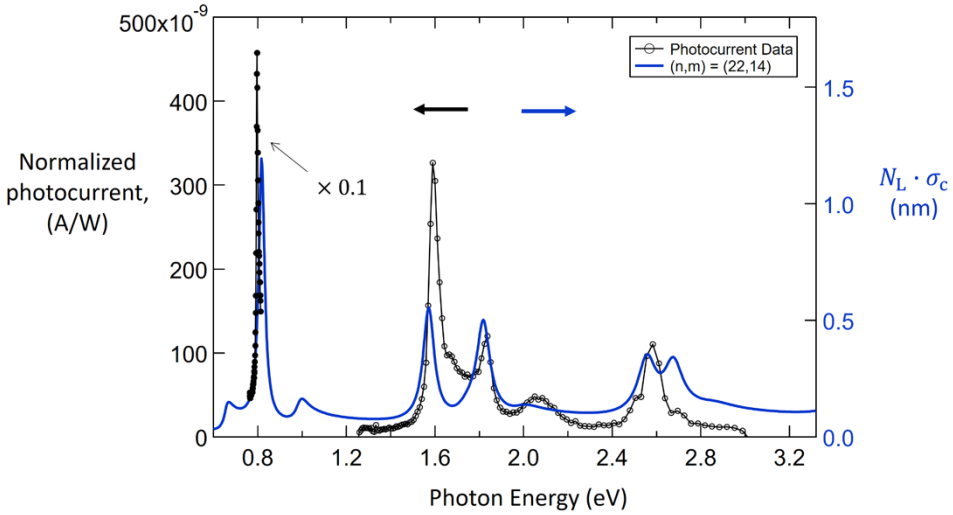

Figure 8.14 Photocurrent spectrum normalized by the laser power at the height of the nanotube 34 nm below the electrode (black). The product of absorption cross section per carbon atom and the number of atoms per length of a (22,14) CNT (blue).

Extended Data for Device H

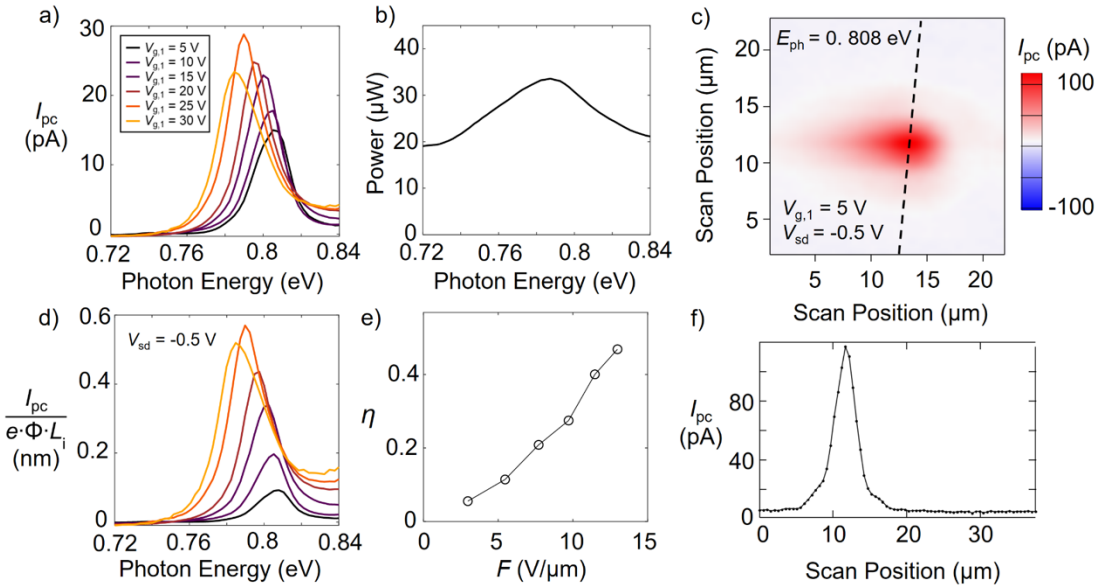

Figure 8.15 Device H Summary. The photocurrent spectrum of a (20,16) carbon nanotube. b) Laser power at the height of nanotube at 34 nm below the electrode surface. c) Photocurrent image of the nanotube. The power is $P = 44.3$ μW with $\beta_{foc} = 1.05$. d) The photocurrent spectrum corrected for photon flux and intrinsic region length. e) The photocurrent quantum yield as a function of the axial field at the center of the CNT. f) Cross sections along the photocurrent spot used to calculate an area A = 15.2 μm^2.

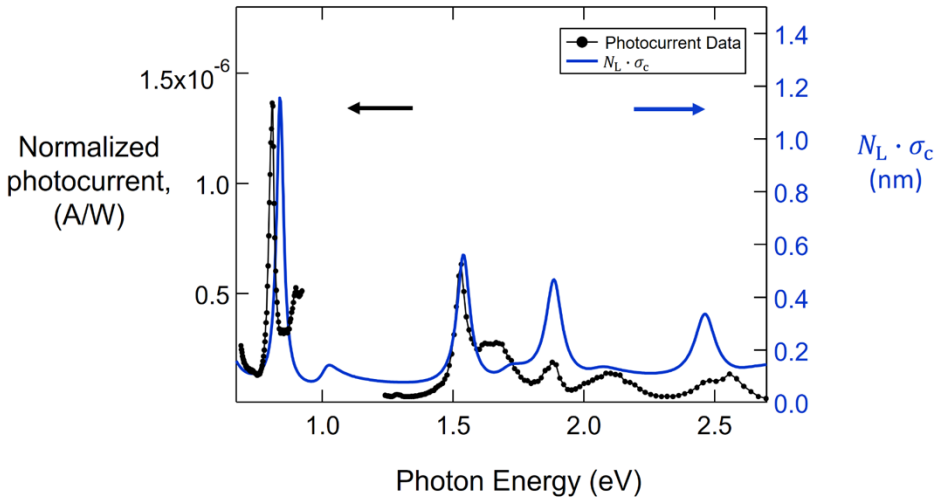

Figure 8.16 Photocurrent spectrum normalized by the laser power at the height of the nanotube 34 nm below the electrode (black). The product of absorption cross section per carbon atom and the number of atoms per length in the nanotube (blue).

Extended Data for Device J

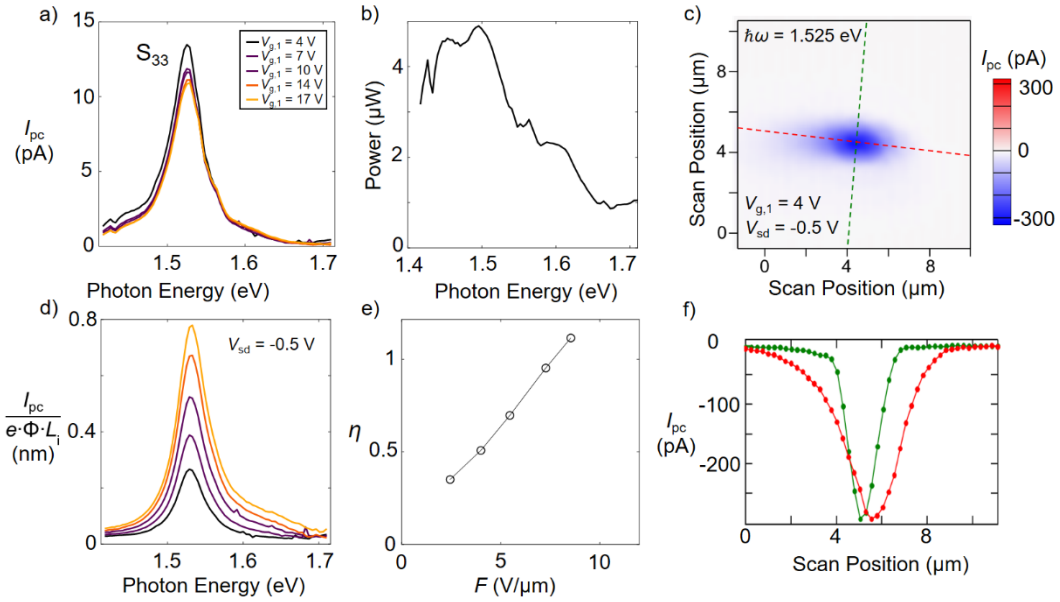

Figure 8.17 Device J Summary Raw photocurrent spectrum of a (19,18) carbon nanotube. b) Laser power at the height of nanotube at 34 nm below the electrode surface with $\beta_{foc}/\beta_{def} = 1.62$. c) Photocurrent image of the nanotube. The power is $P = 46.8$ μW with $\beta_{foc} = 1.41$. d) The photocurrent spectrum corrected for photon flux and intrinsic region length. e) The photocurrent quantum yield as a function of the axial field at the center of the CNT. f) Cross sections along the photocurrent spot were used to calculate an area $A = 4.92$ μm^2.

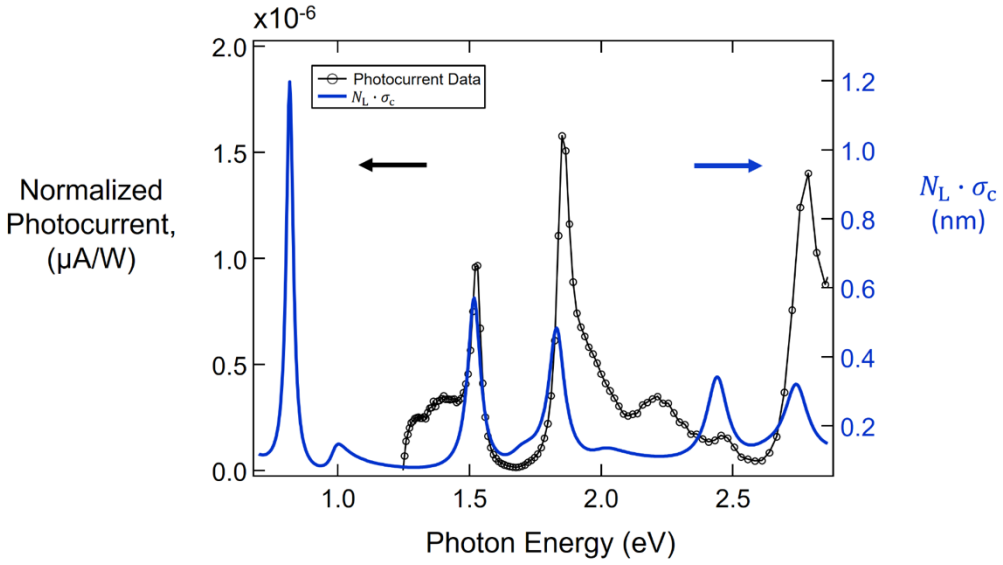

Figure 8.18 Photocurrent spectrum normalized by the laser power at the height of the nanotube 34 nm below the electrode (black) and the optical width of a (19,18) nanotube (blue)